AD-A031 852 HARVARD UNIV CAMBRIDGE MASS DIV OF ENGINEERING AND --ETC F/G 20/5
DIELECTRIC BREAKDOWN INDUCED BY PICOSECOND LASER PULSES.(U)
OCT 76 W L SMITH, J H BECHTEL, N BLOEMBERGEN N00014-75-C-0648

UNCLASSIFIED TR-665 NL

1 OF 2
AD
A031 852

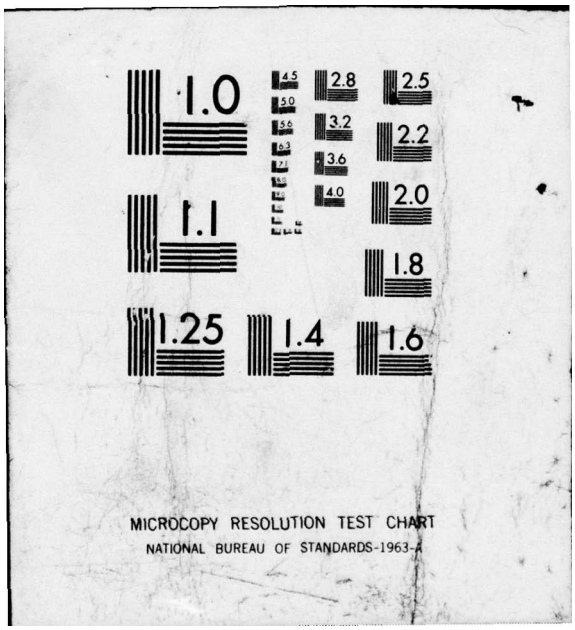
1.0
1.1
1.25
1.4
1.6
1.8
2.0
2.2
2.5
2.8
3.2
3.6
4.0
4.5
5.0
5.6
6.3
7.1
MICROCOPY RESOLUTION TEST CHART
NATIONAL BUREAU OF STANDARDS-1963-A

Office of Naval Research
Contract N00014-75-C-0648 NR-372-012
Advanced Research Projects Agency Grant F 44620-76-C-0068
National Aeronautics and Space Administration Grant NGL-22-007-117

DIELECTRIC BREAKDOWN INDUCED BY PICOSECOND LASER PULSES

By
W. Lee Smith, J. H. Bechtel, and N. Bloembergen

October, 1976

Technical Report No. 065

Division of Engineering and Applied Physics
Harvard University • Cambridge, Massachusetts

Unclassified

SECURITY CLASSIFICATION OF THIS PAGE (When Data Entered)

REPORT DOCUMENTATION PAGE	READ INSTRUCTIONS BEFORE COMPLETING FORM
1. REPORT NUMBER: Technical Report No. 665 (9) Jan 74 - Jun 76	2. GOVT ACCESSION NO. / 3. RECIPIENT'S CATALOG NUMBER: (14) TR-665
4. TITLE (and Subtitle): (6) DIELECTRIC BREAKDOWN INDUCED BY PICOSECOND LASER PULSES.	5. TYPE OF REPORT & PERIOD COVERED: Interim Report
	6. PERFORMING ORG. REPORT NUMBER
7. AUTHOR(s): (10) W. Lee Smith, J. H. Bechtel, N. Bloembergen	8. CONTRACT OR GRANT NUMBER(s): (15) N00014-75-C-0648, F 44620-75-C-0088, NASA NGL-22-007-117
9. PERFORMING ORGANIZATION NAME AND ADDRESS: Division of Engineering and Applied Physics, Harvard University, Cambridge, Massachusetts	10. PROGRAM ELEMENT, PROJECT, TASK AREA & WORK UNIT NUMBERS
11. CONTROLLING OFFICE NAME AND ADDRESS	12. REPORT DATE: Oct 1976 (11)
	13. NUMBER OF PAGES: 177 (12) 180p.
14. MONITORING AGENCY NAME & ADDRESS (if different from Controlling Office)	15. SECURITY CLASS. (of this report): Unclassified
	15a. DECLASSIFICATION/DOWNGRADING SCHEDULE

16. DISTRIBUTION STATEMENT (of this Report)

This document has been approved for public release and sale; its distribution is unlimited. Reproduction in whole or in part is permitted by the U.S. Government.

17. DISTRIBUTION STATEMENT (of the abstract entered in Block 20, if different from Report)

18. SUPPLEMENTARY NOTES

19. KEY WORDS (Continue on reverse side if necessary and identify by block number)

Dielectric breakdown
Laser-induced damage
Picosecond laser pulses
Avalanche ionization
Multiphoton absorption
Self-focusing

MICROMETERS

20. ABSTRACT (Continue on reverse side if necessary and identify by block number)

This report contains the consolidated results of investigations, carried out in the period January 1974 - June 1976 on the damage threshold of transparent optical materials. Single picosecond pulses at 1.06 μm, 0.53 μm and 0.35 μm were obtained from a mode-locked Nd-YAG oscillator-amplifier-frequency multiplier system. The pulses are Gaussian in space and time and permit the determination of breakdown thresholds with a reproducibility of →

DD FORM 1 JAN 73 1473 EDITION OF 1 NOV 65 IS OBSOLETE
S/N 0102-014-6601

Unclassified
SECURITY CLASSIFICATION OF THIS PAGE (When Data Entered)

163750

fifteen percent. It is shown that the breakdown thresholds reported here are characteristic of the bulk material, which include nine alkali halides, five different laser host materials, KDP, quartz, sapphire and calcium fluoride. The extension of the damage data to the ultraviolet is significant, because some indication is obtained that two- and three-photon absorption processes begin to play a role in determining the threshold. Throughout the visible region of the spectrum the threshold is still an increasing function of frequency, indicating that avalanche ionization is the dominant factor in determining the breakdown threshold. This is confirmed by a detailed study of the damage morphology with a high resolution microscope just above the threshold. A detailed discussion of the influence of self-focusing is given, and evidence for beam distortion below the power threshold for complete self-focusing is presented, confirming the theory of Marburger.

This report constitutes essentially the material of the Ph. D. thesis of Walter Lee Smith, submitted in partial fulfillment of the requirements for the degree of Doctor of Philosophy in the subject of Applied Physics, Harvard University, September 1976.

Chapter I describes briefly previous work on laser induced breakdown and the relationship of the present work to that described in technical report 643, Laser Induced Damage in Solids, May, 1973, by D. W. Fradin. Chapter II gives a description of the picosecond laser system. Chapters III-V give the experimental results of the breakdown at three different wave lengths, in the near infrared, the green and the near ultraviolet. This material is presented mostly in the form of reprints, or of preprints of papers submitted for publication.

The four appendices include reprints of papers on two-photon absorption in semiconductors and multiphoton photo-electric emission of metals, which have also been made possible by the existence of the reproducible picosecond pulse generator.

All this material is assembled in the present report because of its relevance and potential usefulness for high power pulsed laser systems, including damage criteria for windows and other components in the ultraviolet.

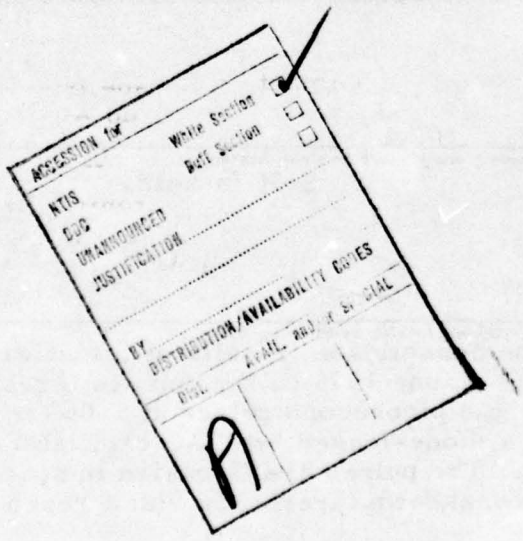

Office of Naval Research

Contract N00014-75-C-0648 NR-372-012

Advanced Research Projects Agency Grant F 44620-75-C-0088

National Aeronautics and Space Administration Grant NGL-22-007-117

DIELECTRIC BREAKDOWN INDUCED BY PICOSECOND LASER PULSES

By

W. Lee Smith, J. H. Bechtel and N. Bloembergen

Technical Report No. 665

October, 1976

The research reported in this document was made possible through support extended the Division of Engineering and Applied Physics, Harvard University by the U. S. Army Research Office, the U. S. Air Force Office of Scientific Research and the U. S. Office of Naval Research under the Joint Services Electronics Program by Contracts N00014-67-A-0298 and N00014-75-C-0648, by the Advanced Research Projects Agency under Grants DAHC 15-73-G-16 and F 44620-75-C-0088, and by the National Aeronautics and Space Administration under Grant NGL-22-007-117.

Division of Engineering and Applied Physics

Harvard University · Cambridge, Massachusetts

DIELECTRIC BREAKDOWN INDUCED BY PICOSECOND LASER PULSES

W. Lee Smith, J. H. Bechtel and N. Bloembergen

ABSTRACT

This report contains the consolidated results of investigations, carried out in the period January 1974 - June 1976 on the damage threshold of transparent optical materials. Single picosecond pulses at 1.06 μm, 0.53 μm and 0.35 μm were obtained from a mode-locked Nd-YAG oscillator-amplifier-frequency multiplier system. The pulses are Gaussian in space and time and permit the determination of breakdown thresholds with a reproducibility of fifteen percent. It is shown that the breakdown thresholds reported here are characteristic of the bulk material, which include nine alkali halides, five different laser host materials, KDP, quartz, sapphire and calcium fluoride. The extension of the damage data to the ultraviolet is significant, because some indication is obtained that two- and three-photon absorption processes begin to play a role in determining the threshold. Throughout the visibile region of the spectrum the threshold is still an increasing function of frequency, indicating that avalanche ionization is the dominant factor in determining the breakdown threshold. This is confirmed by a detailed study of the damage morphology with a high resolution microscope just above the threshold. A detailed discussion of the influence of self-focusing is given, and evidence for beam distortion

below the power threshold for complete self-focusing is presented, confirming the theory of Marburger.

This report constitutes essentially the material of the Ph. D. thesis of Walter Lee Smith, submitted in partial fulfillment of the requirements for the degree of Doctor of Philosophy in the subject of Applied Physics, Harvard University, September 1976.

Chapter I describes briefly previous work on laser induced breakdown and the relationship of the present work to that described in technical report 643, Laser Induced Damage in Solids, May, 1973, by D. W. Fradin. Chapter II gives a description of the picosecond laser system. Chapters III-V give the experimental results of the breakdown at three different wave lengths, in the near infrared, the green and the near ultraviolet. This material is presented mostly in the form of reprints, or of preprints of papers submitted for publication.

The four appendices include reprints of papers on two-photon absorption in semiconductors and multiphoton photo-electric emission of metals, which have also been made possible by the existence of the reproducible picosecond pulse generator.

All this material is assembled in the present report because of its relevance and potential usefulness for high power pulsed laser systems, including damage criteria for windows and other components in the ultraviolet.

TABLE OF CONTENTS

LIST OF FIGURES

LIST OF TABLES

CHAPTER I

INTRODUCTION

The investigation of the properties of matter as a function of the intensity of electromagnetic fields at optical frequencies has been stimulated by the advent of lasers, notably of pulsed lasers with high peak powers. Many nonlinear optical properties have been studied, but the ultimate nonlinearity of any condensed phase is a breakdown process, which transforms the material into a plasma. The damage threshold of optical components is an important limiting factor in the design of high-power laser (HEL) systems. The incipent processes of plasma formation are responsible for the establishment of damage thresholds in transparent optical materials.

The process of irreversible structural alteration of an initially transparent material substance, upon excitation from a sufficiently intense light wave, is known as laser-induced dielectric breakdown.

Although the first pulsed laser operation was reported in 1960 by Maiman,[1] no observations of breakdown processes were made. The early pulsed ruby lasers of 1960 operated in a "burst mode," with an optical output consisting of a collection of many relaxation oscillations of the system. It was not until the technique of Q-switching,[2] which allows temporal concentration of all the stored optical energy into a single output pulse of about 10^{-8} sec duration, was implemented that breakdown was induced by a laser. At the Third International Quantum Electronics Conference in 1963, Maker et al.,[3] who used a Q-switched ruby laser of about 10 MW peak power, made the first communication of laser-induced breakdown. They reported the breakdown of air by focused pulses with an estimated breakdown field strength of 10^8 V/cm. In addition, they reported (without elation) the first laser-induced breakdown in solids, relating that the "experimental factor causing the greatest difficulty was breakdown or burning of the sample" used for their third-harmonic generation experiments. 1965 brought a great improvement in laser peak power production, as Mocker and Collins[4] demonstrated the first simultaneous mode-locking and Q-switching of a ruby laser by use of a saturable absorber. Mode-locking techniques resulted in an

immediate hundred-fold advancement in the peak power obtainable from a laser oscillator. Power levels exceeding the gigawatt mark were then obtainable with modest amplification. Again the blight of breakdown was noted in an original paper, as Mocker and Collins reported that "considerably higher mirror damage was found" when the laser was mode-locked.

Throughout the remaining years of the 1960's, laser-induced breakdown (or laser-induced damage) thwarted laser experimentors, in particular those involved in the development of high-power laser systems. The reason for such longevity of the state of confusion concerning laser-induced damage was the complexity and variety of the involved processes. During those years, progress was slow and investigations were largely empirical in nature. But by 1970, the elements of laser-induced damage problem were being unraveled, due in large part to improvements in laser system mode-control and reproducibility. Laser-induced damage due to absorbing impurities[5] had by that time largely been relegated to a quality control production problem. It was realized that self-focusing of powerful pulses leads to intensification of the light wave in a material, but it was not understood whether self-focusing caused the actual material disruption, as well. Indeed, many different processes were still being discussed as possible breakdown mechanisms, among them photo-excitation of populous impurity levels,[6] stimulated Mandel'shtam-Brillouin Scattering,[7] bulk multiphoton ionization,[8] and electron

avalanche ionization.[9]

In 1971, several advances were made. The introduction of short-pulse TEA CO_2 lasers[10] enabled Yablonovitch[11] to present conclusive evidence that avalanche ionization is the intrinsic physical mechanism which conveys disruptive quantities of infrared light energy to the transparent crystal lattice in laser-induced breakdown. His experiment was conducted with a wavelength (10.6 μm) long enough that self-focusing and multiphoton ionization were absent. Impurity effects were minimized by tight external focusing and further eliminated by microscopic observation. With the identity of the intrinsic breakdown mechanism in hand, further progress in understanding the interplay between self-focusing and breakdown was rapid. Guiliano and Marburger[12] reported direct streak photography observation of pairs of moving self-focal spots in sapphire, verifying theoretical interpretations[13] of time-dependent self-focusing theory. In 1972 Yablonovitch and Bloembergen[14] explained the ubiquitous diameter of the filamentary self-focusing damage track, which is formed by the moving self-foci, with an argument based on avalanche electron production. Fradin *et al.* in 1973 demonstrated that intrinsic laser-induced breakdown at 1.06 μm[15] and at 6943 Å[16] is also an avalanche ionization process, and they[17] measured the laser pulse duration dependence of the breakdown threshold in NaCl.

The experiments listed above (beginning with Yablonovitch)

placed laser-induced breakdown on a firm experimental footing for the spectral region (10.6 μm to 6943 Å) and pulse duration region (~80 nsec to 5 nsec) investigated. However, other areas of research remained uninvestigated and many questions were still unanswered. Laser-induced breakdown in the picosecond pulse regime was not yet studied, except for Fradin's NaCl datum, and it was not known whether avalanche ionization would in fact be effective for such short pulse durations. It was argued that submicroscopic inclusions would dominate the breakdown process for picosecond pulses. And, most intriguing of all, it was not known what would be the light frequency dependence of the breakdown processes. Although avalanche ionization was established as the intrinsic low-optical-frequency breakdown mechanism, multiphoton ionization[18] was known to be an additional intrinsic process in matter that was expected[19] to influence the breakdown process as the light photon energy increased beyond 1.7 eV (the ruby laser value) toward the material optical band gap. These questions addressed the basic physical behavior of transparent matter under intense illumination, yet they also derived considerable practical importance from various high-power laser projects underway then and now. This report recounts three years of experimental effort to answer them.

It is appropriate next to describe the avalanche ionization process that was introduced in the above chronology of laser-induced breakdown. Avalanche ionization breakdown may be

separated for discussion into three stages: 1) initiating electron production; 2) avalanche ionization plasma production; 3) transfer of a damaging quantity of energy from the light wave to the material lattice by the dense, absorbing plasma. The first stage, at low photon energies ($\lesssim$1 eV for a typical insulator), relies on the presence of shallow electron traps (color centers, inclusions, etc.) to yield starting electrons early in the laser pulse. As the photon energy is increased, such shallow traps may be ionized by a single photon, or direct interband multiphoton transitions may be invoked to supply the initiating free electrons. The second stage of the avalanche breakdown process concerns the evolution of an initiating electron in the strong optical light wave. Energy is supplied to the oscillating electron by the optical field. At the same time, the electron undergoes inelastic collisions with the lattice at a rate τ_c^{-1} of roughly 10^{15} sec^{-1}. If the light field is sufficiently strong, the electron will succeed in attaining an energy that will allow it to produce a secondary electron by impact ionization of a lattice atom. The two electrons then may repeat the energization process to produce four electrons, those four may produce eight, and the avalanche has begun. The growth of the avalanche is described by an avalanche ionization coefficient η:

$$N(t) = N_0 \exp\left[\int_{-\infty}^{t} \eta\{E(t')\}\, dt'\right] . \qquad (1)$$

Here N(t) is the number of free electrons per unit volume, N_o is the starting density of electrons, and E(t) is the laser pulse electric field distribution. The function η is highly nonlinear in the electric field E(t).[14] Fig. I.1 illustrates this point. This graph displays E(t), the quantity $\log[N(t)/N_o]$ computed using experimentally derived data for η in NaCl, and also the computed lattice temperature T(t) for a typical pulse from our experiments in NaCl. One observes that the electron distribution is formed predominantly at the peak of the laser pulse, indicating strong nonlinearity and the threshold character of avalanche ionization. The quantity N_o typically has the value 10^{10} cm^{-3} (discussed in Chapter III, Part C, in detail) and it is often observed that breakdown occurs if N(t) exceeds $\sim 10^{18}$ cm^{-3}.

The production of the plasma at the very peak of the pulse serves to separate, for purposes of discussion, stage 2 from stage 3. In stage 3, the plasma absorbs energy from the final portion of the light pulse. The rate of energy absorption by the plasma at a time t, W(t), may be approximated with the Joule heating expression of

$$W(t) = \frac{e^2 \tau_c}{m^*} \frac{|E(t)|^2 N(t)}{1 + \omega^2 \tau_c^2} \quad . \qquad (2)$$

Here e and m* are the electron charge and effective mass, τ_c is the electron momentum relaxation time, and ω is the light angular frequency. As described in Part C of Chapter III,

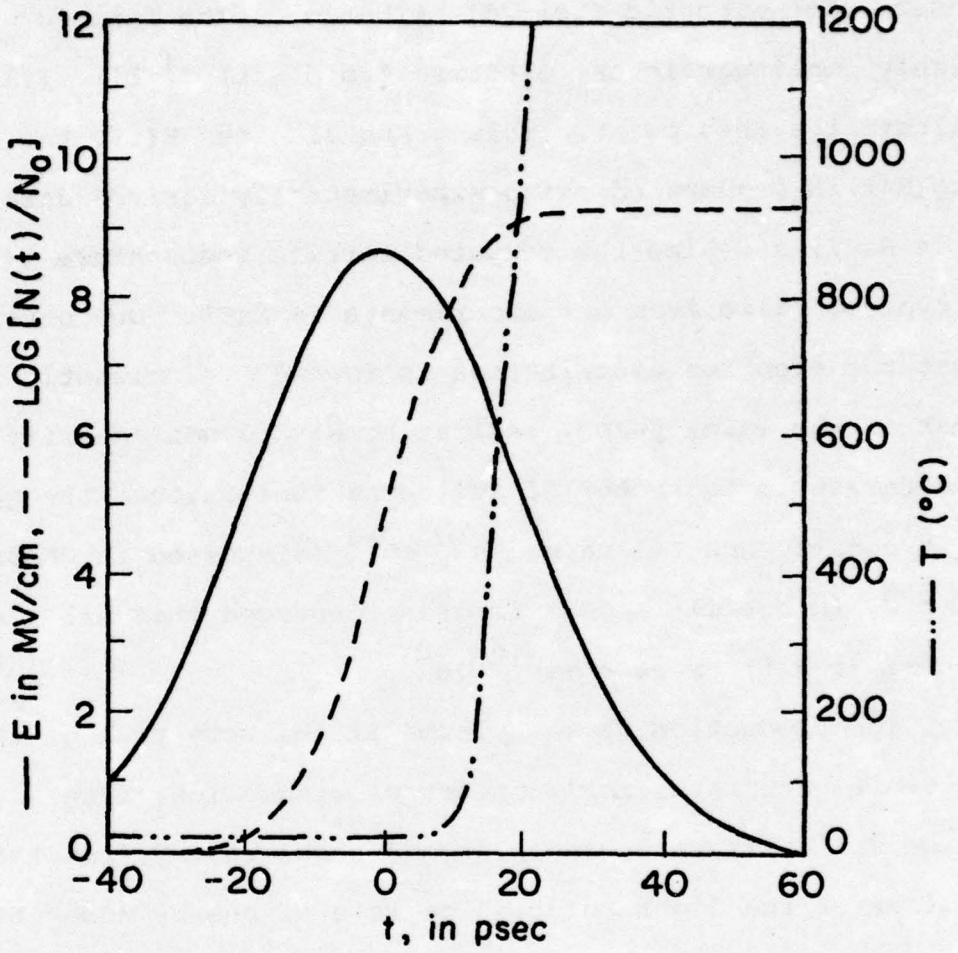

Fig. I.1 Time dependence of the plasma growth [$N(t)/N_o$] and lattice temperature [T(t)] during breakdown induced by a picosecond laser pulse with a Gaussian electric field distribution [E(t)].

with a simplifying neglect of diffusive or radiative thermal loss during the picosecond heating, the temperature of the lattice may be calculated by performing an integration of Eq. (2) over time and using the heat capacity of the material. The T(t) curve of Fig. I.1 is the result of such a numerical calculation. Although the calculation is not accurate above the sample melting temperature (800 °C), it nevertheless illustrates the manner in which lattice heating occurs subsequent to plasma production at the laser pulse peak. If the lattice heating for a given pulse succeeds in melting the lattice over a material volume sufficiently large to be observed under a high-power microscope (as related in Chapter III), then production of breakdown would be recorded for that pulse.

The qualitative picture of the avalanche ionization process given above will serve to acquaint the reader with the basic characteristics. The notions that were introduced will be discussed in detail in following chapters.

The most recent review article on laser-induced breakdown is that by Bloembergen[19] in 1974. That review and references therein, the preceedings[20] of the Conferences on Laser Damage of 1969-1975, and a paper by Holway and Fradin[21] will introduce the reader to the published literature on the subject. References to several other relevant publications which have appeared since 1974 are included in the bibliographies at the end of each of the chapters in this dissertation. For information on DC

breakdown, the reader is referred to the book by O'Dwyer,[22] and to a recent experimental paper[23] and its references.

Chapter II of this report describes the mode-locked laser oscillator-amplifier system which was constructed in our laboratory beginning in late 1973. Construction details which contributed to the stability of the system are reported. A full discussion is given there of the employed techniques for characterization of individual laser pulses. These techniques enabled us to measure optical frequency electric field distributions in absolute units with an accuracy of ± 15%. Several new observations were made during the calibration of our laser system. They were subsequently published and reproductions of those publications are included here as appendices. Appendix I describes the effects of laser pulse depletion, by linear and nonlinear absorption, in the common two-photon fluorescence method of measuring the duration of picosecond laser pulses. If not properly treated, depletion effects lead to erroneous pulse duration measurements. Appendix II describes a nonlinear optical method - the τA technique - for the extraction of an individual picosecond laser pulse duration with only the use of two detectors, an oscilloscope, and a harmonic generation crystal. This technique offers important advantages over other picosecond pulse duration schemes including streak camera photography, two-photon fluorescence, etc. Using the τA technique, we measured the degree of fluctuation

in the pulse duration of our laser which is mode-locked by a saturable absorption dye. That experiment is recounted in Appendix III. Such fluctuation is intrinsic to the saturable absorber mode-locking process,[24] but it had not been considered as a source of error in experiments prior to ours. As demonstration of the utility of the laser system and the characterization techniques described in Chapter II, papers concerning two topics other than breakdown are included as Appendix IV. Part A of Appendix IV describes the observation of a nonlinear photoelectric emission effect from a tungsten metal surface which involved two-photon absorption by the photoelectrons. Careful measurements of the two-photon absorption coefficient in several semiconductors are related in Part B of Appendix IV. The experiments of Appendix IV derived important benefits from the use of low-energy but high-peak-power laser pulses.

The description of the central experiments of this research begins with Chapter III. That chapter describes our research at the 1.064 μm wave length, and it is composed of three parts. The first (Part A) is a paper recounting a measurement of the breakdown threshold, with our nominally 30 picosecond pulses, in fourteen transparent solids. These solids include several practically important optical materials (KH_2PO_4, a laser glass, a laser crystal, SiO_2 and CaF_2) in addition to nine alkali-halides. The data for the alkali-

halides is compared with previous data taken with nanosecond laser pulses by Yablonovitch[11] and Fradin et al.[15,16] to show that avalanche ionization of electrons is indeed the breakdown agent at 1.064 μm, even for picosecond pulses. Simultaneous measurements of the nonlinear refractive index are obtained and compared with other published values, to demonstrate that our experiment accounted properly for self-focusing. Part B of Chapter III is a follow-up experiment in four additional state-of-the-art laser component materials. Part C of Chapter III describes one final aspect of the 1.064 μm laser-induced breakdown study, its morphology. It was discovered that the picosecond breakdown morphology consists of a collection of micron-sized, spatially distinct sites, localized along the focal axis. Each of the microsites is the vestige of a tiny plasma which grew from a small number, perhaps only one, of electrons which were present in shallow traps when the laser pulse traversed the focal region. Because of the short laser pulse duration, the plasma sites did not grow to the point of overlap. The observed density of sites allowed us to measure for the first time the actual density of free or slightly bound electrons which may serve to launch an avalanche inside a transparent dielectric. Photographs of the damage sites are presented in this part of Chapter III.

Chapter IV recounts our effort to extend the work of Chapter III to a shorter wavelength than had been studied

previously. By frequency doubling the 1.064 μm pulses in a noncritically phase-matched crystal, we obtained 5321 Å pulses with a spatio-temporal waveform as noiseless and reproducible as at the fundamental wavelength. Self-focusing constraints in this experiment were severe. Nevertheless, breakdown thresholds were obtained in six materials. Comparison of the thresholds at the two wavelengths showed a most exciting result: for the small band gap material KH_2PO_4, the threshold at 5321 Å was less than the infrared threshold, indicating for the first time a quantitative observation of multiphoton (three-photon, in this case) absorption assistance to the avalanche. For the other materials, the 5321 Å threshold equaled or exceeded the infrared threshold, in a systematic fashion, providing conclusive data also for the first time for a frequency-dependent increase in the threshold of avalanche ionization. This increase was predicted for some time,[19] as was the effect of multiphoton absorption on the threshold. Morphology of this breakdown showed consistently that the operative process at 5321 Å is avalanche ionization for the large band gap materials. Even for KH_2PO_4, the morphology confirmed that an avalanche dominates the breakdown process in stages two and three, as discussed earlier. The experimental results concerning the frequency dependence of the two intrinsic breakdown mechanisms constitute the highlights of Chapter IV.

Chapter V describes our investigation of breakdown at 3547 Å in the ultraviolet wavelength range. For the necessary frequency summing process to produce this wavelength, no material is known which allows noncritical phase-matching to be achieved. Severe difficulties were therefore caused by pulse spatial distortion due to walk-off, and by self-focusing, in the nonlinear generation crystal. These distortions, time- and power-dependent, coupled with the smallness of the critical power for self-focusing in the samples, did not permit precise breakdown threshold interpretation to be made from the data at this wavelength, as discussed in Chapter V. Nevertheless, the data obtained at 3547 Å verified qualitatively the frequency dependent behavior first discussed in Chapter IV.

REFERENCES

1. T. H. Maiman, Phys. Rev. Lett. 4, 564 (1960).

2. R. W. Hellwarth, in Proc. of Third Int. Conf. on Quant. Electr., P. Grivet and N. Bloembergen, eds. (Columbia Univ. Press, New York, 1964), p. 1203.

3. P. D. Maker, R. W. Terhune, and C. M. Savage, In Proc. of Third Int. Conf. on Quantum Electronics, P. Grivet and N. Bloembergen, eds. (Columbia Univ. Press, New York, 1964), p. 1559.

4. H. W. Mocker and R. J. Collins, Appl. Phys. Lett. 7, 270 (1965).

5. R. W. Hooper and D. R. Uhlmann, J. Appl. Phys. 41, 4023 (1970).

6. R. W. Hellwarth, in Damage in Laser Materials, edited by A. J. Glass and A. H. Guenther, NBS Spec. Pub. No. 341, p. 67.

7. B. M. Ashkinadze, V. I. Vladimirov, V. I. Likachev, S. M. Ryvkin, V. M. Salmanov, I. D. Yarshetskii, Zh. Eksp. Teor. Fiz. 50, 1187 (1966) [Sov. Phys. JETP 23, 788 (1966)].

8. V. A. Pashkov and G. M. Zverev, Zh. Eksp. Teor. Fiz. 51, 777 (1966) [Sov. Phys. JETP Lett. 24, 516 (1967)].

9. A. Wasserman, Appl. Phys. Lett. 10, 132 (1967); G. M. Zverev, T. N. Mikhailova, V. A. Pashkov, and N. M. Solov'eva, Zh. Eksp. Teor. Fiz. 53, 1849 (1967) [Sov. Phys. JETP 26, 1053 (1968)].

10. A. J. Beaulieu, Appl. Phys. Lett. 16, 504 (1970).

11. E. Yablonovitch, Appl. Phys. Lett. 19, 495 (1967).

12. C. R. Guiliano and J. H. Marburger, Phys. Rev. Lett. 27, 905 (1971).

13. Y. R. Shen and M. M. T. Loy, Phys. Rev. 3, A2099 (1971).

14. E. Yablonovitch and N. Bloembergen, Phys. Rev. Lett. 29, 907 (1972).

15. D. W. Fradin, E. Yablonovitch, and M. Bass, Appl. Opt. 12, 700 (1973).

16. D. W. Fradin and M. Bass, Appl. Phys. Lett. 22, 206 (1973).

17. D. W. Fradin, N. Bloembergen, and J. P. Lettelier, Appl. Phys. Lett. 22, 635 (1973).

18, L. V. Keldysh, Zh. Eksp. Teor. Fiz. 47, 1945 (1964), [Sov. Phys. - JETP 20, 1307 (1965)].

19. N. Bloembergen, IEEE J. Quant. Electr. QE-10, 375 (1974).

20. Proceedings of Conferences on Laser-Induced Damage in Optical Materials, A. J. Glass and A. H. Geunther, eds.:

1969 - ASTM Spec. Pub. No. 469, ASTM, Philadelphia, Pa;

1970-1975 - NBS Spec. Pub. Numbers 341, 356, 372, 387, 414, 435, resp., U. S. Govt. Printing Office, Washington, D. C.

21. L. H. Holway, Jr. and D. W. Fradin, J. Appl. Phys. 46, 279 (1975).

22. J. J. O'Dwyer, The Theory of Electrical Conduction and Breakdown in Solids and Dielectrics (Clarendon, Oxford, 1973).

23. J. L. Smith and P. P. Budenstein, J. Appl. Phys. 40, 3491 (1969).

24. P. G. Kryukov and V. S. Letokhov, IEEE J. Quant. Electr. QE-8, 766 (1972).

CHAPTER II.

LASER SYSTEM

A. Introduction

This chapter contains a description of the diffraction-limited, mode-locked Nd:YAG laser system which was constructed in our laboratory beginning in late 1973. The heart of this 1.064 μm laser system is a passively Q-switched and mode-locked Nd:YAG oscillator, which produces a train of roughly 20 optical pulses, each of 30 picosecond duration. A single pulse is separated from the pulse train by a fast Pockels cell electro-optic shutter. The use of a single picosecond pulse optical source, rather than an entire pulse train, is greatly preferred for straightforward data analysis and attainment of conclusive results. The final elements of the laser system are two single-pass, Nd:YAG amplifiers. These amplifiers provide an energy boost of up to roughly 100, enabling a peak power of 3×10^8 watts to be achieved in a single pulse. Peak powers of this magnitude make possible the efficient conversion of this 1.064 μm light into the visible and ultraviolet harmonic wavelengths. We have observed power conversion efficiency of ~50% to 5321 Å, ~20% to 3547 Å, and ~15% to 2661 Å, limited by the damage properties of the nonlinear crystals. Because both the spatial and temporal profile of these optical pulses is Gaussian (with some

reservation at 3547 Å), calculations for extraction of results from data, whether analytic or numerical, are often simplified. The Gaussian spatial profile is convenient for focusing the light pulses to achieve higher intensity since the spatial profile remains Gaussian while only its width changes. The focused pulses from this laser system make available intensity levels higher than that sustainable by any solid, liquid, or gaseous form of matter: all are converted to the plasma state at such excitation levels. However, the utility of this laser system stems not from the available raw power, but from the reproducibility and careful characterization of the waveform. These two qualities will be discussed further in the last section of this chapter and in later chapters as well.

The following sections of this chapter contain details of the laser system components, operation, and performance.

B. Mode-locked Laser Oscillator

1. Resonator Design

The Brewster configuration resonator is diagrammed schematically in Fig. II.1. Between the two reflectors are positioned the laser rod, mode-locking cell, and spatial mode selecting aperture. The front and rear reflectors are dielectric-coated glass substrates with reflectivities of 46% and 100%, respectively. The reflecting surface of the rear mirror is concave with a 3 m radius of curvature. This

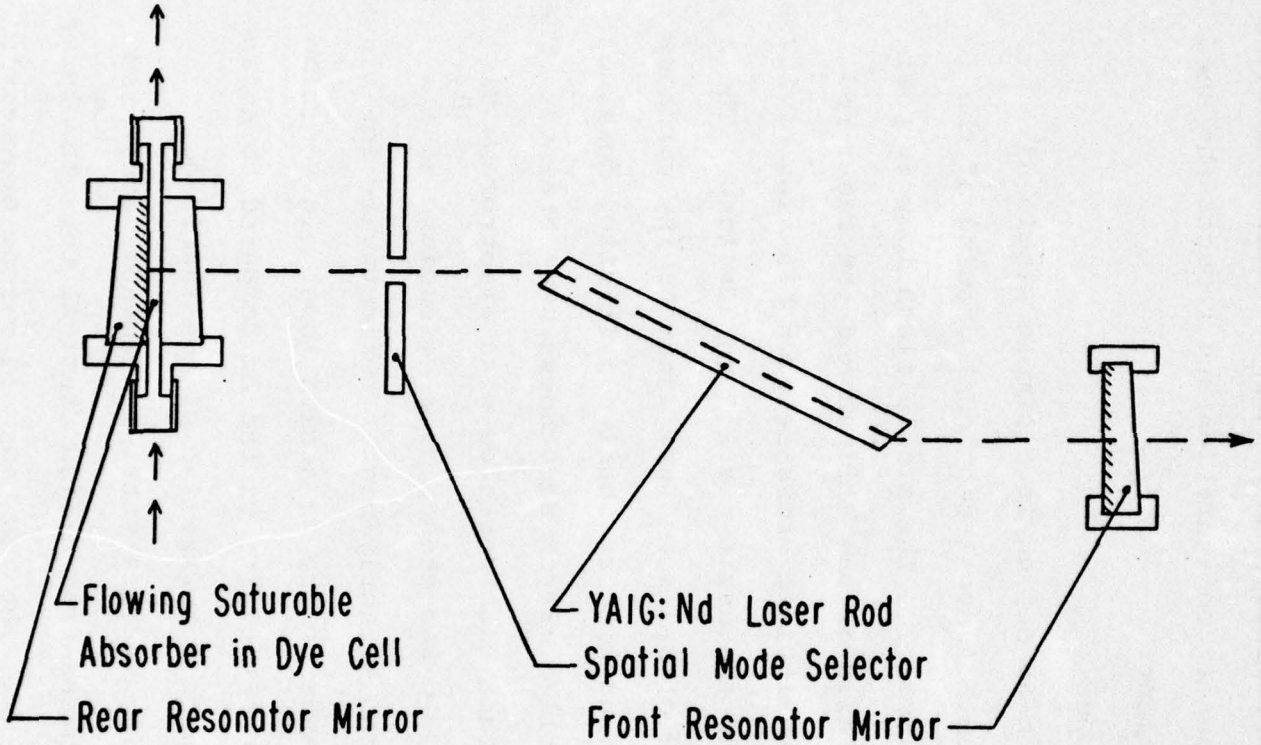

Fig. II.1 Schematic illustration of the oscillator configuration of the YAlG:Nd mode-locked laser system.

curvature relaxes appreciably the alignment tolerances found in a flat-flat resonator configuration and reduces the need for frequent realignment.

2. Oscillator Head

The oscillator head design is a simple single 63^{o} ellipse configuration. A cross-sectional drawing of the head is shown in Fig. II.2. The single flash lamp is positioned at one focal axis of the ellipse and the laser rod at the other. The elliptical cross-section has axes of 2.750 and 2.450 inches, and the cavity is 2.0 inches long. The head pieces were machined of brass and the inner cavity surfaces were then hand polished with successive grit sizes down to jeweler's rouge, until a mirror smoothness was obtained. The cavity pieces were then electroplated with electroless Ni and then with Au. Gold was chosen over Ag because of its greater durability and slightly higher reflectivity for light in the absorption bands of the Nd active ions. In addition, the slightly lower reflectivity of the Au compared to Ag in the ultraviolet reduces solarization of the laser rod.

The laser rod itself is a Yttrium Aluminum Garnet rod doped with Nd, purchased from Allied Chemical Co. The laser wavelength is 1.064 μm. The rod ends are cut at Brewster's angle with respect to the rod cylindrical axis, for three reasons. 1. The Brewster configuration alleviates the frequency-selective properties of pairs of parallel, normal

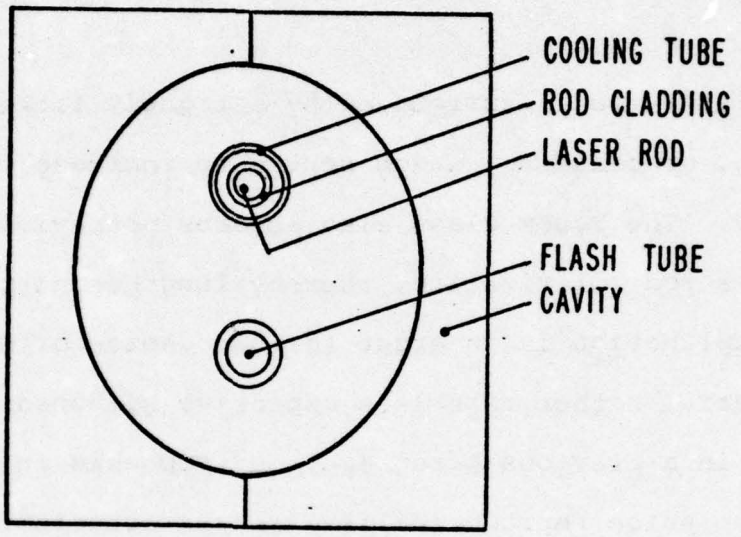

Fig. II.2 Illustration of the single-ellipse configuration of the laser heads.

surfaces inside the resonator. Frequency selectivity would be deleterious for the production of bandwidth-limited output pulses. 2. It removes the need for low-reflectivity dielectric coatings, with their attendant damage susceptibility, on the rod faces. 3. It results in 100% linearly polarized output radiation.

The laser rod is surrounded by a tightly fitted Pyrex glass tube, or cladding, which serves to increase the pumping efficiency. The Pyrex glass also absorbs ultraviolet light and reduces rod solarization, thereby lengthening rod lifetime.

An explanation is in order for our choice of Nd:YAG as a laser material rather than less expensive Nd-doped glass. As mentioned in a previous paragraph, our emphasis in this work has been on pulse reproducibility and characterization, in order to maximize control in our experiments. Nd:glass mode-locked lasers are now well known to be less suited for that class of application, for the following reason. Because the Nd^{+3} ion fluorescence linewidth is broadened substantially more by host interaction with glass than with crystalline YAG, the Nd:glass oscillator is capable of producing pulses correspondingly shorter in duration than a Nd:YAG oscillator. The Nd:glass pulses are typically, in initial states, shorter even than the response time of the dye used to mode-lock the laser. This response time is reportedly about 7 psec.[1] Therefore the Nd:glass pulses are not smoothed and transformed, by the many

successive passages through the bleachable dye, into a standard final waveform to the degree of Nd:YAG pulses. The result is that the temporal waveform of Nd:glass mode-locked laser pulses generally is not smooth but has noise-like structure of picosecond scale which fluctuates from shot to shot. Further problems of Nd:glass involve temporal broadening due to self-phase modulation which progressively increases the width of successive pulses in the same pulse train. These factors render Nd:glass markedly unsuited for our purposes. A further inconvenience of Nd:glass is that its lesser thermal conductivity limits the firing rate to about 1 pulse per second, whereas our Nd:YAG system can be operated at 30 pulses per second. This fast rate is beneficial for alignment procedures, as well as for data recording.

Our Nd:YAG rod is cooled by distilled H_2O which flows through a 1 mm thick annular space between the cladding and an outer Pyrex glass tube. The flow velocity is approximately 10 cm/sec and the H_2O temperature is maintained at 20 °C ± 0.1 °C by a Lauda-Brinkman K2/R thermo-regulating circulator. No other elements are cooled with this circuit. This minimal thermal load allows the thermo-regulator to operate very sensitively to control the rod temperature for increased stability. The Pyrex glass tubes were bonded to the gold-plated brass end pieces with a transparent epoxy (Eccobond 24).

The oscillator flash lamp, and those for our amplifier

heads, were manufactured by ILC Technology (#L-1419) and are xenon-filled. Xenon lamps are superior to krypton-filled lamps, an alternate for pumping Nd, for use in high-current, pulsed operation.[23] They also offer longer lifetime, approaching 10^6 shots. The lamp dimensions are 4 mm inner bore diameter and 2.125 inch cathode-anode separation.

The oscillator flashlamp and both the rods and lamps of the dual amplifiers are water cooled by a circuit entirely separate from that for the oscillator rod, as mentioned above. A high-capacity industrial water cooler (Blue M #PCC-3455C) maintains a 20 °C temperature. This cooling system has the capability to service several additional amplifier stages or adjacent lasers.

3. Mode-locking Dye Cell

A schematic illustration of the construction of the dye cell is shown in Fig. II.1. The cell is of so-called "contacted" design, meaning that the flowing sheet of dye is in physical contact with the rear, 100% reflective mirror. This arrangement[3] is optimum for the suppression of satellite structure in the mode-locked output pulse train. The sheet of dye solution is pumped upward against gravity and flows in a thin (0.5 mm thickness) sheet between the two confining surfaces of the rear reflector and the other uncoated substrate. The dye solution itself is Kodak #9860 saturable absorber diluted with laser-grade 1,2 - dichloroethane. The dye has a relaxation time of

7 picoseconds and a saturation (bleaching) intensity of 60 MW/cm^2. The proper concentration (22 ml of dye with 100 ml dichloroethane) results in a low intensity transmission factor (through the cell) of about 0.7 at 1.064 μm. The other elements of the dye circuit, which are not included in Fig. II.1, are the dye pump, dye reservoir, filter, and flow lines. Black, opaque polyvinyl flow tubing was used to shield the dye from ambient UV room light which would hasten its degradation. The Millipore teflon filter, installed in the circuit just before the dye cell, removes particulate matter from the pump gears, etc. Without the filter, the 0.5 mm channel in the dye cell is the most restrictive part of the circuit, and the light-absorbing, particulate matter collects and leads quickly to the damage of the dielectric coating. The stainless-steel reservoir is never completely filled, allowing the air volume to act as a cushion to damp fluctuations in the flow velocity.

4. Flashlamp Pulsed Power Supply

The two power supplies including the pulse-forming networks used to fire the flashlamps in our laser system were manufactured by ILC Technology. This supplier also makes our flashlamps, and in fact, the power supplies are designed from the beginning for the exact firing characteristics of the L-1419 xenon flashlamps. Two power supplies are used here, one for the oscillator lamp and one for the series pair of amplifier lamps. The maximum repetition rate is 30 pulses per second, limited

by the onset of "latch-on" or faulty continuous lamp energization. This rather high repetition rate is made possible by special recharge delay circuitry designed to inhibit "latch-on". The circuitry begins recharge only after a sufficient time has elapsed for the ionized gas in the lamp to recombine to the neutral state. The oscillator (amplifiers) power supply characteristics are a maximum energy per pulse of 20 (50) joules, a pulse width of 150 (200) μsec, a maximum continuous power of 1500 (2000) watts, and a charging voltage of 0 to -2kV.

C. Pockels Cell Single Pulse Selector

As mentioned in the introduction to this chapter, in order to use mode-locked lasers for many applications, it is desirable to employ only one of the pulses from the characteristic train of pulses. If the entire train is used in an experiment, the output signal is usually an average or accumulation over the many pulses. Unambiguous and precise conclusions are at least more difficult and often impossible to draw from such data. Therefore we employ an electrooptic shutter after our oscillator to extract from the pulse train a single picosecond pulse.

The general technique for single pulse selection makes use of the different transmission factor of an optical polarizing element for the two orthogonal polarization states of the laser light. An electrooptic device is positioned between

a pair of crossed polarizers. Unless a proper voltage is applied to the electrooptic device, no light passes through the second polarizer. When given the proper voltage pulse, the electrooptic element rotates the light polarization by $\lambda/2$, allowing it to proceed through the second polarizer unattenuated.

The electrooptic device may employ either the Pockels electrooptic effect or the Kerr electrooptic effect. Because of the toxicity of the nitrobenzene fluid normally used in a Kerr cell and the excessively high required voltage, we have employed a Pockels cell electrooptic shutter in our apparatus.

The Pockels effect is a linear electrooptic effect that occurs in all piezoelectric crystals. The ideal transmission T of a Pockels cell is given by

$$T = T_o \sin^2(\pi n_o^3 r_{63} V/\lambda) \quad . \tag{1}$$

Here n_o is the ordinary refractive index of the electrooptic material (in our case, KD_2PO_4), r_{63} is the material linear electrooptic coefficient, λ is the light vacuum wavelength, and V is the applied voltage. From this expression, one observes that the condition for full transmission (that for $\lambda/2$ polarization rotation) is obtained with an applied voltage of

$$V_{\lambda/2} = \lambda/2n_o^3 r_{63} \quad , \tag{2}$$

known as the "half-wave" voltage. This quantity for KD_2PO_4 (KD*P) at 1.06 μm is approximately 6000 volts.

The Pockels cell shutter used in our experiments is illustrated schematically in Fig. II.3. A high voltage power supply (HV) charges a transmission cable (C1) through a charging resistor (R1) of 1.1×10^6 ohms. This voltage V (≃ 12,000 volts) is applied to one side of the electrode pair in the spark gap (SG), the other side of which is at ground potential. High-pressure nitrogen gas was used to increase the dielectric breakdown voltage limit of the gap. When the focused initial pulses of the pulse train enter the shutter, their polarization is rotated by λ/2 by the half-wave plate (WP), allowing them to pass through to polarizer P2. There the pulses are deflected and focused into the electrode gap region where they initiate breakdown. A voltage pulse of V/2 then travels through cable C2 for a duration $2\ell_1/v$, where ℓ_1 is the length of cable C1 and v is the propagation velocity of the cable. (C1, C2, C3 are all 50 ohm, RG-8/U cable.) While this voltage pulse is traveling across the Pockels cell PC, itself a 50 ohm impedance, traveling-wave device, the polarization of any light passing through it is rotated by λ/2. The length of the cable C1 is made so that only one pulse can be switched out from the pulse train, as expressed by the condition $2\ell_1 v^{-1} \lesssim 2L/c$. Here 2L is the optical round-trip path length of the laser oscillator, and c is the vacuum

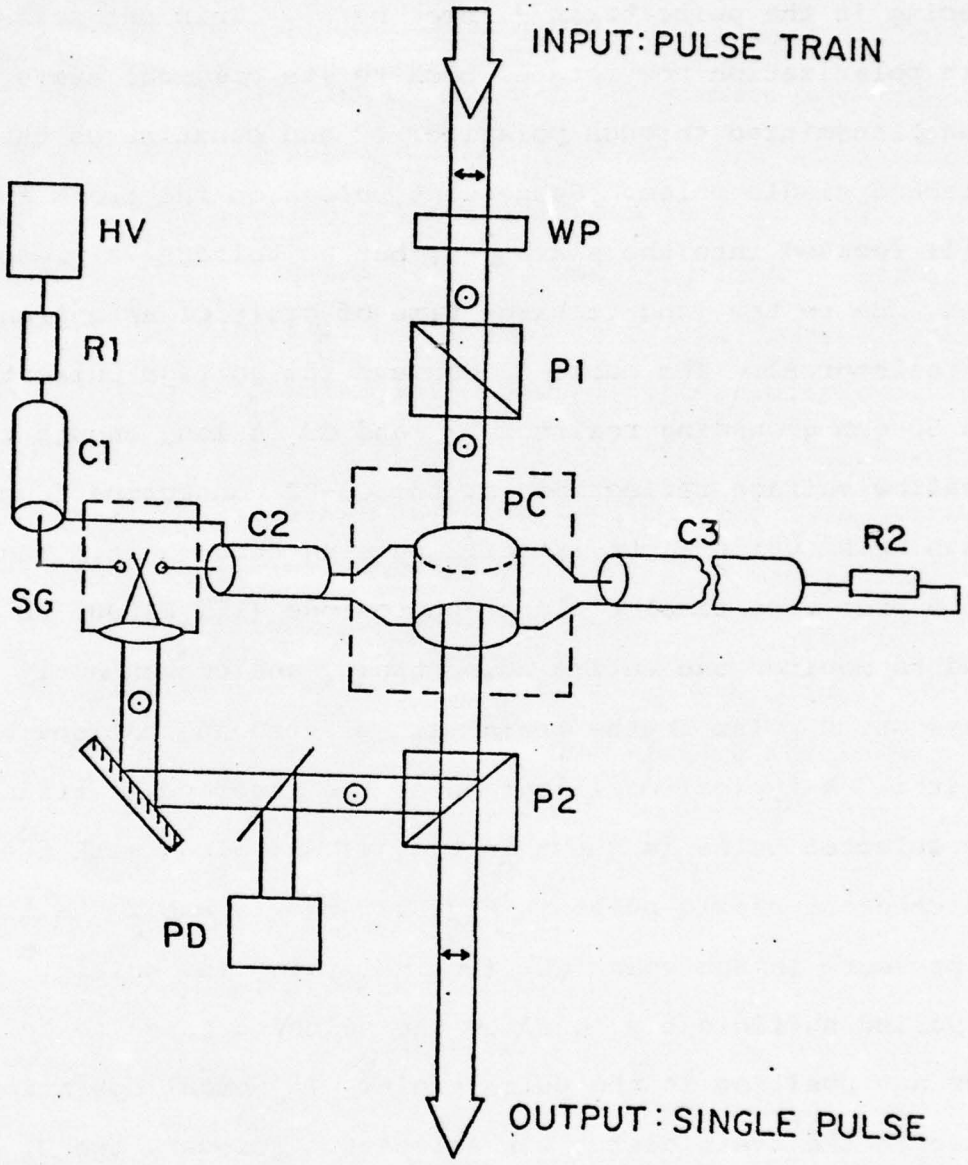

Fig. II.3 Schematic diagram of the Pockels cell single pulse selector used in the laser system. Notation: WP, half-wave plate; P_1 and P_2, Glan prism polarizer; PC, traveling-wave configuration KD_2PO_4 Pockels cell; C1-C3, 50-ohm coaxial cables; R1, 10^7 ohm charging resistor; R2, 50 ohm load resistor; SG, high-pressure, N_2-filled, laser-triggered spark gap; PD, photodiode detector; HV, high voltage supply.

speed of light. The right side is the temporal interpulse spacing in the pulse train (7 nsec here). This one pulse with polarization now rotated back to its original state is then transmitted through polarizer P2 and constitutes the selected single pulse. Subsequent pulses on the train are still focused into the spark gap, but no voltage is present then, due to the long recharge time of cable C1 as guaranteed by resistor R1. The cable C3 conveys the voltage pulse to the 50 ohm grounding resistor R2, and C3 is long enough to disallow voltage reflections at the C3-R2 connection from reaching PC while light is still passing through it. The fast (<0.5 nsec rise time) biplanar photodiode (ITT F4000) PD is used to monitor the entire pulse train, and conveniently displays which pulse in the train was selected and excised by the shutter. A typical oscillograph of the laser pulse train minus the selected pulse is shown in Fig. II.4a, along with the actual switched-out single pulse in Fig. II.4b. It was found that the N_2 pressure in the spark gap (nominally 160 lb./sq. in.) could be varied sufficiently to allow the selected pulse to be taken from any position in the pulse train. In normal operation the pulse in the train center was selected. However, the N_2 pressure could be used in some cases to make adjustments of the single pulse intensity level. (This technique would not be possible with a Nd:glass laser because pulses in different positions in the train have widely different duration and substructure.)

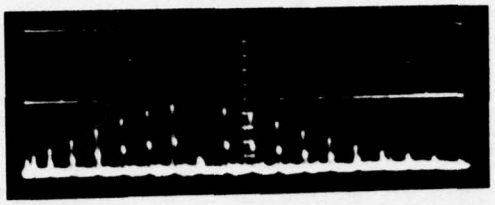

a. Oscillograph of mode-locked pulse train after switch-out (2 nsec/div.).

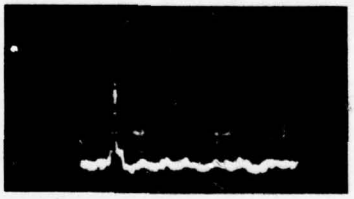

b. Oscillograph of single selected pulse(0.5 nsec/div.).

Fig. II.4

Temporal Waveforms

The jitter, or fluctuation, in the selection position of our shutter was typically 15-30 nsec, or 2 to 4 pulse positions. The actual Pockels cell used in our system is a product of Lasermetrics Corp. (Model 1071), and has a cylindrical ring electrode (CRE) geometry, as indicated in Fig. II.3. This configuration provides a more uniform transmission across the electrooptic crystal face at a given voltage than does the more conventional end-plate electrode geometry. In addition, the CRE geometry reduces the cell capacitance and yields a faster cell response time (in our case, ~1 nsec), important for clean switch-out of a single pulse.

D. Dual Amplifiers

The final stages of our laser system are two Nd:YAG, single-pass, traveling wave amplifiers. These amplifiers provide a maximum power gain of about 100 for the single pulse which is selected by the Pockels cell. The amplifiers have operated at this excitation level for a period of almost three years without suffering any damage.

The amplifier heads are different from the oscillator head in only one respect. The Nd:YAG rods (from the same supplier and of the same size as the oscillator rod) have faces cut, not at Brewster's angle, but at a small wedge angle of 6^{o}. Because the amplifiers are single-pass devices, the loss from the face reflectivity is not important compared to the alignment ease of the wedge cut over the Brewster cut.

The faces are cut at 6^{o} rather than 0^{o} for two reasons. The small angle eliminates problems caused by back propagation of intense reflections into the Pockels cell, etc. And the 6^{o} wedge angle was calculated to be just large enough to suppress low-order parasitic modes which would otherwise be able to oscillate inside the rod between the faces, thereby decreasing useable gain.

The cooling system and power supply systems were described in previous paragraphs. Although it was not necessary for any experiments undertaken thusfar, a different arrangement of these amplifiers could be introduced to provide an additional gain factor of perhaps 8 to 10. Because the first amplifier is not at all saturated by the single pass of the single pulse, it could be used instead in dual-pass mode. The second amplifier would remain in single-pass formation. This overall triple-pass amplifier chain would then provide over 10^{9} watts in a single 30 psec output pulse.

E. Laser Pulse Characterization

For a laser pulse which is both spatially and temporally Gaussian, the intensity waveform I(r,t) in a plane normal to the propagation direction is expressible as

$$I(r,t) = I_{o}\, e^{-(r/\rho)^{2}}\, e^{-(t/\tau)^{2}} \quad . \qquad (3)$$

Here r is the radial coordinate of distance from the

propagation axis and t is the time variable. Thus the intensity waveform is specified entirely by the three parameters I_o, ρ, and τ, which are the peak intensity, the spatial radius, and temporal radius, respectively. This condition is true for focused, as well as for unfocused, Gaussian laser pulses. Therefore the task at hand in order to specify quantitatively $I(r,t)$ is to record I_o, ρ, and τ values for each laser pulse. The techniques for these three measurements which we have developed and employed in our experiments are described in the following paragraphs. Because the physical processes studied in our experiments (as discussed in later chapters) are highly nonlinear, even exponentially nonlinear, in the intensity, precise knowledge of the pulse parameters is a solemn necessity. The unusual care that was exercised in the accurate determination of the individual pulse parameters in our experiments was of fundamental importance for our observations.

1. Measurement of Pulse Spatial Dimension, ρ

The measurement of the unfocused pulse radial dimension offered the least difficulty of the three parameters. In initial experiments, measurement of the spatial profile was made with a multi-lens camera photographic technique[4] which is independent of all film exposure nonlinearity. Photodensitometric analysis of the data film yielded the parameter ρ. As one would expect, fluctuations in the spatial profile

and thus the area A ($=\pi\rho^2$) were small (unobservable at 1.06 μm), as the amplifier stages were not used in the nonlinear, saturation range. Therefore, a measurement (or rather, the average of several measurements) of the pulse area needed to be performed only once for an experiment, rather than for every shot. This was fortunate, considering the time involved in the photographic recording and analysis.

In later experiments, far greater accuracy in the measurement of ρ was made possible by the purchase of an electronic device, a (Reticon) self-scanning photodiode array. This monolithic integrated circuit linear array is composed of 256 individual Si photodiodes, each of area .001 in. x .001 in., spaced by .002 in. (50.8 μm). Associated circuitry repetitively scans the 256 diodes (at 10 kHz) in order and processes the individual diode light signals into a serial output format. This serial output signal is fed into an oscilloscope and provides a direct display of the distribution of light illuminating the array over the scanning period. The array is in practice illuminated with a single pulse and an oscillograph is made. The pulse area is obtained immediately and to an accuracy of better than 10%. The spectral response of the device is such that it is useful at 1.064 μm and at the second-, third-, and fourth-harmonic wavelengths. The photodiode array has been invaluable in another respect in experiments using the harmonic wavelengths, especially the third-harmonic. The

array was used to phase-match the KH_2PO_4 third-harmonic generation crystal to the particular angle which yielded the smoothest ultraviolet spatial waveform.

2. Measurement of Pulse Temproal Duration, τ

a. Measurement of Average Duration, $\langle\tau\rangle$

A major series of experiments in our characterization of the laser pulse output concerned the measurement of the average temporal duration, τ. Specifically, τ is the 1/e half duration of the intensity. Two techniques were used for these measurements: i) a second-harmonic autocorrelation (SHAC) technique,[5] and ii) a two-photon fluorescence (TPF) technique.[5] Fig. II.5 illustrates the optical arrangements for the two techniques. In both techniques, the incident 1.064 μm pulse is split into two equal parts which are then recombined to interact in a nonlinear medium. In the SHAC technique, Fig. II.5a, an optical delay is imposed on one of the separated pulses by a movable mirror in one arm of the interferometer. The two pulses then travel collinearly through a nonlinear second-harmonic generation crystal (KH_2PO_4). There the two infrared pulses produce 5321 Å light with polarization orthogonal to the infrared light. In addition to a constant background signal due to the individual pulse harmonic generation, there is a correlational contribution which is proportional to the temporal overlap of the two pulses. The amount of second-harmonic light produced is measured by detector D.

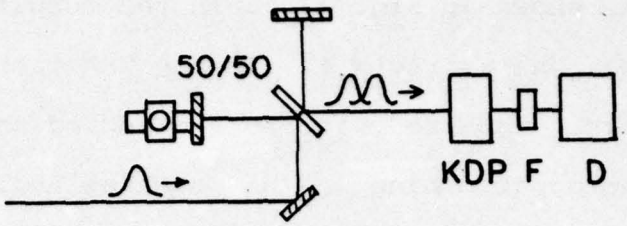

a. SECOND HARMONIC GENERATION AUTOCORRELATION TECHNIQUE

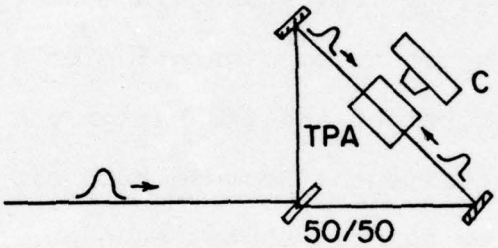

b. TWO-PHOTON FLUORESCENCE AUTOCORRELATION TECHNIQUE

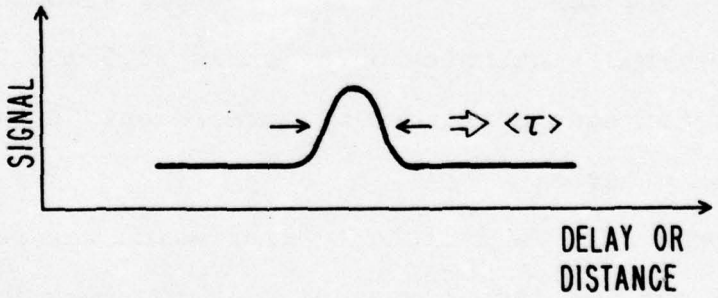

c. AUTOCORRELATION DATA

Fig. II.5 Schematic diagram of two conventional experimental methods for measuring the duration of picosecond laser pulses, and an illustration of their autocorrelation output data.

If the detected harmonic light is plotted versus optical delay, a curve as shown in Fig. II.5c is the result. From the width of the peak, one extracts τ. In the TPA technique, no delay is necessary. The two pulses are directed anticollinearly through a two-photon absorbing medium, such as Rhodamine 6G, and the fluorescence spatial pattern is photographed by a camera. Photodensitometric analysis of the film again yields a curve as shown in Fig. II.5c, and again τ is extracted from the peak width. An important consideration of the contrast ratio between the peak height and the background height is also necessary in these experiments. Because both experiments require many tens or even a few hundred shots, each produces a measure of the average duration, $\langle\tau\rangle$. The significance of that observation will be mentioned below. The result of both experiments was that for our laser $\langle\tau\rangle = 18.0 \pm 1.8$ picoseconds and the full-width-at-half-intensity duration is 30.0 ± 3.0 picoseconds. This result has been confirmed by more recent, direct experiments[6] using streak cameras.

In Appendix I, we include a paper which was published as a result of our TPF investigations. In the work in that paper, account for the effects on the contrast ratio from one- and/or two-photon attenuation of the laser pulses in the TPF medium was included for the first time. These observations were important for the extraction of accurate $\langle\tau\rangle$ values from the data.

b. Measurement of Individual Pulse Duration, τ

The previous section described our measurements of the average duration $\langle\tau\rangle$. For a laser that is mode-locked with a saturable absorber, knowledge of $\langle\tau\rangle$ is insufficient for many purposes because the single pulse duration, τ, fluctuates substantially from shot to shot. Saturable absorber mode-locking is intrinsically a stochastic process. Letokhov and others developed a successful model[7] of the process by beginning with the realization that, prior to absorber bleaching, the radiation in the laser resonator is well characterized as a narrow-band Gaussian random process. This behavior results from the beating of the many modes which are brought above lasing threshold and which lack a deterministic phase relation. The well developed formalism of Gaussian random processes[8] then immediately yields probabilistic expressions for the parameters of the noise radiation, such as the most probable noise spike duration, the spread therein, etc. It is the distribution of probability for the temporal width of the most intense noise spike, in the initial stages of pulse development, which results in a distribution of duration for the output pulses.

Thus one must detect and account for this variation in duration from shot to shot if he is to arrive at accurate knowledge of the single pulse intensity distribution. Prior to our experiments, the only way in which this fluctuation

had been considered was by direct observation with streak photography. Only large laboratories have such equipment. Therefore we developed a nonlinear optical technique for the indirect monitoring of the pulse duration, which requires minimal equipment and has several advantages over direct streak camera photography for experiments such as ours. This technique, called the τA technique, is described in a published paper which is included in full as Appendix II. The τA technique involves the simple measurement of two energy signals with photodiodes for each pulse. One signal is the energy $\mathcal{E}_f$ in a sample of the laser pulse, and the other is the energy $\mathcal{E}_{sh}$ at the second-harmonic wavelength which was obtained by sending a second sample through a KH_2PO_4 crystal. It is shown in Appendix I that the ratio of $\mathcal{E}_f^2 / \mathcal{E}_{sh}$ is proportional to the individual pulse duration τ and to the pulse area A. Fortunately, for our laser we could treat A as a constant in most cases. By recording the signals $\mathcal{E}_f^2 / \mathcal{E}_{sh}$ for each of the shots in an experiment and forming their average, one may renormalize that data into invididual pulse duration data, in units of pico-seconds. This τA technique was invaluable for obtaining accurate single pulse intensity data in all our subsequent experiments, and is mentioned further in later chapters.

To make use of the τA technique itself to investigate the statistical nature of the pulse duration, an experiment was performed to measure the pulse duration probability function of our laser. This experiment is also described fully in a

paper, presented as Appendix III. In that experiment the pulse duration probability function was found to be approximately 20 picoseconds wide, indicating pulses of about 20 to 40 picoseconds are produced by our laser. This degree of fluctuation has been since verified directly with streak photography by workers at the Naval Research Laboratory.[9] It is evident that such wide variation in one of the three pulse parameters (ρ, τ, I_o) must be taken into account if accurate experiments are to be performed.

3. Measurement of Individual Pulse Peak Intensity, I_o

Present optical detectors do not have sufficient frequency response to monitor the instantaneous intensity of a picosecond laser pulse. They must be used in the integrating mode. Furthermore, the large surface area of our detectors performs an integration over the spatial coordinates of our laser pulse. Expressed more concisely, the signals we record are energy ($\mathcal{E}$) signals according to the relation

$$\mathcal{E} = \int_{-\infty}^{\infty} dt \int_{0}^{\infty} 2\pi r \, dr \, I(r,t) = \pi^{3/2} I_o \rho^2 \tau \quad , \qquad (4)$$

where $I(r,t)$ is the Gaussian intensity function for our pulses as written earlier in Eq. 3 of this chapter. Yet, intensity (I_o) values, not energy values, are needed for our data evaluation. Therefore we are forced to measure ρ, τ, and $\mathcal{E}$ for each pulse in order to arrive at I_o for each pulse. The techniques

for measurement of ρ and τ were discussed in the previous sections of this chapter. It remains only to outline the relatively simple procedure used to measure the energy of each laser pulse. In almost all of our experiments, biplanar photodiodes, which have characteristics of high linearity of response, stable sensitivity over long periods of time, and large photocathode area, were used as the optical detectors. They were generally fitted with narrow-band dielectric interference filters. These detectors were always calibrated with the same procedure, using the same two thermopiles as standards. The thermopiles are products of the Eppley Laboratory (Newport, R.I.), and were calibrated in absolute units by the manufacturers using National Bureau of Standards reference light sources. Our calibration procedure involved firing the laser at a non-damaging level at 7 pulses per second into the thermopile and recording the signals from the thermopile and the photodiode. The calibration figure of the thermopile was then used to determine the photodiode absolute sensitivity. The high repetition rate was necessary for two reasons: i) the thermopile is too insensitive to respond to single pulses; ii) the thermopile is calibrated with a continuous light source, meaning that our repetition period had to be less than the instrument response time by at least a factor of 10 to enable us to use the calibration figure.

Therefore, the typical pulse intensity measurement involved

recording the pulse energy with a calibrated photodiode, and dividing it by $\pi^{3/2}\rho^2\tau$, where ρ is the essentially constant spatial radius and τ is the individual pulse duration obtained with the τA technique (Appendix II). Our procedures yielded intensity values with estimated accuracy in the unfocused case of ±20% (±10% in electric field), and ±30% (±15% in electric field) in the focused case. These uncertainty figures were substantiated by the reproducibility of standard measurements performed at different times.

F. Additional Applications of Laser System

To indicate the utility and versatility of the laser system and characterization procedures that were discussed in this chapter, in experiments other than those constituting the remaining chapters and principal theme of this thesis, papers concerning two different research areas are included here. Part A of Appendix IV contains a paper published on the subject of laser-induced photoemission from a metal surface caused by multiphoton absorption. In particular, four-photon photoemission was observed from a tungsten surface, using 1.064 μm light over an intensity range of 5×10^8 W/cm^2 to almost 10^{10} W/cm^2. The photocurrent density varied over a corresponding range of slightly more than 4 orders of magnitude. The careful control of the picosecond laser pulses permitted the elimination of lower-order thermionic heating effects, a necessity for the

observation of such a high-order nonlinear process.

In Part C of Appendix IV, we include a paper published on the different subject of two-photon absorption in semiconductors. The two-photon absorption coefficient at 1.064 μm was measured in five semiconductors. The coefficients we found were among the smallest ever reported, and were in surprisingly good agreement with theoretical extimates. The reason for the systematic smallness of our coefficient values, as compared with those from previous experiments, is again the degree of characterization and control permitted by our experimental apparatus and techniques in determining the intensity distribution of our laser pulses.

REFERENCES

1. D. von der Linde and K. F. Rodgers, IEEE J. Quant. Electr. QE-9, 960 (1973).

2. M. B. Davies, P. Sharman and J. K. Wright, IEEE J. Quant. Electr. QE-4, 424 (1968).

3. D. J. Bradley, G.H.C. New, and S. J. Caughey, Opt. Commun. 2, 41 (1970).

4. I. M. Winer, Appl. Opt. 5, 1437 (1966).

5. See discussion and extensive references in P. W. Smith, M. A. Duguay, and E. P. Ippen, in Progress in Quantum Electronics, edited by J. H. Sanders and S. Stenholm (Pergamon, Oxford, 1974), Vol. 3, Part 2, Chap. 4.

6. H. Al-Obaidi, R. J. Dewhurst, D. Jacoby, G. A. Oldershaw, and S. A. Ramsden, Opt. Commun. 14, 219 (1975).

7. P. G. Kryukov and V. S. Letokhov, IEEE J. Quant. Electr. QE-8, 766 (1972); see also W. H. Glenn, IEEE J. Quant. Electr. QE-11, 8 (1975) and references therein.

8. V. I. Tikhonov, Sov. Phys. USPEKHI 5, 594 (1963).

9. W. L. Faust and J. N. Bradford, Naval Research Laboratory, Washington, D. C., private communication.

CHAPTER III.

STUDY OF PICOSECOND LASER-INDUCED BREAKDOWN AT 1.064 μm

This chapter is composed of three parts. Part A (pages III-2 to III-10) describes the first systematic study of picosecond laser-induced breakdown, and the major results and conclusions of this chapter are presented there. Part A is a reproduction of a 1975 publication. In Part B (pages III-11 to III-12) the experimental techniques developed in Part A are used to study several new laser-related optical materials. Part B is also a reproduction of a published paper. Part C (pages III-13 to III-26) describes an additional aspect of the 1.064 μm study, the breakdown morphology, which was not included in Parts A or B. Part C is in the form of a manuscript which is to be published in Optics Communications (1976).

PHYSICAL REVIEW B VOLUME 12, NUMBER 2 15 JULY 1975

Dielectric-breakdown threshold and nonlinear-refractive-index measurements with picosecond laser pulses*

W. L. Smith, J. H. Bechtel, and N. Bloembergen
Gordon McKay Laboratory, Harvard University, Cambridge, Massachusetts 02138
(Received 18 February 1975)

Single pulses from a well-calibrated mode-locked YAG:Nd laser have been used to study the dielectric-breakdown properties of 14 transparent solids. Results are presented for the breakdown threshold electric fields, accurate to an estimated 15%. The experimental technique permits simultaneous measurement of the nonlinear susceptibility $\chi_{xxxx}^{(3)}(-\omega,\omega,\omega,-\omega)$, via the nonlinear refractive index. Susceptibility results with estimated accuracy of 50% are presented.

I. INTRODUCTION

It is well known that damage to transparent optical components in high-power laser systems constitutes a limiting factor to their performance. In many practical cases the damage threshold is set by the presence of absorbing inclusions, or by the occurrence of self-focusing. It has, however, been established that an intrinsic damage threshold, characteristic of the bulk transparent material, can be defined. If the effects of inclusions have been eliminated, and if one has corrected for the effects of self-focusing, the threshold is determined by the onset of avalanche ionization, in a manner which is very similar to low-frequency electric breakdown.[1] Since the conduction-electron density has to build up from the initial density of about 10^8 to 10^{10} electrons/cm^3 to a critical value of about 10^{18} electrons/cm^3 during the duration of the laser pulse, the damage threshold has a characteristic dependence on pulse duration. Most available experimental data were taken with pulses of nanoseconds or longer duration. In fact, heretofore, there was only one quantitative datum point taken with a picosecond pulse.[2] The reliability of that point has been questioned on the grounds that, for picosecond pulses, impurities of submicroscopic size may play a dominant role and that no morphological study of the damaged region had been made. The purpose of this paper is to provide systematic picosecond data on the damage threshold in 14 transparent materials. The data obtained are characteristic of the material and are very reproducible.

It is necessary to take into account the effects of self-focusing in this experiment, even though the maximum pulse power was always less than the critical power for self-focusing.[3,4] This power P_{cr} is related to the intensity-dependent contribution to the index of refraction n_2, where

$$n = n_0 + n_2 |E_{rms}|^2 , \tag{1}$$

by

$$P_{cr} = c\lambda^2/32\pi^2 n_2 . \tag{2}$$

In the above equations, n_0 is the linear refractive index, c is the speed of light, and λ is the vacuum wavelength. Wagner *et al.*[5] discuss the deformation of a Gaussian light pulse by the self-interaction represented by Eq. (1). Let w_1 be the beam waist, i.e., the radius at which the intensity drops to $1/e$ of its on-axis value, at low power levels. Then the low-power focal area πw_1^2 is reduced by a factor $(1 - P/P_{cr})$ due to self-action. The maximum intensity is consequently increased by a factor $(1 - P/P_{cr})^{-1}$. Zverev and Pashkov[6] and Fradin[7] have suggested how this effect may be used to determine P_{cr}, and consequently n_2, by measuring the damage threshold as a function of focal length, utilizing different lenses.

Consider a low-power diffraction-limited Gaussian pulse with an initial $1/e$ intensity radius ρ. A lens, without spherical aberration and with focal length f, will produce a focal spot with a radius (to the $1/e$ intensity point) of

$$w_1 = \lambda f/2\pi\rho . \tag{3}$$

If the pulse total power is P and we define an area $A = \pi w_1^2$, the focal plane intensity distribution is given by

$$I(r) = (P/A)\, e^{-(r/w_1)^2} . \tag{4}$$

For high-power pulses where self-focusing tendencies cannot be ignored, the relationship between the maximum intensity and the power becomes

$$I_{max} = (P/A)(1 - P/P_{cr})^{-1} \tag{5}$$

or

$$P^{-1} = I_{max}^{-1} A^{-1} + P_{cr}^{-1} . \tag{6}$$

If one plots, therefore, the reciprocal measured power, necessary to produce the value of I_{max} required for breakdown, as a function of the reciprocal focal area A^{-1}, one should obtain a straight line. The slope of this straight line gives the breakdown

rms electric field strength

$$E_b = (I_{max}/cn_0\epsilon_0)^{1/2}, \quad (7)$$

where ϵ_0 is the free-space permittivity. The intercept with the vertical axis determines P_{cr} and n_2.

One restriction implicit in the preceding discussion concerns the response time of the self-focusing mechanism. Various mechanisms for self-focusing exist,[3,8] with response times from the order of 10^{-8} sec for electrostrictive and thermal self-focusing, to the order of 10^{-15} sec for self-focusing originating in the electronic hyperpolarizability. For picosecond-pulse experiments in solids, the only mechanism fast enough to reach its steady-state value is the electronic hyperpolarizability. That mechanism follows our laser-pulse intensity essentially instantaneously, and so the assumption of a steady-state nonlinearity is a valid one for our experiment. Indeed, picosecond pulses provide results free from ambiguity introduced by slower contributions to n_2, an ambiguity which may hinder Q-switched laser-pulse experiments.

The method described above has been used to measure the rms breakdown field strength E_b and the critical power for self-focusing P_{cr} in several transparent solids of interest. Section II describes the experimental apparatus and procedure, including a technique for measuring the product of the laser-pulse duration and pulse area on a shot-to-shot basis in a simple manner. Results are presented and discussed in Sec. III.

II. EXPERIMENTAL METHOD

A. Laser system

A mode-locked YAG: Nd laser system generated the picosecond pulses used in these experiments. The experimental arrangement is illustrated in Fig. 1. A 6-mm-diam by 3-in-long Brewster-ended YAG: Nd rod supplies gain. Mode locking is achieved by a contacted dye cell which confines a 0.5-mm-thick sheet of flowing Kodak 9860 saturable absorber. TEM_{00} transverse profile is established with an intracavity aperture. Single-pulse switch-out is effected by a cylindrical-ring electrode potassium dideuterium phosphate Pockels cell, positioned between crossed polarizers, and pulsed by a nitrogen-filled high pressure laser-triggered spark gap. A selected pulse then propagates through two single-pass YAG: Nd amplifiers for augmentation of energy. A repetition rate of 20 pulses/sec is available, and an amplified single-pulse peak power exceeding 300 MW has been measured. CRO-1 is a Tektronix 519 oscilloscope used in conjunction with high-speed biplanar photodiode PD-1 (ITT F4000, S-1 response), for single-pulse monitoring. Two Glan polarizers form the variable attenuator A in Fig. 1. The calibrated photodiode PD-3 (S-1 response) measures the energy incident on the lens. The second-harmonic generation channel, ending with photodiode PD-2 (S-20 response), is used with PD-3 to obtain single-pulse values of the product of the pulse duration and pulse area, as will be described later. CRO-2 is a Tektronix 555 dual-beam oscilloscope. In Fig. 1, L represents the focusing lens and S the sample materials tested in the experiments.

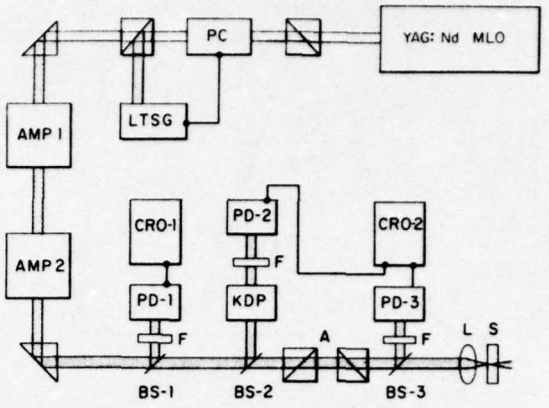

FIG. 1. Schematic diagram of the experimental arrangement. MLO, mode-locked YAG: Nd oscillator; PC, Pockels cell; LTSG, laser-triggered spark gap; AMP, YAG: Nd amplifier; BS, beam splitter; F, filter; PD, biplanar photodiode; CRO, oscilloscope; KDP, second-harmonic generation crystal; A, Double Glan-prism variable attenuator; L, focusing lens; S, dielectric sample.

Fig. III.1

B. Pulse characteristics

1. Spatial characteristics

Since precise measurement of threshold optical electric fields requires an accurate knowledge of both the spatial and temporal pulse shape and the pulse energy, great care was taken toward those measurements.

At the actual site on the optical table where the focusing lens was later placed for the breakdown measurements, three scans across the beam were made with a 50-μm pinhole to determine the transverse intensity distribution. The results of one of the scans is shown in Fig. 2. In addition, pictures were taken of phase-matched second-harmonic light with a multilens camera[9] (MLC). The result of each of the above tests was that the intensity distribution is of Gaussian form to at least the $1/e^2$ points, and that the average $1/e$ intensity radius $\langle\rho\rangle$ is 1.1 ± 0.1 mm.

2. Temporal characteristics

In order to determine the temporal pulse profile of the output, two techniques[10] were used: a second-harmonic-generation autocorrelation method

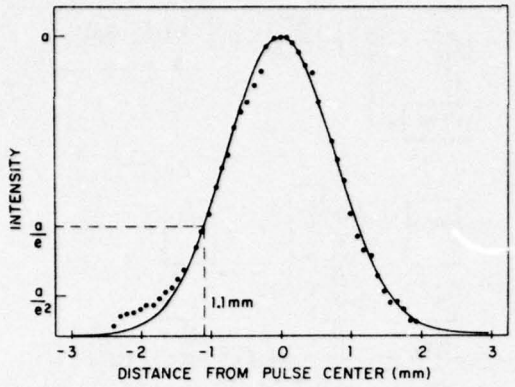

FIG. 2. Intensity distribution of laser pulse at location of focusing lens. The solid line is a Gaussian fit to the data, yielding a $1/e$ intensity radius 1.1 mm.

Fig. III.2

(SHAC), and two-photon-fluorescence (TPF) photography. The two methods are formally equivalent, both providing $1+2G_2(\tau)$. In either method, a single pulse is split into two pulses of equal amplitude (any disparity in the two amplitudes degrades the contrast ratio). In the TPF arrangement, the two pulses are then redirected by mirrors to overlap in a precisely collinear fashion within a two-quantum-absorptive material such as Rhodamine 6G, and the dye fluorescence is photographed. In the SHAC method the beam splitter is part of a Michelson interferometer. The pulses are recombined collinearly, after one has been delayed by a variable amount, and directed through a potassium dihydrogen phosphate (KDP) crystal. One plots second-harmonic output as a function of delay. The result of one of the SHAC runs is shown in Fig. 3. The enhanced scatter of the points near the center of the graph is due to interference effects in the interferometer. The curve is a four-parameter least-squares fit to the function $K_1+K_2\exp[-2(z-\frac{1}{2}z_0)^2/c^2\tau^2]$. It shows a contrast ratio [equal to $(K_1+K_2)/K_1$] of 2.7:1. The results of TPF traces, each one the result of many laser shots, agree with the data of Fig. 3: the average full-width-at-half-maximum (FWHM) temporal duration of the laser output is 30.0 ± 6.0 psec, implying an average $1/e$ half-duration $\langle\tau\rangle$ of 18.0 ± 3.6 psec.

3. *Individual-pulse τ, A measurements*

During the course of the laser calibration, a narrow distribution of individual pulse durations was actually observed, the average of which is the value stated above. In order to investigate the pulse-width statistics further, and to be able to obtain individual τ measurements, a simple pulse-duration–pulse-area monitor system was devised and added to the laser system.[11] The rationale of this monitor system follows from the proven Gaussian spatial and temporal distribution of the pulse intensity. Let $\mathcal{E}_f$ be the energy content of the sample of the fundamental pulse that is measured by photodiode PD-3 in Fig. 1, and $\mathcal{E}_{sh}$ be the energy content of the second-harmonic sample that is measured by PD-2. Then, for small harmonic conversion efficiencies, it can be shown that

$$\mathcal{E}_f^2/\mathcal{E}_{sh}=q\tau A\ , \tag{8}$$

where q is a collection of constants for a given experiment. If, in the course of an experiment, enough data points are taken so that the average of the ratio values given above is meaningful and representative, then that average value can be set equal to the product of the known, previously measured average values, $\langle\tau\rangle\langle A\rangle$, thereby calibrating absolutely the individual pulse values of the ratio given by Eq. (8). Using these individual-pulse values of τA, one obtains individual-pulse intensity values from the easily measured pulse-energy values. This simple scheme is useful in obtaining accurate data for processes which are highly nonlinear in the intensity, such as laser-induced breakdown or multiphoton photoemission.[12]

C. Focal considerations

As discussed in Sec. I, a plot of the reciprocal breakdown power versus reciprocal focal area yields the breakdown field and the nonlinear refractive index. For each material tested in these experiments, the breakdown power was measured for three different lenses. The focal lengths were 0.5, 1.0, and 1.5 in. All were of proper shape to minimize spherical aberration.[13] In the absence of all aberration, the intensity distribution in the focal plane inside the test material would be the Fourier

Fig. III.3

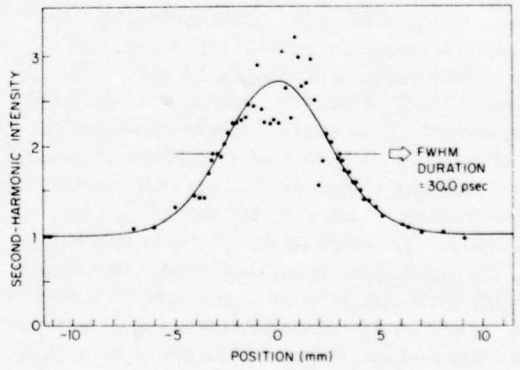

FIG. 3. Results of measurement of the laser pulse average temporal duration, using a second-harmonic-generation technique. The enhanced scatter of the points in the middle of the data is due to interference effects in the interferometer. The solid curve is a least-squares fit to the data, yielding a FWHM duration of 30.0 psec and a contrast ratio of 2.7:1.

transform of the distribution in the back focal plane of the lens. The latter is of the form $I(r) = I_0 \exp -(r/\rho)^2$, and so the focal-plane distribution would be $I_f(r) = I_0' \exp -(r/w_1)^2$, where w_1 is given in Eq. (3). Such performance would be diffraction limited. In reality, however, contributions to the focal radius due to spherical aberration by the lens and by the planar surface of the test material must be considered. The radius that would result from the first of these two aberrations w_2 is given by[13]

$$w_2 = 4\kappa\rho^3/f^2 , \tag{9}$$

where κ is a function of lens refractive index and has the value 0.069 for the 0.5- and 1.5-in. focal-length lenses (quartz, $n_0 = 1.4498$), and 0.0455 for the 1-in. focal-length lens (glass, $n_0 = 1.6667$), at 1.06 μm. Equation (9) was derived for the case of a plane wave incident on the lens, but it is still useful here in a manner to be described below. The focal radius that would result from spherical aberration by the planar test material surface[14] w_3 is given by

$$w_3 = D(n_0^2 - 1)\rho^3/2n_0^3 f^3 , \tag{10}$$

where D is the distance between the interface and the focal point and, in the experiments here, was always 2.0 mm. The effective focal radius w is related to the above constituents by

$$w = (w_1^2 + w_2^2 + w_3^2)^{1/2} . \tag{11}$$

In Table I, the quantities introduced above are tabulated for the three lenses used here. Because of the shallow depth of focus D maintained here, the contribution to w from w_3 is seen to be less than 1% in all cases. The contribution from w_2 is also seen to be less than 1% for the $f = 1$-in. and $f = 1.5$-in. lenses. Thus, in these two cases, the use of Eq. (9) to compute w_2 is acceptable. For the $f = 0.5$-in. lens, however, the spherical aberration contribution to w as calculated from Eq. (9) is nonnegligible. It was felt necessary to perform an experiment to determine the focal distribution for this lens. To that end a chromium-steel razor blade was mounted on a two-dimensional precision translator with 0.13-μm resolution. The front surface of the blade edge was then positioned precisely in the focal plane of the 0.5-in. focal-length lens, the focal plane being identified as that requiring the least irradiance to produce a spark on the blade surface. The blade was then swept in increments across the beam, and the fraction of the incident pulse energy (as measured by a reference detector) that was not blocked by the blade was measured as a function of position. Several shots were taken at each position, and the irradiance was always maintained below the blade damage level. A simple calculation shows that the transmission function $T(x)$ should be of the form

$$T(x) = (\pi w^2)^{-1} \int_{-\infty}^{x} \int_{-\infty}^{\infty} e^{-(x'^2+y^2)/w^2}\, dx'\, dy$$

$$= \tfrac{1}{2}[1 + \mathrm{erf}(x/w)] . \tag{12}$$

The experimental data conformed well to a curve of the above form if w was given the value 3.3 μm. Microscopic examination of the blade edge after the experiment verified that it had not been disfigured. Therefore, the value of 3.3 μm for the focal radius for the $f = 0.5$-in. lens was used in all data analysis in this report, and it appears in Table I.

Finally, aberration due to decentration and tilt[15] of the lens must be considered. In these experiments, such further contributions to w were rendered negligible by the following alignment procedure, which was used for every experiment. Firstly, in order to deal with tilt, the lenses were mounted in holders which allowed the attachment of a microscope slide in front of the lens in such a manner as to be parallel to the plane of the lens. Next the beam was apertured so as to allow only a small (0.5-mm-diam) central section to strike the attached slide. The lens was then adjusted to be normal to the propagation direction to within better than 1.0° by adjusting the holder so that the reflection was collinear with the pulse propagation direction. Secondly, decentration was made negligible by two operations. Before the lens was placed in the system, the position of the center of the laser pulse at a point past the lens site was located by a marked phosphorescent card. Then with the lens inserted, and corrected for tilt as discussed above, it was translated so that the center of the transmitted light was coincident with the position previously located. Additionally, the reflection of the pulse from the curved, first face of the lens was observed with another viewing card and when alignment was obtained, the reflection was symmetrically distributed about the propagation direction. The lenses could be centered to within 0.1 mm easily, making associated aberration negligible. The reproducibility of lens positioning afforded by the above simple techniques is necessary for accurate absolute breakdown field measurements over a large series of materials.

Table III.1

TABLE I. Focal parameters.

Focal length f (in.)	w_1 (μm)	w_2 (μm)	w_3 (μm)	w (μm)	$A = \pi w^2$ (μm^2)
0.5	1.95	a	0.23	3.3[a]	34.2
1.0	3.80	0.37	0.03	3.94	48.2
1.5	5.85	0.25	0.01	5.85	107.9

[a]See text, Sec. II C.

D. Procedure

To begin each experiment, the sample was optically polished and blown with dry nitrogen to remove any residual abrasive particles from the surface. The sample was then clamped onto an x-y translator, and the entrance surface was aligned normal to the propagation direction. It was necessary to maintain a hot-air stream over the most hygroscopic of the materials to retain surface quality. The amplifier gain and the variable attenuator were then adjusted so that the approximate breakdown irradiance entered the material and so that sufficient signal was available for the τA measurement devices, as discussed earlier. Thereafter, the attenuator was left unchanged in order that the ratio values of Eq. (8) retain their usefulness, as noted earlier. Any further fine adjustment of the input irradiance was done with the amplifier gain control. The material was translated between pulses so that a new portion of the material was probed by each pulse, and the coordinates of each probed location were recorded. A fast photodiode/Tektronix 519 oscilloscope combination (PD-1/CRO-1 in Fig. 1) was monitored during each firing in order to eliminate data from pulses with satellites. At each firing, the fundamental energy and the harmonic energy were recorded. Loss of energy by reflection from the lens and material surface was taken into account in each experiment. The fundamental energy was measured with a photodiode calibrated with an Eppley Laboratory thermopile. Breakdown sparks were initially detected with well dark-adapted eyes operating in a dark room shielded from laser flashlamp light. Later, using the recorded coordinates of the probed sites, the crystal was observed under a microscope to verify breakdown at any visually uncertain points. The observed damage was confined to a cylindrically shaped volume typically 2 μm in diameter and 25–50 μm in length, and therefore occupied a small fraction of the focal volume, just above threshold. The reproducibility of the data when probing different specimens and different volume elements within the same specimen indicate that a property characteristic of the bulk material is observed. Only a few isolated cases of inclusions were observed under the microscope, and they were eliminated. A further detailed account of the morphology of the damage will be given elsewhere. Typically, 50 shots were used near the threshold region with each lens for each material. The data were then plotted as shown in Fig. 4 for KCl. The sharpness of the threshold is typical of the behavior encountered in these experiments. The uncertainty in the breakdown energy was generally less than 10%. The three encircled points were associated with pulses having unusually short τA values, and did cause breakdown even though their energy was below the threshold energy evident in the figure for pulses with τA nearer to $\langle\tau\rangle\langle A\rangle$. The damage energy was determined in this manner in each case, and then $\langle\tau\rangle$ was used to convert the energy to power. A pulse energy $\mathcal{E}_f$ is related to the pulse power P by $P = \mathcal{E}_f/(\pi)^{1/2}\tau$. The reciprocal damage-power values were then plotted versus reciprocal focal area as discussed in Sec. I. An example, that of KCl, is shown in Fig. 5. A least-squares fit to the three points then yields the desired quantities—the breakdown field E_b, independent of self-focusing effects, and the nonlinear index of refraction n_2, via the critical power for self-focusing.

III. RESULTS

In this section results are presented from tests on 14 materials. All samples were obtained from

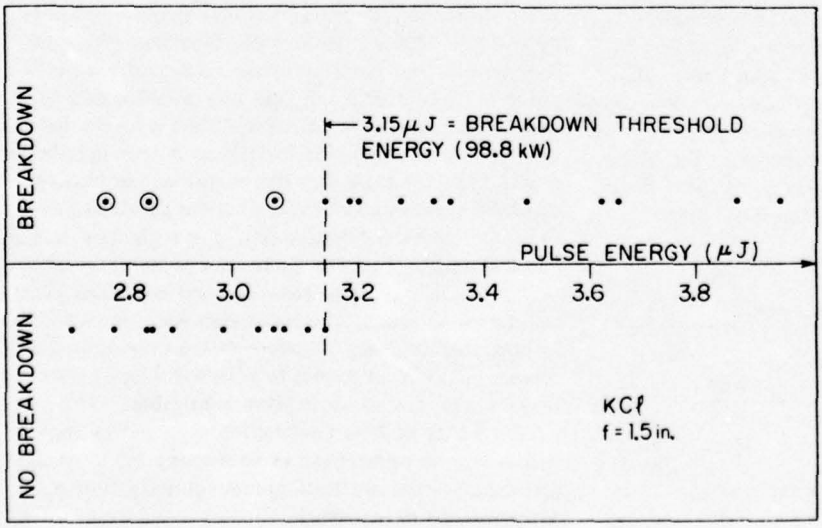

Fig. III.4

FIG. 4. Results of breakdown experiment in KCl for $f = 1.5$-in. lens. The average pulse duration $\langle\tau\rangle$ was used to convert energy to power via $P = \mathcal{E}/(\pi)^{1/2}\langle\tau\rangle$, as discussed in Sec. II D. The three circled points resulted from atypically short pulses.

commercial sources, and all except SiO_2 and ED-4, were monocrystalline. All results are for a geometry with the propagation direction along the [001] axis and electric vector along the [100] axis, except for the YAG: Nd material, in which the propagation direction was along a [111] axis. This sample orientation was chosen in order to measure the same quantities that are operational in YAG: Nd laser rods.

A. Pulse-duration dependence of the breakdown threshold in NaCl

Graphs such as Fig. 5 yield the breakdown-threshold electric field according to Eq. (6), as discussed previously. Field values so obtained are independent of all self-focusing effects. The field values obtained by us are all absolute, and the experimental uncertainty, estimated by reproducibility and by calculation, is ±15%.

In this section we examine the pulse-duration dependence of the breakdown threshold in alkali halides probed by pulses of 1.06-μm radiation only. Measurements have been made in NaCl for four different pulse durations, from 10 nsec to 15 psec, by previous investigators.[2] Those data are reproduced in Fig. 6, along with the datum point for 30 psec measured by us. The solid curve in that figure is the result of an approximate theoretical calculation discussed in Ref. 2. The previous investigators described the pulse duration dependence of the

Fig. III.5

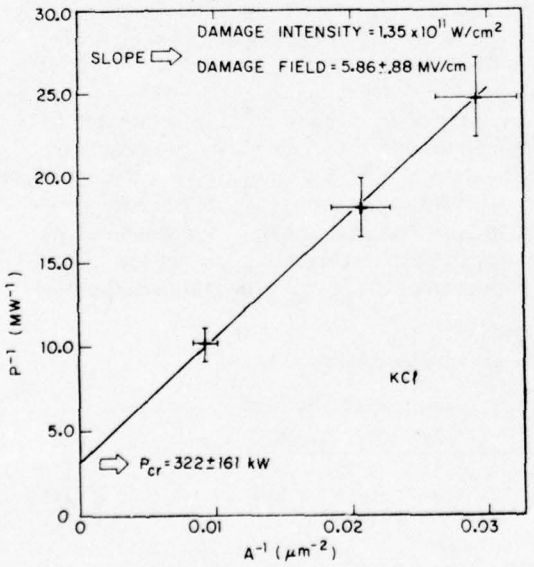

FIG. 5. Results of breakdown experiments in KCl for three lenses. The solid line is a least-squares fit to the data. The slope equals the reciprocal threshold breakdown intensity and the vertical-axis intercept equals the reciprocal critical power for self-focusing.

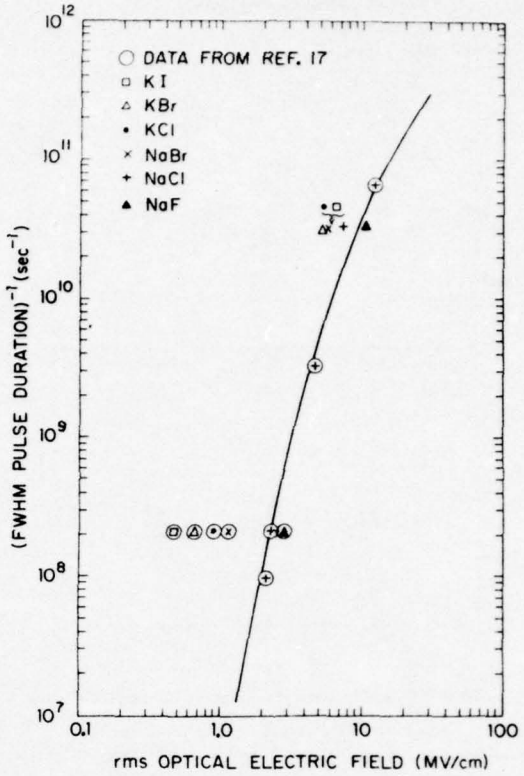

FIG. 6. Functional relationship between the breakdown threshold electric field strength and the pulse duration. The solid curve is a semiempirical prediction for NaCl, discussed in Ref. 2.

Fig. III.6

threshold in terms of a field-dependent ionization rate $\alpha(E)$, inversely proportional to the pulse width. An exponential relation between the number of conduction electrons and time was obtained

$$N(t) = N_0 \exp\left(\int_{-\infty}^{t} \alpha[E(t')]\, dt'\right) \equiv N_0 M(t) , \qquad (13)$$

where $M(t)$ describes the evolution of the initial number N_0 (~10^8 to 10^{10} per cm^3). As mentioned earlier, because $M(t)$ must reach ~10^{10} during the presence of the laser pulse, stronger fields are necessary as the pulse duration is decreased. Therefore the field dependence of the ionization rate, as well as the pulse duration dependence of the threshold, is displayed in Fig. 6.

In addition to data for NaCl, the data now available at 1.06 μm for five other alkali halides are illustrated in Fig. 6. The three Na halides display a similar relative dependence of threshold on pulse duration, which appears to be somewhat different for the K halides. In combination with dc measurements by others,[16] the data of Fig. 6 make available the approximate field dependence of the ionization rate in six materials.

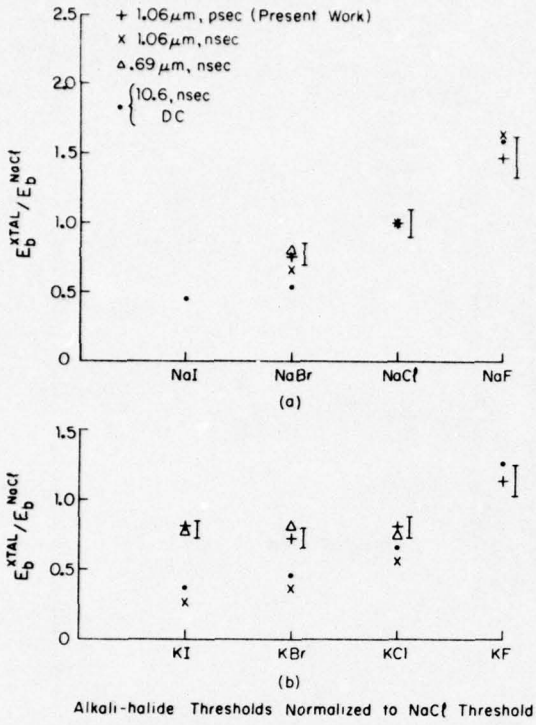

FIG. 7. Experimental trend of the breakdown field through (a) the Na halides and (b) the K halides. Shown for comparison are data from previous studies: (×), Ref. 19; (Δ), Ref. 18; (•), dc data from Ref. 16, 10.6-μm data from Ref. 17. In the figure nsec denotes a pulse duration the order of nanoseconds, and psec, picoseconds. Each set of data is normalized to the field for NaCl of that same data set. Error bars for the present work are shown displaced to the right.

Fig. III.7

B. Variation of the breakdown-threshold field through the Periodic Table

We now consider the variation of the breakdown threshold among different substances for picosecond pulses at 1.06-μm wavelength. The results of our measurements are presented in Table II. The threshold is observed to vary from a minimum of 3.4 MV/cm to a maximum of 22.28 MV/cm among the materials tested. KDP possesses a threshold so high as to approach the level necessary to make multiphoton ionization probable. Figure 7 displays the trend of our threshold measurements across the Periodic Table for the Na and K halides. For comparison, previous data from dc,[16] and Q-switched CO_2,[17] ruby,[18] and YAG: Nd,[19] laser-damage studies are presented. Note that all the data for a particular combination of pulse duration and frequency are normalized to the NaCl threshold of that same data set.

C. Third-order electronic susceptibility

The critical power for self-focusing, as given by Eqs. (2) and (6), is obtained in these experiments as the inverse of the intercept of the fitted line with the vertical axis, in graphs such as Fig. 5. The nonlinear index n_2 and $\chi^{(3)}(-\omega, \omega, \omega, -\omega)$ are related by

$$n_2 = 12\pi\chi^{(3)}(-\omega, \omega, \omega, -\omega)/n_0 \,. \qquad (14)$$

The experimental condition that the laser-pulse duration is much shorter than the electrostrictive response time ($\sim 10^{-9}$ sec) and that the materials investigated are ionic solids, indicate that the values of P_{cr}, n_2, and $\chi^{(3)}$ obtained in these experiments are those of electronic (E) origin only. Several techniques have previously been employed to measure $\chi^{(3)E}$, among them third-harmonic generation,[20,21] three-wave mixing,[22,23] intensity-dependent ellipse rotation,[24] nonlinear birefringence,[25] and time-resolved interferometry.[26]

The values obtained in the present experiments for the critical power P_{cr}, the nonlinear refractive index, and the third-order electronic susceptibility $\chi^{(3)E}_{xxxx}(-\omega, \omega, \omega, -\omega)$ are presented in Sec. A of Table III. Also tabulated is the linear refractive index used to convert n_2 into $\chi^{(3)E}$. The experimental accuracy of P_{cr}, and of $\chi^{(3)E}$, is estimated to be ±50%. Section B of the table lists previously obtained values of $\chi^{(3)E}$ for comparison. The smallest $\chi^{(3)E}$ value was registered by NaF, a factor of almost 18 less than that of KBr. Agreement with previous values is substantial, except for LiF, given the rather large experimental uncertainties

Table III.2

TABLE II. rms breaksown electric field strengths (E_b uncertainty, ±15%; field ratio uncertainty, ±10%).

	NaF	NaCl	NaBr	KF	KCl	KBr	KI
E_b (MV/cm)	10.77	7.34	5.67	8.34	5.86	5.33	5.87
E_b/E_b^{NaCl}	1.47	1.00	0.77	1.14	0.80	0.73	0.80

	LiF	RbI	ED-4[a] glass	YaG:Nd	Fused SiO_2	CaF_2	KDP
E_b (MV/cm)	12.24	3.40	9.90	9.82	11.68	14.44	22.28
E_b/E_b^{NaCl}	1.67	0.46	1.35	1.34	1.59	1.97	3.04

[a]Owens-Illinois (Toledo, Ohio) undoped laser glass.

TABLE III. Results for $\chi^{(3)E}_{1111}(-\omega,\omega,\omega,-\omega)$.

	A. Present work				B. $\chi^{(3)E}_{1111}$ (10^{-14} esu), other work					
					Experiment[a]				Theory[b]	
Material	P_{cr} (MW)	n_0	n_2 (10^{-14} esu)	$\chi^{(3)E}_{1111}$ (10^{-14} esu) ±50%	I ±300%	II ±20%	III	Other	I	II
NaBr	0.111	1.62	96.15	4.13						
NaCl	0.166	1.532	64.66	2.63	1.2	1.7			0.8	2.0
NaF	1.13	1.321	9.45	0.33	0.25				0.13	0.3
KI	0.095	1.638	112.35	4.88					3.1	9.0
KBr	0.075	1.544	142.31	5.83	2.8	3.0			1.3	3.7
KCl	0.322	1.479	33.15	1.30	1.2	1.9			0.9	1.9
LiF	0.438	1.387	24.37	0.90	0.3	0.2	0.34 ± 0.06		0.28	0.3
CaF_2	0.389	1.429	27.70	1.05		0.35	0.43 ± 0.13		0.4	0.4
fused SiO_2	0.783	1.450	13.63	0.52		0.7	0.70 ± 0.12	0.38 ± 0.03^{IV}	1.4	1.1
KDP	0.295	1.494	36.18	1.43						
ED-4	0.503	1.550	21.22	0.87			1.07 ± 0.08	0.71 ± 0.05^{IV}		
YAG : Nd[c]	0.302	1.823	35.34	1.71			2.18 ± 0.13	1.98 ± 0.14^{IV} 1.53 ± 0.30^{V}		0.62

[a] I. Values from third-harmonic generation, Wang and Bardeen, Ref. 20. II. Values from three-wave mixing, Maker and Terhune, Ref. 22. III. Values from three-wave mixing, Levenson and Bloembergen, Ref. 23. IV. Values from intensity-dependent ellipse rotation, Owyoung, Ref. 24. V. Values from time-resolved interferometry, Bliss *et al.*, Ref. 26.

[b] I. Calculated from generalized Miller's, $\chi^{(3)} = (\chi^{(1)})^4 \times 10^{-10}$ esu, Wang, Ref. 27. II. Calculated from Wang's rule, Ref. 27.

[c] All experimental values in this row, with one exception, are for pulse propagation along a [111] direction, the usual laser rod configuration. In these cases, the measured susceptibility is $\frac{1}{2}(\chi^{(3)E}_{1111} + \chi^{(3)E}_{1221} + 2\chi^{(3)E}_{1122})$. The value in the column designated III is for the single element $\chi^{(3)E}_{1111}$, however. The present work investigated a YAG : Nd crystal; all other values in the row pertain to undoped YAG crystal.

Table III.3

listed. The only serious discrepancy occurs for LiF. The difference between our value for LiF and those obtained by others is a factor of approximately 3. We tested two different samples of LiF, a total of three times, and our results were reproducible. Therefore, we know of no reason to suspect that the error in our value for LiF exceeds the stated uncertainty of ±50%. The expected trend of the third-order susceptibility element through the periodic table is displayed for the Na and K halides.

IV. SUMMARY

The method of controlled dielectric breakdown[6,7] has been demonstrated to be a useful way to measure simultaneously the two intrinsic parameters which must be known to enable propagation of maximum picosecond-light intensity through a material in a stable nondestructive manner. Those parameters, the breakdown field strength and the electronic nonlinear refractive index, have been measured in several materials of scientific interest with 1.06-μm laser pulses of 30-psec average duration (FWHM). The measurements were made with well-calibrated pulses and focal geometry, in a manner allowing elimination of any inclusion effect and measurement of intrinsic processes characteristic of the bulk. A simple technique was related for the measurement of (individual picosecond pulse duration)-(pulse area) products. The values of $\chi^{(3)E}(-\omega,\omega,\omega,-\omega)$ presented here are in reasonable agreement with those of other investigators. The measured breakdown field strengths have been shown to be those of an avalanche ionization process. Further picosecond experiments at the second-harmonic frequency are in progress to investigate the onset and properties of dielectric breakdown driven by multiphoton ionization.

ACKNOWLEDGMENTS

The authors are grateful to Patrick Heck of Owens-Illinois, Inc., for supplying a sample of ED-4 glass, and to S. Maurici for his skillful preparation of the many samples. One of us (W. L. S.) is also appreciative of helpful discussions with Professor Eli Yablonovitch of Harvard.

*Research supported in part by the National Aeronautics and Space Administration, by the Joint Services Electronics Program and by the Advanced Research Projects Agency.

[1] N. Bloembergen, IEEE J. Quantum Electron. QE-10, 375 (1974).

[2] D. W. Fradin, N. Bloembergen, and J. P. Lettelier, Appl. Phys. Lett. 22, 635 (1973).

[3]S. A. Akhmonov, R. V. Khokhlov, and A. P. Sukhorukov, in *Laser Handbook*, edited by F. T. Arecchi and E. O. Schulz-DuBois (North-Holland, Amsterdam, 1972), Vol. 2, Chap. E3.

[4]J. H. Marburger (unpublished).

[5]W. G. Wagner, H. A. Haus, and J. H. Marburger, Phys. Rev. 175, 256 (1968).

[6]G. M. Zverev and V. A. Pashkov, Zh. Eksp. Teor. Fiz. 57, 1128 (1969) [Sov. Phys.-JETP 30, 616 (1970)].

[7]D. W. Fradin, IEEE J. Quantum Electron. QE-9, 954 (1973). Note that Eq. (2) in this reference should read $I_d = I_0(1 - P/P_{cr})^{-1}$.

[8]A. Feldman, D. Horowitz, and R. M. Waxler, IEEE J. Quantum Electron. QE-9, 1054 (1973).

[9]I. M. Winer, Appl. Opt. 5, 1437 (1966).

[10]P. W. Smith, M. A. Duguay, and E. P. Ippen, in *Progress in Quantum Electronics*, edited by J. H. Sanders and S. Stenholm (Pergamon, Oxford, 1974), Vol. 3, Pt. 2, Chap. 4.

[11]W. L. Smith and J. H. Bechtel (unpublished). The proportionality expressed by Eq. (8) was noted by W. H. Glenn and M. J. Brienza [Appl. Phys. Lett. 10, 221 (1967)], and used by C. V. Shank and E. P. Ippen [Appl. Phys. Lett. 24, 373 (1974)], in conjunction with a cw mode-locked dye laser.

[12]J. H. Bechtel, W. L. Smith, and N. Bloembergen, Opt. Commun. 13, 56 (1975).

[13]W. J. Smith, *Modern Optical Engineering* (McGraw-Hill, New York, 1966), Chap. 3. The lenses used in these experiments were either standard or custom products of Special Optics, Little Falls, N. J. 07424.

[14]E. Yablonovitch, thesis (Harvard University, 1972) (unpublished).

[15]P. L. Ruben, J. Opt. Soc. Am. 54, 45 (1964).

[16]A. von Hippel, J. Appl. Phys. 8, 815 (1937).

[17]E. Yablonovitch, Appl. Phys. Lett. 19, 495 (1971).

[18]D. W. Fradin and M. Bass, Appl. Phys. Lett. 22, 206 (1973).

[19]D. W. Fradin, E. Yablonovitch, and M. Bass, Appl. Opt. 12, 700 (1973).

[20]C. C. Wang and E. L. Bardsen, Phys. Rev. 185, 1079 (1969); and Phys. Rev. B 1, 2827 (1970).

[21]W. K. Burns and N. Bloembergen, Phys. Rev. B 4, 3437 (1971).

[22]P. D. Maker and R. W. Terhune, Phys. Rev. 137, A801 (1965).

[23]M. D. Levenson, IEEE J. Quantum. Electron QE-10, 110 (1974); and M. D. Levenson and N. Bloembergen, Phys. Rev. B 10, 4447 (1974).

[24]A. Owyoung, IEEE J. Quantum Electron. QE-9, 1064 (1973).

[25]M. A. Duguay and J. W. Hansen, in *Damage in Laser Materials*, Natl. Bur. Stds. Spec. Publ. No. 341 (U.S. GPO, Washington, D.C., 1970), p. 45.

[26]E. S. Bliss, D. R. Speck, and W. W. Simmons, Appl. Phys. Lett. 25, 728 (1974).

[27]C. C. Wang, Phys. Rev. B 2, 2045 (1970).

Laser-induced breakdown and nonlinear refractive index measurements in phosphate glasses, lanthanum beryllate, and Al_2O_3†

W. Lee Smith and J. H. Bechtel

Gordon McKay Laboratory, Harvard University, Cambridge, Massachusetts 02138
(Received 2 February 1976)

We present results of measurements of the laser-induced dielectric breakdown threshold in two phosphate composition laser glasses, in lanthanum beryllate:Nd, and in Al_2O_3. The nonlinear refractive indices for these materials are also presented. The measurements were made with single 30-psec 1.064-μm pulses. The results are compared with those for other laser materials in the 1.06-μm spectral region.

PACS numbers: 79.20.Ds, 77.50.+p, 78.20.Dj, 42.65.−k

The properties of two recently introduced laser materials which operate near 1.06 μm have attracted considerable interest. The prospect of a smaller nonlinear refractive index but larger gain coefficient than offered by familiar silicate glasses has created interest in new phosphate composition glasses.[1] Another new laser material, neodymium-doped lanthanum beryllate[2] ($La_2Be_2O_5$: Nd) is of interest due to its biaxial monoclinic (C_2h) structure which results in plane-polarized output radiation. We report here measurements of the threshold electric field for laser-induced damage and the nonlinear refractive index in these two new materials, and also in a carefully grown sample of Al_2O_3. These new results will be compared to measurements from a similar study at 1.064 μm,[3] which included YAG : Nd and ED-4 laser glass.

The experimental technique and apparatus used in this experiment have been described previously,[3] and will only be outlined here. A saturable absorber (Kodak 9860) mode-locked YAG : Nd oscillator, constrained to the TEM_{00} mode, produced the picosecond, 1.064-μm laser pulses. A fast Pockels cell/spark gap combination excised one single pulse from the oscillator pulse train, and it was amplified as needed by two single-pass YAG : Nd amplifiers. Subsequent detectors monitored the energy content and the temporal duration,[3] and identified pulses with satellites or bad switch-out structure. The pulses of this laser were determined previously to be of 30-psec average duration. Three precision lenses of the proper shape to minimize spherical aberration, with focal lengths of 1.0, 1.5, and 3.0 in., were used with each material. The calculated focal area A (defined as the area in the focal plane within which the intensity exceeds e^{-1} times the peak axial value) for the three lenses in this experiment was 31.0, 50.8, and 180.5 μm^2. These values include the small effects of spherical aberration by the lens and the planar sample surface as discussed in Ref. 3.

The experimental procedure involved the passing of focused increasingly powerful pulses each through a new recorded position in the sample and noting the threshold power level P at and beyond which breakdown occurred. Breakdown was detected *in situ* by observation of microscopic spark radiation with well dark-adapted shielded eyes. Subsequently, these sightings were checked by 340-power microscopic examination, at which time any inclusion effects would have been spotted. A threshold power for breakdown was thus determined for each of the three lenses. The desired quantities, the threshold (rms) electric field for breakdown, E_b, and the critical power for self-focusing, P_{cr}, were extracted using the operative equation[3] $I_{max} = P[A(1 - PP_{cr}^{-1})]^{-1}$, where I_{max} is the peak intensity reached at the focal point. This equation describes the mild reduction of the pulse area due to self-focusing and assumes that the pulse Gaussian spatial profile itself does not become distorted. It may be rewritten into a more useful form as

$$P^{-1} = I_{max}^{-1} A^{-1} + P_{cr}^{-1}. \tag{1}$$

This equation is valid if only minor self-focusing occurs, that is, for pulse input power less than a critical power P_{cr} which is defined as

$$P_{cr} = c\lambda^2/32\pi^2 n_2. \tag{2}$$

Here n_2 is the nonlinear refractive index, λ is the optical wavelength, and c is the vacuum speed of light. Noting the linear form of Eq. (1), the reciprocals of the three threshold input power levels are plotted versus their respective reciprocal focal area. A linear least-squares fit to the three data points then yields the experimental values of I_{max} and P_{cr}. E_b and n_2 are immediately obtainable using Eq. (2) and the relation $E_b = (I_{max}/n_0 \epsilon_0 c)$, where n_0 is the linear refractive index and ϵ_0 is the free-space permittivity. The real part of the electronic third-order nonlinear optical susceptibility, $\chi^{(3)}(-\omega, \omega, \omega, -\omega)$, which is associated with n_2 in this experiment may be obtained via the relation

$$n_2 = (12\pi/n_0)\chi_{1111}^{(3)}(-\omega, \omega, \omega, -\omega), \tag{3}$$

where the frequency degeneracy factor of 3 has been included in the factor 12.

Table III.4

TABLE I. Breakdown (rms) electric field strengths (E_b uncertainty, ± 15%; field ratio uncertainty, ± 10%).

Material	E_b (MV/cm)
BEL : Nd	15.6
LHG-5 : Nd	13.0
LHG-6 : Nd	13.0
Al_2O_3	12.9
ED-4 [a]	9.9
YAG : Nd [a]	9.8

[a] Data from Ref. 3.

TABLE II. Measured nonlinear refractive indices (n_2 uncertainty, ± 50%).

Material	n_2 (10^{-13} esu)
Al_2O_3	1.30
LHG-5:Nd	1.50
LHG-6:Nd	1.50
BEL:Nd	2.12
ED-4[a]	2.12
YAG:Nd[a]	3.53

[a]Data from Ref. 3.

Table III.5

The results for the breakdown rms electric field thresholds are presented in Table I. These values are independent of self-focusing effects, in that Eq. (1) corrects analytically for the present mild self-focusing, as just discussed. The breakdown threshold was sharp ($\lesssim 10\%$ uncertainty in input power) for all the tested materials; inclusion effects were not observed. In this experiment the materials KCl and silica, examined in Ref. 3, were retested to check the accuracy of the new focal parameters. For both materials, the threshold values and critical power values agreed to better than 10% with those obtained earlier. Therefore, one may compare the absolute values obtained in the present experiment with these for the various materials tested in Ref. 3. The tested phosphate composition glasses were types LHG-5 and LHG-6 of Hoya Optics, Inc.[4] The Al_2O_3 sample was a carefully grown sample from Union Carbide Corp.[5] All the materials listed in Table I except Al_2O_3 are candidate materials for high-power near-1.06-μm laser oscillators and/or amplifiers. The laser transition in $La_2Be_2O_5$:Nd (BEL:Nd) is at 1.070 or 1.079 μm, depending on orientation,[2] while in LHG-5 and LHG-6, the laser center wavelength is at 1.056 μm. The breakdown threshold values for the new materials show considerable improvement over those of the two more commonplace 1.06-μm materials, YAG:Nd and ED-4 glass. The E_b value of 15.6 MV/cm registered by BEL:Nd is 59% greater than that of YAG:Nd, which represents an improvement factor of about 2.5 in intensity. The phosphate composition glasses also show a marked improvement in damage threshold.

Next we present the results for the nonlinear refractive indices. Table II presents the values obtained in the present experiment and also lists the values for ED-4 laser glass and YAG:Nd measured by the identical technique in Ref. 3. The experimental uncertainty in these values is unfortunately inherently rather large, ± 50%, due to the employed slope-intercept method. The orientation of our Al_2O_3 sample was such that the laser pulse propagated along the rhombohedral axis of the crystal. The electric field direction within the normal plane was not determined. The orientation of the BEL:Nd sample was not determined; however, we expect the orientational dispersion in n_2 not to exceed 20%. We now compare these measured values with those available from other methods. Recently, a value of $1.48 \pm 0.15 \times 10^{-13}$ esu for n_2 in ruby was obtained by a time-resolved interferometry technique.[6] This compares well with our value of 1.30×10^{-13} esu. The two phosphate glasses gave identical results, 1.50×10^{-13} esu, in our measurements, whereas measurements at Lawrence Livermore Laboratory[7] have produced values of 1.16 ± 0.12 and $1.01 \pm 0.10 \times 10^{-13}$ esu for LHG-5 and LHG-6, respectively. The small nonlinear indices of these new materials have important implications with regard to the propagation and focusing behavior of terawatt laser pulses.[1] The n_2 value of the other new sample, BEL:Nd, along with its relatively large damage threshold (Table I) and output polarization characteristics, indicate interesting possibilities for new laser oscillators. For completeness we note that, while our results gave the same value of n_2 for BEL:Nd and ED-4, other techniques offering better accuracy have found values for ED-4, or its Nd-doped version ED-2, of 1.52 ± 0.3,[8] 1.73 ± 0.1,[9] and 1.53 ± 0.15,[6] in units of 10^{-13} esu. For final comparison, other published values for undoped YAG in units of 10^{-13} esu are 3.16 ± 0.6,[8] 4.09 ± 0.3,[9] and 3.47 ± 0.35.[6]

The authors are grateful to M.A. Gilleo and C. Kass of Allied Chemical Corp. and D.K. Segawa of Hoya Optics U.S.A., for supplying samples. They also appreciate the collaboration of C. F. Cline, M.J. Weber, and D. Milam of Lawrence Livermore Laboratory, and thank Professor N. Bloembergen of Harvard for support and critical review of the work.

†Research supported in part by the National Aeronautics and Space Administration, by the Joint Services Electronics Program, and by the Advanced Research Projects Agency.

[1]Laser Focus 11 (No. 5), 67 (1975); 11 (No. 6), 44 (1975); 11 (No. 10), 40 (1975).
[2]R.C. Morris, C.F. Cline, R.F. Begley, M. Dutoit, P.J. Harget, H.P. Jenssen, T.S. LaFrance, and R. Webb, Appl. Phys. Lett. 27, 444 (1975); sample supplied by Allied Chemical Corp., Morristown, N.J. 07960.
[3]W. Lee Smith, J.H. Bechtel, and N. Bloembergen, Phys. Rev. B 12, 706 (1975).
[4]Hoya Optics USA, Inc. Menlo Park, CA 94025.
[5]Union Carbide Corp., East Chicago, IN 46312.
[6]M.J. Moran, C.-Y. She, and R.L. Carman, IEEE J. Quantum Electron. QE-11, 259 (1975).
[7]D. Milam and M.J. Weber (unpublished).
[8]E.S. Bliss, D.R. Speck, and W.W. Simmons, Appl. Phys. Lett. 25, 728 (1974).
[9]A. Owyoung, IEEE J. Quantum Electron, QE-9, 1064 (1973).

PICOSECOND LASER-INDUCED DAMAGE MORPHOLOGY: SPATIALLY RESOLVED MICROSCOPIC PLASMA SITES*

W. Lee Smith, J. H. Bechtel and N. Bloembergen

Gordon McKay Laboratory
Harvard University
Cambridge, Massachusetts 02138, U.S.A.

The morphology just above threshold of damage sites caused by picosecond 1.06 μm laser pulses is shown to consist of a collection of micron-sized, spatially distinct vestiges of individual plasmas. From the observed site density, the density of electrons which may initiate breakdown can be inferred. The morphology is consistent with an avalanche ionization model, but not with absorbing inclusion damage.

New observations are presented here concerning the initiation and growth of regions of avalanche plasma inside initially transparent, solid dielectrics due to the passage of intense picosecond laser pulses. These observations provide experimental data for the first time on the question of the operative density of electrons which may serve to initiate laser-induced breakdown at a given intensity level. Because of the short duration of the laser excitation used in this experiment, avalanche growth does not develop to the point of plasma microsite overlap and extensive disruption of the material. The damage morphology in the picosecond regime, induced by well controlled pulses just above the breakdown threshold, is shown to consist of a chain of individual, spatially-resolved, micron-sized plasma vestiges. They are limited to a narrow axial part of the focal region, the perimeter of which is well correlated with an avalanche ionization model.

Previously we have reported thresholds for picosecond laser-induced breakdown in eighteen transparent materials.[1, 2] The present observations concern the morphology of the damage produced in those studies. Single, 1.06 μm pulses from a passively mode-locked, TEM_{00}, YAlG:Nd laser system were used to cause breakdown. The average full-width-at-half-maximum (FWHM) pulse duration was 30 psec and a nonlinear optic technique was used to infer the duration of each individual pulse.[3] The pulse duration is known to fluctuate in passively mode-locked lasers.[4] This technique allows accurate single pulse intensity measurements. The influence of incipient self-focusing was minimized by tightly focusing the laser pulses with an external lens and by always using incident pulse power less than the critical power for self-focusing. Corrections for incipient

self-focusing were taken into account by a technique[1] using several lenses of different focal area. Any damage track, which showed presence of inclusions upon subsequent microscopic examination, was eliminated. This occurred in roughly one percent of the shots.

In figs. 1a, b, c we show photomicrographic data for picosecond laser-induced breakdown near threshold in a NaCl single crystal sample from Harshaw Chemical Co. These damage tracks were produced with a well-corrected 0.5 in. focal length lens, resulting in an intensity 1/e radius of 3.3 μm.[1] Only one pulse traversed any single region in the crystal. The tracks were photographed with a Leitz Ortholux microscope and blue light through a 0.4 N.A. objective at 340x total magnification. The calculated resolution and the observed minimum detectable diameter is ~0.7 μm. The scale lines in the figure indicate a distance of 10 microns, and were transferred from a photograph made under identical magnification conditions of a 10 micron-spacing objective micrometer. Because the photographs were made under bright-field illumination, the damage microsites appear black in the photographs. That appearance does not necessarily suggest that the microsites are strong absorbers after creation. The same appearance would result for no absorption, but instead only scattering of light out of the collection solid angle of the microscopic objective. The microsites do scatter light strongly, as verified by observation with dark-field illumination. The morphology of fig. 1 is typical for all the crystalline materials that we tested.[1,2] The morphology in the tested non-crystalline materials (silica and laser glasses) showed less distinct microsites, however. Such a difference is to be expected due to the lack of surrounding crystalline

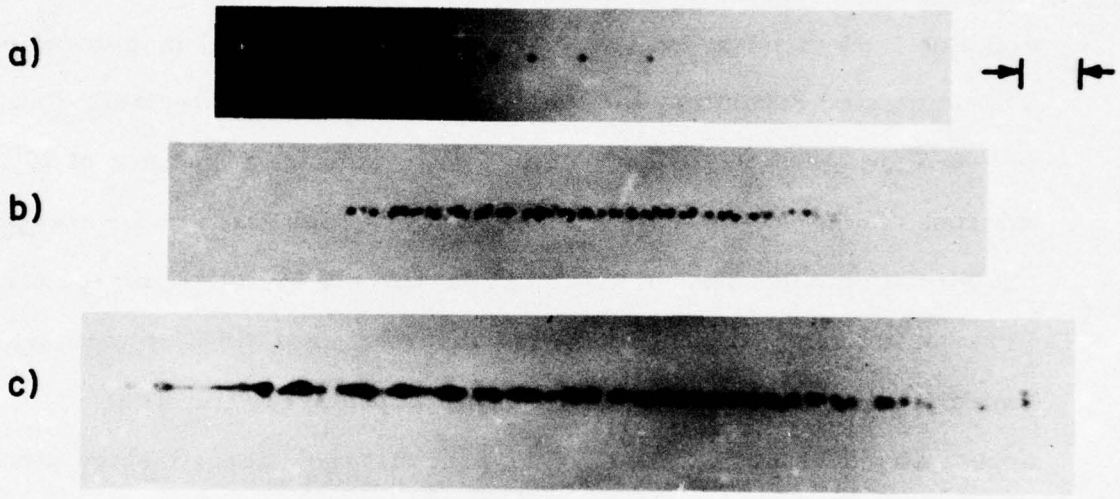

Fig. 1 Breakdown morphology in a NaCl sample produced by 1.064 μm, nominally 30 psec laser pulses focused to an e^{-1} rms intensity radius of 3.3 μm. The scale markers denote a distance of 10 μm, and the pulses were incident from the left. The maximum rms electric field values reached at the focal point in Figs. 1a-c were 1, 20, and 52%, respectively, above the previously measured threshold.

Fig. III.8

medium. The crystalline backdrop provides a light scattering discontinuity between unmelted crystalline structure and melted material which re-solidifies presumably into a disordered state.

Figs. 1a-c illustrate the damage morphology for three different input intensities. In fig. 1a, the maximum rms electric field reached at the focal point was 7.4 ± 1.1 MV/cm (corresponding to 65.6 kW). The breakdown threshold found previously[1] for NaCl was 7.3 ± 1.1 MV/cm, and therefore fig. 1a illustrates damage essentially at threshold. The damage is accordingly observed to consist of a small number of isolated scattering centers localized on the focal axis, each of which is the vestige of a laser-induced microplasma. Each microplasma began from a single, or perhaps a few, easily freed electrons along the focal axis during the passage of the laser pulse. Fig. 1b illustrates the damage in the same sample under the same focusing conditions due to an 86.3 kW pulse with maximum focal point electric field of 8.7 MV/cm, about 20% above threshold. A pulse of 127.6 kW and 11.1 MV/cm maximum field (52% above threshold) produced the damage shown in fig. 1c.

The diameter of the microsites in the figures is typically about 1 μm. If we assume that the microplasma began with an electron located at point $\vec{r}'$ at the beginning of the pulse and model the growth of the plasma by a simple diffusion model, we may estimate the expected spatial extent of the light-scattering remains of such a microplasma to have a diameter $\approx 2|\vec{r} - \vec{r}'|$ of roughly $4\sqrt{DT_p}$. Here T_p is the laser pulse duration (FWHM, 30 psec.) and D is the electron diffusion coefficient, which is expected to have an average value for the high electric fields encountered here of roughly 1 to 10 $cm^2/sec.$[5] These two numbers bracket the microsite

diameter by about 0.2 and 0.7 microns. This rough estimate is consistent with the observed diameter. It is evident that for laser pulses with duration a few times longer than the present 30 psec FWHM duration, the focal region would show continuous breakdown. Resolved microsites would not be observed. Such continuous morphology was observed by Yablonovitch,[6] Fradin et al.,[7] and others in damage studies with nanosecond pulses.

Just at threshold (2.2×10^{11} W/cm^2 maximum focal point intensity) the volumetric density of microsites from fig. 1a is approximately 4×10^9 cm^{-3}, corresponding to the observed linear density of 1.5×10^3 cm^{-1}. The maximum density in fig. 1b is about 2×10^{11} cm^{-3}, for a maximum focal point intensity level of 3.1×10^{11} W/cm^2. This density decreases slowly out to the extremities of the damage, where the maximum field attained was the threshold value and the density is approximately equal to that in fig. 1a. In fig. 1c one observes along the track the progression in density of microsites from approximately that of fig. 1a, at the extremities of the damage, through that of fig. 1b, into a region where the damage along the focal axis has become continuous, except for short discontinuities caused or enhanced perhaps by diffractive shadowing.

The damage sites just above threshold are statistically spaced and symmetrically distributed within their region of occurrence along the axis. There is initially no shadow effect due to absorption and scattering out of the incident beam. The light diffracts readily around the damage sites in the trailing edge of the pulse and the effective integrated intensity on axis is hardly diminished. At higher intensities the loss of incident intensity due to damage spots creates the asymmetry noticeable in fig. 1c.

The maximum intensity reached at the focal point in fig. 1c was 5.0×10^{11} W/cm^2. It is important to note that the electric field and intensity values discussed in this paper are maximum rms values reached only instantaneously as the temporally gaussian laser pulse passed through a given spatial point in the sample.

Much discussion[8-15] has taken place in the recent literature concerning the number and origin of initiating electrons for the avalanche process, and on their influence in associated aspects such as the statistical nature of laser-induced breakdown. In the original work by Yablonovitch[6] which established 10.6 μm optical breakdown as an avalanche process closely related to DC breakdown, the initial electron density N_o in the avalanche relation

$$N(t) = N_o \exp\left[\int_{-\infty}^{t} \eta\{E(t')\}\, dt'\right] \qquad (1)$$

had to be obtained essentially by order-of-magnitude guesswork.[16] The resulting successes of the avalanche model have been due to the weak dependence of most aspects on N_o. However, statistical aspects of laser-induced breakdown depend markedly on N_o.[13-15] The microsite density in figure 1 may be identified with the density N_o. It is of course possible that more than one initiating electron leads to the production of one microsite. Thus the derived value of N_o is approximate, and has the order of magnitude of 10^{10}/cm^3, in agreement with past summptions.[8] The production mechanism of these electrons could be investigated in more detail with our observation technique. It has been argued[12] from electrical conductivity properties that 10^9 free electrons per cm^3 do not exist in

insulating crystals, but that initiating electrons are produced[9, 12] at 1.06 μm promptly by two-photon ionization of ground-state F centers which may occur in concentrations as high as $10^{11}/cm^3$, even in a clear crystal with linear absorption coefficient $\alpha \lesssim 10^{-4}\ cm^{-1}$ at 1.06 μm. It is evident that further studies of this nature as a function of F-center concentration, temperature, ambient light, etc., would be useful in fully understanding this aspect of laser-induced breakdown. Any color center densities must be implanted without concomitant introduction of metallic colloids which would confuse subsequent data interpretation.

The damage microsites are clearly confined to a narrow region on the axis of the focal spot, where the laser intensity is maximum. The region grows both in length and in diameter, with the amount by which the maximum laser intensity exceeds the threshold value. The region has an ellipsoidal shape and is plotted as the dotted line in figure 2 for the case of figure 1b. It may be roughly interpreted as the volume element in which the laser intensity exceeds the threshold value. These data are testimony to the reproducibility of the laser pulses and their effects.

The damage is due to heating of the lattice by resistive losses of the electrons in the plasma. Since the heat diffusion length during the picosecond pulse is much smaller than the electron diffusion length which determines the size of the microsite, the temperature rise in a microsite located at the point (r, z) may be calculated from

$$T(r, z, t) = \frac{e^2 \tau_c}{mC(1 + \omega^2 \tau_c^2)} \int_{-\infty}^{t} N(r, z, t') \left| E(r, z, t') \right|^2 dt' , \quad (2)$$

where the laser electric field distribution is given by

$$|E(r,z,t)|^2 = \frac{E_0^2}{1+z^2 z_{RE}^{-2}} e^{-(t/\tau)^2} \exp\left\{-r^2/[\rho^2(1-P(t)P_{cr}^{-1})(1-z^2 z_{RE}^{-2})]\right\} \quad (3)$$

The electron density is given by eq. (1) where the ionization rate η may be calculated from[18, 1]

$$\log \eta \{E(r,z,t)\} = 3.58 \log E(r,z,t) + 8.62 \quad , \quad (4)$$

for E between 1.0 and 9.0 in units of MV/cm. For N_o in eq. (2) we use one electron within a microsite volume, or $N_o = 2 \times 10^{12}$ cm^{-3}. In expression (2) above, e and m are the free-electron charge and mass, respectively, C is the sample heat capacity per unit volume (1.85 J/cm^3 ^{o}C) for NaCl, ω is the laser angular frequency, and τ_c is the effective electron collision time which we have taken here to be ω^{-1}.[18] In eq. (3) E_0 is equal to $E(0,0,0)$ which is the maximum rms field reached at the focal point, occurring at $t = 0$. The e^{-1} intensity radius in the focal plane is ρ (= 3.3 μm here), and z_{RE} is the Rayleigh distance for the electric field, $2\pi n \rho^2/\lambda$, or 98.5 microns here (where n is the linear refractive index). The e^{-1} temporal intensity half-duration is denoted above by τ, having values of 23.2, 19.4 and 27.0 psec, respectively, for the pulses which produced figs. 1a, b, and c.[3] $P(t)$ denotes the laser pulse power. P_{cr} is the critical power for self-focusing, taken here[1] to be 166 kW for NaCl. Using eqs. (1-4), we may compute the three dimensional surface on which the maximum temperature reached just equals the melting temperature of NaCl (800^{o}C) and within which any volume element of microsite size would be melted, if it contained an initial electron. The result of this calculation is plotted as the solid line in fig. 2. The good agreement,

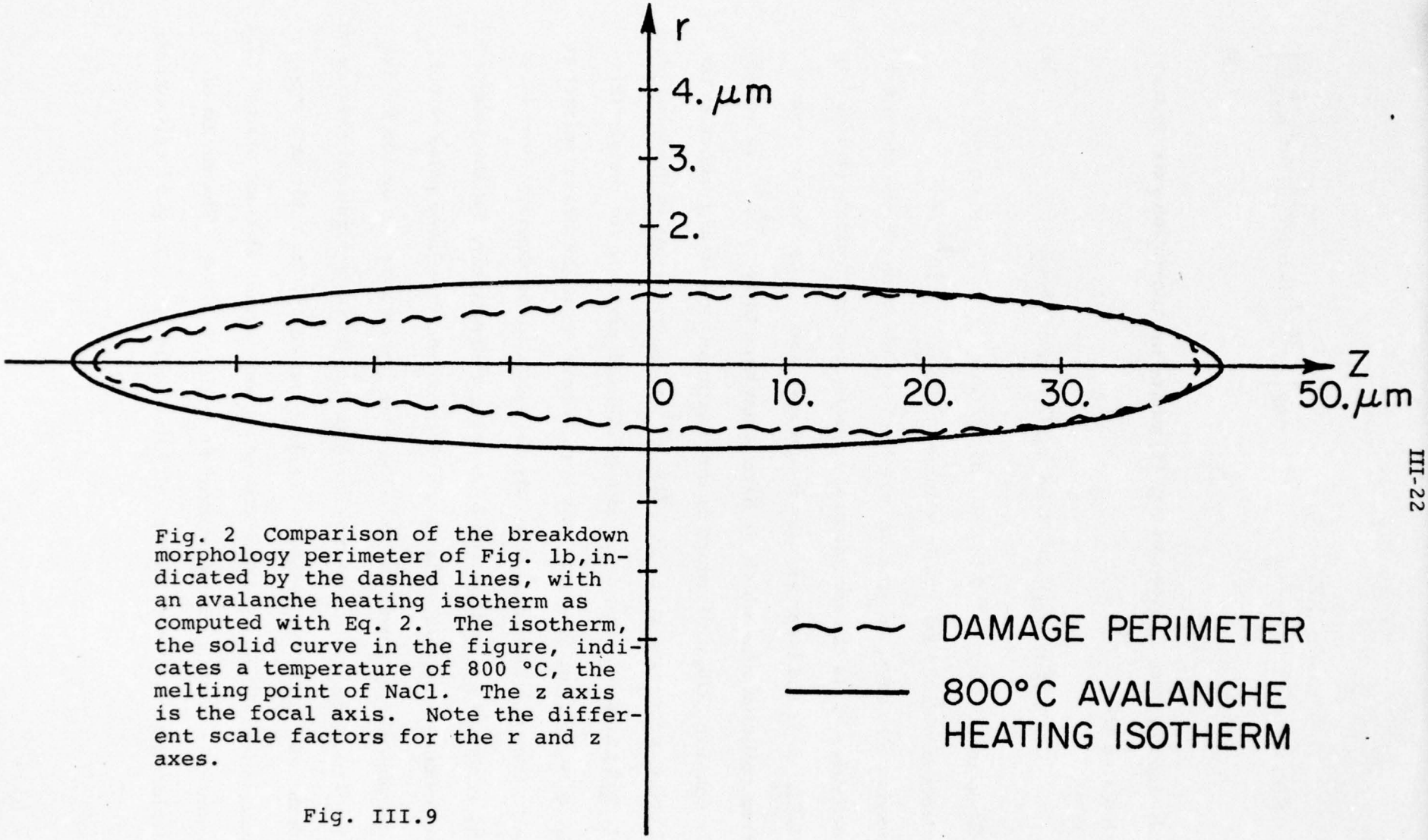

Fig. 2 Comparison of the breakdown morphology perimeter of Fig. 1b, indicated by the dashed lines, with an avalanche heating isotherm as computed with Eq. 2. The isotherm, the solid curve in the figure, indicates a temperature of 800 °C, the melting point of NaCl. The z axis is the focal axis. Note the different scale factors for the r and z axes.

Fig. III.9

especially as to the shape of the region with damage sites, is strong evidence that the avalanche ionization mechanism is responsible for the damage.

The difference in size of the region with damage shown in figures 1a and 1b, corresponding to a difference in input pulse power of only 32 percent, cannot be explained on the basis of absorbing inclusions. These (invisible) inclusions would have to be uniformly distributed with a density of 10^{11} cm^{-3}, and would all have to be uniform in absorptivity and size. They would also have to vary in a systematic way to explain the observed characteristic threshold for each bulk material,[1] in particular the systematic compositional variation throughout the periodic table for the alkali halides. Since the specter of absorbing inclusions, influence of which was carefully assessed and eliminated in the present experiments, was raised in a recent publication,[19] the question of metallic Na inclusions in NaCl is considered in further detail. The invisible inclusions are obviously smaller than the wavelength of blue light (< 0.4 μm), but in order to melt a volume of this size to produce microscopically visible damage, they must have a diameter at least as large as about 0.1 μm. This number was calculated by solving the transient heat conduction boundary value problem for the absorber-host system, using the Mie absorption cross section[20] and the incident intensity. If the sample contains $10^{11}/cm^3$ of Na particles with a diameter larger than 0.1 μm, one would of course find a linear attenuation coefficient many orders of magnitude larger than the observed attenuation coefficient of $< 10^{-4}$ cm^{-1} in Harshaw NaCl samples.[21]

Other experiments[19, 22] also showed filamentary damage of up to 1 mm track length and were carried out at power levels that allow a moving self-focal spot[23, 24] to develop.

In our experiments the effects of incipient self-focusing were carefully corrected[1] by the method proposed by Zverev and Pashkov[25] and by Fradin.[26] Our results add further strong evidence to that of earlier papers[1, 2, 6, 7, 27] that the fundamental damage threshold is determined by the avalanche ionization process.

The authors are indebted to Prof. L. Taylor of Harvard University for the use of microscopy equipment, and to Prof. F. Lüty of the University of Utah and Prof. E. Yablonovitch of Harvard for helpful discussions. The skillful sample preparation of S. Maurici is greatly appreciated.

References

*Research supported in part by the National Aeronautics and Space Administration, the Joint Services Electronics Program, and by the Advanced Research Projects Agency.

1. W. Lee Smith, J. H. Bechtel, and N. Bloembergen, Phys. Rev. B 12 (1975) 706.

2. W. Lee Smith and J. H. Bechtel, Appl. Phys. Letters 28 (1976) 606.

3. W. Lee Smith and J. H. Bechtel, J. Appl. Phys. 47 (1976) 1065.

4. J. H. Bechtel and W. L. Smith, Phys. Lett. 55A (1975) 203.

5. F. Seitz, Phys. Rev. 76 (1949) 1376; E. M. Conwell, High Field Transport in Semiconductors (Academic Press, New York, 1967).

6. E. Yablonovitch, Appl. Phys. Letters 19 (1971) 495.

7. D. W. Fradin, E. Yablonovitch, and M. Bass, Appl. Opt. 12 (1973) 700.

8. A review of work concerning laser-induced breakdown in solids through 1973 was given by N. Bloembergen, IEEE J. Quantum Electr. 10 (1974) 375.

9. P. Bräunlich, A. Schmid and P. Kelly, Appl. Phys. Letters 26 (1975) 150.

10. P. Kelly, P. Bräunlich, and A. Schmid, Appl. Phys. Letters 26 (1975) 223.

11. N. L. Boling, P. Bräunlich, A. Schmid, and P. Kelly, Appl. Phys. Letters 27 (1975) 191.

12. M. Sparks and C. J. Duthler, "Theoretical Studies of High-power Ultraviolet and Infrared Materials " (Fifth Technical Report, Contract No. DAHC15-73-C-0127, Xonics, Inc., Van Nuys, Calif., U.S.A. 91406), 1975.

13. M. Bass and H. H. Barrett, IEEE J. Quantum Electr. 8 (1972), 338; and Appl. Opt. 12 (1973) 690.

14. M. Bass and D. W. Fradin, IEEE J. Quantum Electr. 9 (1973) 890.

15. D. Milam, R. Bradbury, R. Picard and M. Bass in Laser Induced Damage in Optical Materials: 1974, A. J. Glass and A. H. Guenther, eds. (NBS Special Publ. No. 414), p. 169.

16. C. Kittel, Introduction to Solid State Physics, 4th Edition (Wiley, New York, 1971), p. 631.

17. J. J. Markham, F-Centers in Alkali-Halides, (Academic Press, New York, 1966).

18. E. Yablonovitch and N. Bloembergen, Phys. Rev. Letters 29 (1972) 907.

19. Y. K. Danileiko, A. A. Manenkov, V. S. Nechitailo, and A. I. Ritus, Soviet J. Quantum Electr. 4 (1975) 1005.

20. H. C. van de Hulst, Light Scattering by Small Particles (Wiley, New York, 1957).

21. M. Hass, J. W. Davisson, H. B. Rosenstock, J. A. Shinkman and J. Babiskin, Optical Properties of Highly Transparent Solids, ed. S. S. Mitra and B. Bendow (Plenum, New York, 1975), p. 435.

22. V. A. Gridin, A. N. Petrovskii, and S. L. Pestmal, Soviet J. Quantum Electr. 4 (1975) 1270.

23. C. R. Giulianno and J. H. Marburger, Phys. Rev. Letters 27 (1971) 905.

24. G. M. Zverev, E. K. Maldutis, and V. A. Pashkov, Soviet Physics JETP Letters 9 (1969) 61.

25. G. M. Zverev, and V. A. Pashkov, Soviet Physics JETP 30 (1970) 616.

26. D. W. Fradin, IEEE J. Quantum Electr. 9 (1973) 954.

27. D. W. Fradin and M. Bass, Appl. Phys. Letters 22 (1973) 206.

CHAPTER IV.

PICOSECOND LASER-INDUCED BREAKDOWN AT 5321 Å: OBSERVATION OF FREQUENCY-DEPENDENT BEHAVIOR*

W. Lee Smith†, J. H. Bechtel‡ and N. Bloembergen
Gordon McKay Laboratory, Harvard University
Cambridge, Massachusetts 02138

Laser-induced dielectric breakdown at 5321 Å has been investigated in six materials: KH_2PO_4, fused SiO_2, NaCl, CaF_2, NaF, and LiF. The laser pulses were nominally 21 psec in duration and were obtained by the frequency doubling of single 1.064 μm pulses from a mode-locked YAlG:Nd laser system. The frequency doubling was carried out in a temperature phase-matched CsH_2AsO_4 crystal, resulting in spatially smooth, reproducible, diffraction-limited, 5321 Å pulses. Strict attention is given to the complications introduced by self-focusing. The new thresholds for breakdown at 5321 Å are compared with thresholds measured previously at 1.064 μm with the same laser system. This comparison, as a function of material band gap $\mathcal{E}_G$, charts experimentally for the first time the transition of the character of laser-induced breakdown as it becomes strongly frequency-dependent. A frequency-dependent decrease in the threshold of ~30% is observed for KH_2PO_4, for which three 5321 Å photons

exceed $\mathcal{E}_G$ in energy. Frequency-dependent threshold increases of up to 44%, varying smoothly with $\mathcal{E}_G$, are observed for the other materials. These observations are discussed with regard to models for the processes involved in the breakdown, which are avalanche and multiphoton ionization.

A. Introduction

In this paper we present experimental results which characterize for the first time the transition of laser-induced dielectric breakdown from the familiar DC limit into the regime where both avalanche ionization frequency dependence and multi-quantum effects are clearly observed. This study represents a systematic frequency extension of our previous 1.06 μm investigations of picosecond dielectric breakdown in transparent solids.[1-3]

Laser-induced breakdown was reported in the literature early in the 1960's. However, the earnest study of DC breakdown has taken place since the 1930's. Indeed, it has been pointed out[4] that laboratory observation of DC breakdown in glass was reported as early as 1799, by A. Van Marum in the first volume of Annalen der Physik.[5] Van Marum's efforts at producing high voltages were limited by breakdown through the walls of his storage jars. Beginning in 1931, experimental progress in DC breakdown threshold measurement was achieved by von Hippel.[6] Theoretical developments by Frohlich[7] beginning in 1937 and Seitz[8] in 1947 proposed and described avalanche ionization as the basic physical mechanism involved in the DC case. In 1971 Yablonovitch performed laser-induced breakdown experiments[9] at 10.6 μm in which the similarity of the threshold between the infrared and earlier DC data, both in the trend with material composition and in absolute magnitudes, was compelling. Avalanche ionization was established as the intrinsic process whereby an infrared laser pulse is able to

induce breakdown in pure dielectric material. Further controlled laser experiments at 1.06 μm[10] again found breakdown thresholds not significantly different from those at DC and 10.6 μm, either in trend or magnitude. At the still shorter ruby wavelength of 6943 Å, a systematic increase over previous thresholds was reported.[11] As will be discussed in a later section, the pattern of increase was unusual, however, and it now appears that the threshold increase in the low band gap materials may have been an artifact. Yet at least part of the large relative increase in the NaF threshold reported in that study was quite probably an observation of true behavior and therefore the first indication of frequency dependence in avalanche ionization breakdown processes. An increased resistance to surface damage in several materials at 6943 Å over that at 1.064 μm was also reported[12] in 1973. Because that investigation involved rather different experimental conditions (surface breakdown, multiple pulse irradiation of the same sample volume) than the present work, we will not consider it further.

At wavelengths shorter than 6943 Å several experiments have been performed to date.[13-18] However, in each of these experiments self-focusing was present. No attempt was made to extract the self-focusing influence in order to measure a breakdown threshold. At best, such experiments yield a measure of the critical power for self-focusing. Further interpretive difficulties were caused by the use of multimode lasers,

entire mode-locked pulse trains, or harmonic generation crystals allowing walk-off. Under such conditions reliable breakdown thresholds are rarely obtainable.

Thus, up to electromagnetic angular frequencies ω of almost 3×10^{15} Hz, the basic behavior of bulk dielectric breakdown has been observed to be quite similar to the behavior at zero Hertz. The concise reasons for this steadfast behavior over such a remarkable frequency range are two-fold: i) The hot electron collision time (τ_c) in dielectrics is very fast ($<10^{-15}$ sec). ii) In experiments up to 6943 Å, the photon energies were not a sufficiently sizable fraction of the material band gap, $\mathcal{E}_G$. In Fig. 1 we illustrate the schematic frequency dependence of the breakdown threshold E_B, as has been anticipated for some time.[19] The low frequency, pure avalanche region (solid segment) is the range of investigation prior to this study. As discussed elsewhere,[9] the relation

$$E_B(\omega) = E_B^{DC} \left[1 + \omega^2 \tau_c^2\right]^{1/2} \qquad (1)$$

has been used to predict the frequency dependence of laser-induced breakdown in the region of departure from the DC limit. In Fig. 1 the solid segment and its dotted extension have the form of Eq. 1. The aforementioned increase in the NaF threshold at 6943 Å indicates that $h\tau_c^{-1} \simeq \hbar\omega_{ruby}$ (1.79 eV) in NaF, and roughly indicates the $h\tau_c^{-1}$ position on the $\hbar\omega$ axis of Fig. 1.

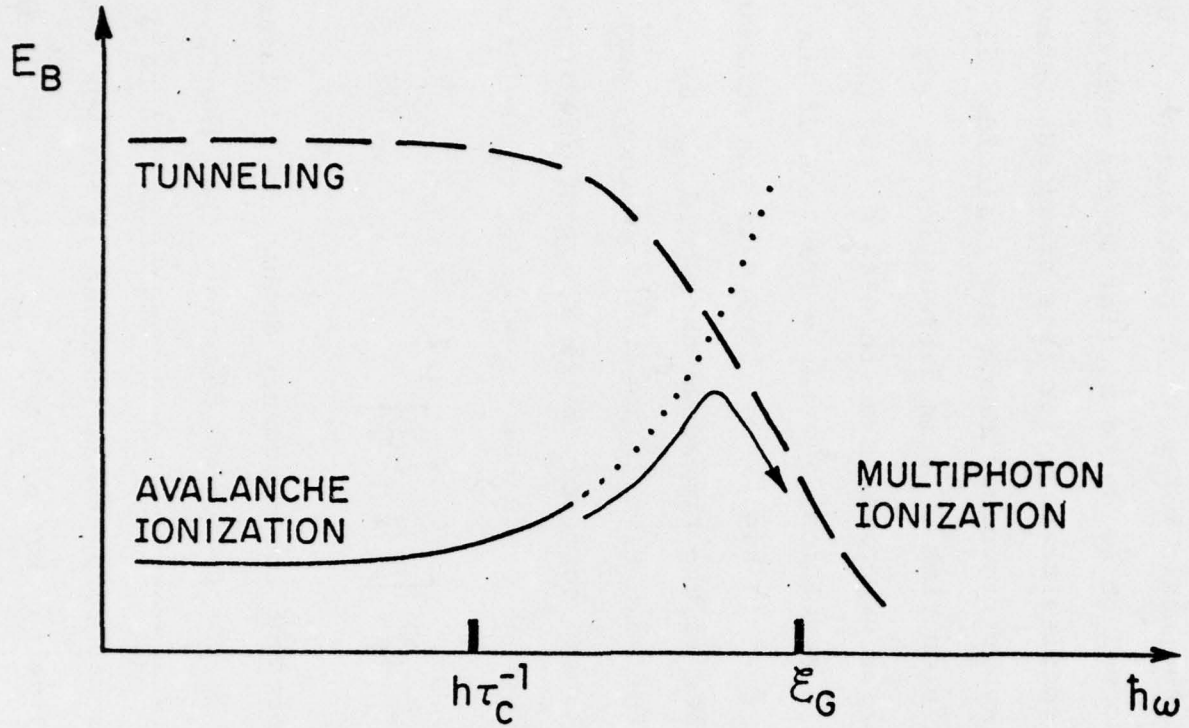

Fig. 1 Schematic frequency dependence of the two intrinsic physical processes involved in laser-induced breakdown: avalanche ionization and multiphoton absorption ionization. $\mathcal{E}_G$ denotes the optical band gap of the material and $h\tau_c^{-1}$ the energy associated with the electron collision time τ_c. The solid curve is the region investigated prior to this study. The present work investigates the region located by the arrow.

Fig. IV.1

The dashed curve outlines the frequency dependence of the Keldysh tunneling mechanism.[20] As the photon energy becomes sizable compared to the material band gap, this tunneling mechanism is described as multiphoton ionization. At some point in this transition the multiphoton ionization probability becomes large enough to effectively assist the breakdown process, still classifiable mainly as avalanche ionization. Several papers[21-23] recently have considered aspects of this combination process. One immediate consequence of the multiphoton ionization assistance is the ready supply of initial electrons with which the breakdown process may proceed. For sufficiently lower frequencies, the productions of such electrons is a subtle matter. As the photon energy exceeds $\mathcal{E}_G/3$, we expect the threshold to reverse its trend as the arrow indicates in Fig. 1. As the photon energy is increased beyond $\mathcal{E}_G/2$, gross two-photon absorption (TPA) will occur. At such frequencies, breakdown experiments utilizing an external focusing lens will be complicated considerably by TPA energy depletion and distortion of the laser pulse in the medium before the lens focal region.

One should note the manner in which the two curves in Fig. 1 will shift horizontally as the material parameters $\mathcal{E}_G$ and $h\tau_c^{-1}$ are changed and $h\omega$ is held fixed. Because $h\tau_c^{-1}$ is likely to be less sensitive to $\mathcal{E}_G$ than is the threshold for strong multiphoton absorption, the most demonstrative effect on Fig. 1 from changing to a material with larger $\mathcal{E}_G$ would be

the shift of the dashed curve to the right and creation of a larger hump in the composite threshold trajectory. Therefore a comparison of breakdown thresholds at two different laser frequencies, both in the region of the transitional hump, for a series of materials and band gap, would provide a test of the surmised behavior which is illustrated in Fig. 1. From our picture, one would expect from such a comparison to see a systematic increase in $\left[E_B(\omega_2) \; / \; E_B(\omega_1) \right]$, where $\omega_2 > \omega_1$, as a function of material band gap. We will present data later in this paper which depicts just such a systematic increase.

A recent review of dielectric breakdown induced by laser pulses is found in Ref. 19. Recent theoretical papers which will serve as well to introduce the reader to segments of the literature are found in Ref. 24 by Holway and Fradin and Ref. 25 by Sparks and Duthler. Numerous papers concerning all aspects of laser-induced dielectric breakdown appear in National Bureau of Standards Special Publications.[26] The 1973 edition of O'Dwyer's book[27] may be consulted for information on DC, as well as high frequency, breakdown phenomena.

Section B outlines the theory necessary for the evaluation of our experiments. Section C relates the experimental details, and we present results in Section D. Comparison of our expermental results with theories on multiphoton contributions to breakdown[4,21] are given in Section E.

B. Theory

The objective of our experiment is to obtain the high electric fields requisite for breakdown, while at the same time minimizing the input pulse power and thus the effects of self-focusing. This we do by tightly focusing the laser pulses into the sample with short focal length lenses. In the absence of any self-focusing, we know that a diffraction-limited light pulse with a Gaussian spatial intensity distribution of radius ρ $\left[I(r) = I_o \exp -(r/\rho)^2 \right]$, focused by a lens of focal length f, will produce an intensity distribution in the focal plane of

$$I_f(r) = (P/A)\, e^{-(r/w)^2} \quad . \qquad (2)$$

Here P is the pulse peak power, defined as

$$P = 2\pi \int_0^\infty dr\, r\, I(r) \quad , \qquad (3)$$

where $A = \pi w^2$, and $w = \lambda f / 2\pi\rho$, if λ is the light wavelength in air. In addition, we know that if the power P in the light pulse exceeds some fraction of the critical power value known as P_1,[28] defined as

$$P_1 = c\lambda^2 / 32\pi^2 n_2 \qquad (4)$$

for a Gaussian pulse, the above focusing behavior is modified by self-focusing. The material parameter which determines P_1 is n_2, the nonlinear refractive index. If E is the rms field amplitude and n is the total refractive index, n_2 is defined via $n = n_o + n_2 E^2 + \ldots$ The equations above may be altered to account for self-focusing with the help of the analytical "aberrationless" or "constant shape" (CS) approximate theory[28-30] if P is "less than" P_1. In that case, Eq. 2 becomes

$$I_f(r) = (P/A)\ (1-P/P_1)^{-1}\ e^{-(r/w)^2} \quad . \quad (5)$$

Depending on whether P_1 is known for a given material of interest, Eq. 5 may be used in two different ways for breakdown threshold measurements.

If n_2 and thus P_1 are not known, then Eq. 5 may be used to measure both the breakdown threshold electric field E_B and P_1, simultaneously, as was done by others[31-33] and by ourselves in earlier 1.064 μm studies.[1-2] In that situation, lenses of different focal area A_i are used to produce breakdown at the focal point, each lens requiring a different input power P_i. One may then plot the various reciprocal input powers P_i^{-1} versus the respective focal areas A_i^{-1}. As long as all P_i are much "less than" P_1 (an unknown), the points will define a straight line, as indicated by Eq. 5. Fig. 2

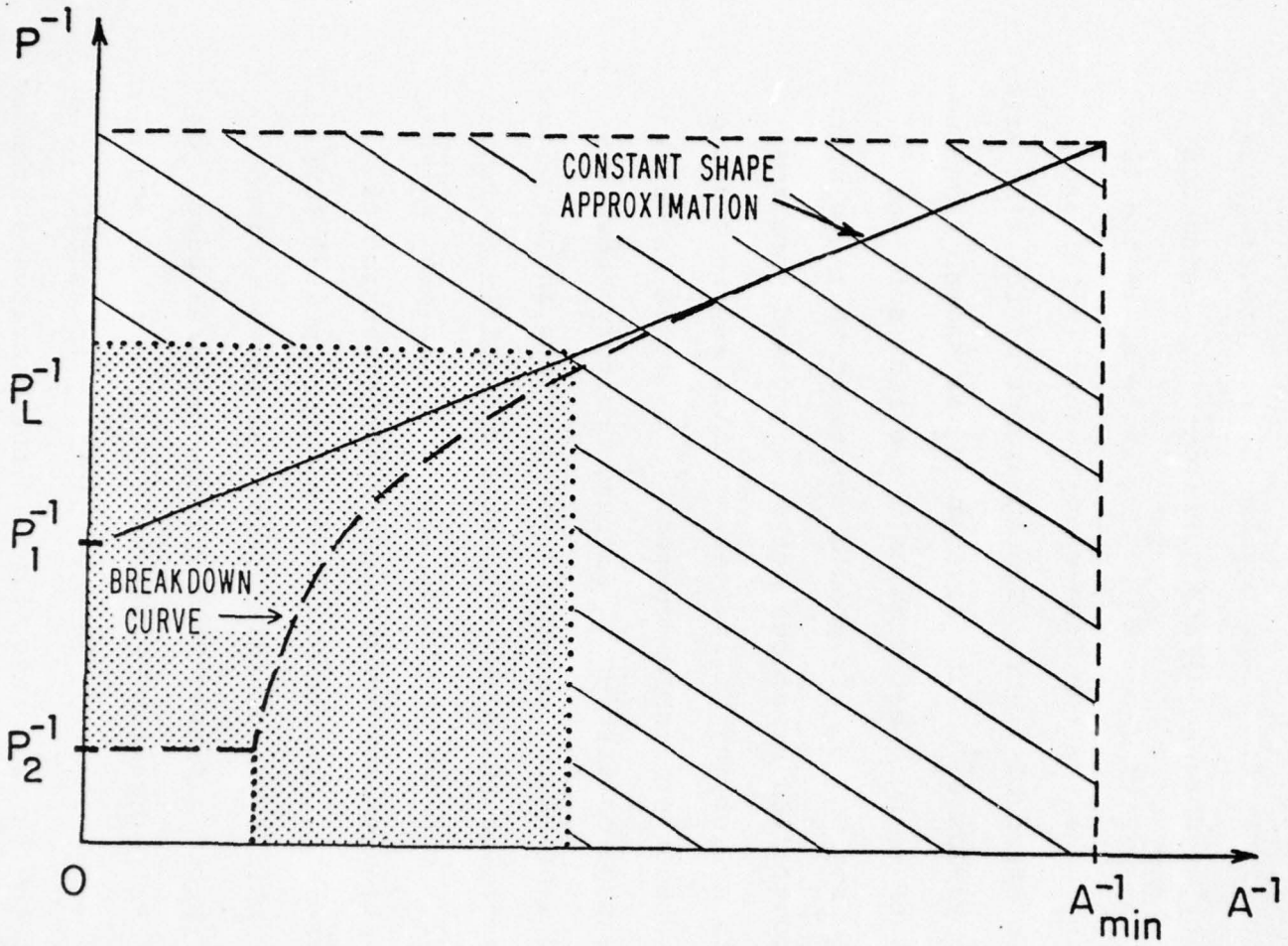

Fig. 2 Illustration of the slope-intercept breakdown construction, as given by Eqs. 5 and 6, wherein one plots for a given lens the reciprocal pulse input power (P^{-1}) versus reciprocal focal area (A^{-1}). The dashed curve is defined by the breakdown properties of the material, and the solid line is from the constant shape approximation. P_1 and P_2 are the "paraxial" and the "catastrophic" critical powers, resp. See Sec. B for discussion of the two curves. A_{min} is the minimum focal area obtainable with a given wavelength.

Fig. IV.2

indicates these features schematically. There the slope of the solid line is $I_f(0)^{-1}$ (and equals the reciprocal breakdown intensity at threshold) and E_B is obtained using the relation $E_B = \left[I_f(0) / n_o \varepsilon_o c \right]^{1/2}$, where n_o is the linear refractive index, ε_o is the free-space permittivity, and c is the vacuum speed of light. The intercept of the line with the P^{-1} axis yields P_1^{-1}. If, however, n_2 is known, then the threshold power measurement from only one lens suffices to determine E_B from Eq. 5. It should be stated that the slope-intercept, controlled breakdown method discussed here and previously is an intrinsically less accurate way to measure n_2 than some other available schemes.[34-39] It is, nevertheless, in the face of unknown n_2 values, the only known way to obtain bulk breakdown threshold measurements in the picosecond pulse regime which are corrected for self-focusing.

Aside from the paucity of accurate available n_2 values, another situation exists which thwarts the extension of picosecond breakdown measurements to shorter optical (UV) frequencies. All the above discussion was based on input pulse powers P being "less than" P_1, the critical power for the onset of self-focusing by paraxial rays in an unfocused geometry. The problem lies in our inability to ascribe more precision to the phrase "less than" in the previous sentence. It is not known quantitatively how, in the focused geometry (where an external lens focuses the light pulse into the

material sample), the constant shape approximation breaks down as P approaches and, moreover, exceeds P_1. Fig. 2 illustrates our present understanding of this behavior. The cross-hatched area is the region of validity of the CS approximation. The dashed curve is the locus of (A^{-1}, P^{-1}) points defined by the breakdown threshold of a particular material. The straight line, which is asymtotic to the dashed curve in the low power limit, is defined by Eq. 5 and is the construction used in our previous papers[1-2] to measure P_1. The dotted area in the figure is the region within which the self-focusing behavior has departed from the CS description. The exact functional form of this departure, and thus of the dashed breakdown curve in the dotted region, is not known. Therefore, the exact limiting power level (indicated by P_L^{-1} in Fig. 2), beyond which one should not apply the constant-shape approximation to deduce breakdown thresholds, is not known. It is indicated by careful numerical calculation[28] that the power in a Gaussian pulse must exceed P_1 by a factor of 3.7 before a catastrophic self-focus (a singularity in axial intensity) will occur, in either externally focused or unfocused geometry. This intensity singularity manifests itself by breakdown and other processes, and represents the horizontal segment of the breakdown curve in Fig. 2. This multiple of P_1 leading to the singularity is denoted in the literature by P_2. For pulse powers very near to but less

AD-A031 852 HARVARD UNIV CAMBRIDGE MASS DIV OF ENGINEERING AND --ETC F/G 20/5
DIELECTRIC BREAKDOWN INDUCED BY PICOSECOND LASER PULSES.(U)
OCT 76 W L SMITH, J H BECHTEL, N BLOEMBERGEN N00014-75-C-0648

UNCLASSIFIED TR-665 NL

2 OF 2
AD A031 852

END

DATE FILMED
12-76

than P_2, the maximum axial intensity may be expressed then by Eq. 5 with P_1 replaced by P_2.[28] And in fact, the maximum axial intensity reached at any input power level might be expressed by the relation

$$I_{MAX} = (P/A)\left[1 - P/\{\phi(P)P_1\}\right]^{-1} . \quad (6)$$

Here $\phi(P)$ is presently unknown and must be the result of numerical calculation, but will behave monotonically between the following limits:

$$\phi(P) \rightarrow 1 \text{ for } P << P_1 ,$$
$$\phi(P) \rightarrow 3.7 \text{ as } P \rightarrow P_2.$$

Data published by Marburger[28] indicates that efforts may be made to compute the function $\phi(P)$. Such new results, in a form applicable to any focusing geometry, would be of great use for experiments of many types, expecially with higher laser frequencies considering the restricting λ^2 dependence of P_1. Knowledge of $\phi(P)$ would, for example, remove our present dependence on the CS approximation and allow more than 4 times more power to be used to produce calculable intensities for breakdown studies such as this one. In that case the segment of the breakdown curve within the dotted area and down to the P_2^{-1} level would be

useable. Similar applications could be made to studies of absolute coefficients for UV two-photon absorption in solids and liquids, etc. The data presented in this paper will be tabulated so that the breakdown threshold values may be recalculated by the reader in the future, should data on the $\phi(P)$ function appear.

C. Experiment

1. Apparatus

The experimental arrangement is shown in Fig. 3 and is in large part the same as used in Refs. 1-3. The YAlG:Nd laser oscillator is mode-locked by saturable absorber (Kodak 9860). It produces a train of TEM_{oo} transverse mode, 1.064 μm pulses of 30 psec average duration. One of these pulses is selected for use by a KH_2PO_4 Pockels cell which is driven by a laser-triggered spark gap. The selected pulse is then monitored for proper switch-out behavior on a Tektronix 519 oscilloscope (CRO 1). Photodiodes P2 and P3 measure the energy content in two samples from the main pulse, one at 1.064 μm and the other converted to 5321 Å by a KH_2PO_4 crystal. From these two signals we obtain the temporal duration of each individual picosecond laser pulse.[40] With this temporal characterization, the main part of the infrared pulse is converted to a 5321 Å pulse by harmonic generation cell (HG2) containing a cesium dihydrogen arsenate crystal. The

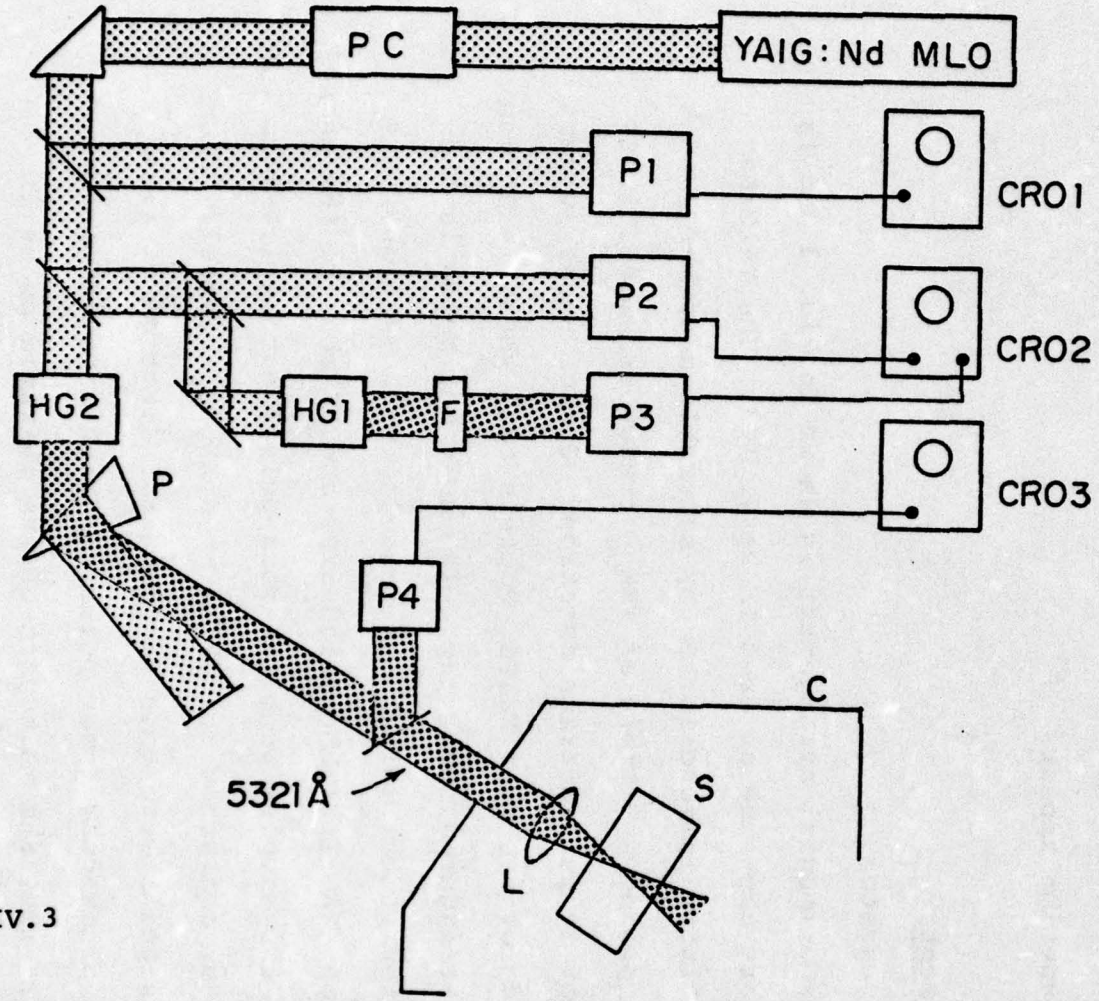

Fig. IV.3

Fig. 3 Schematic diagram of the experimental apparatus. Notation: MLO, mode-locked YAlG:Nd laser oscillator; PC, Pockels cell single pulse selector; P1-P4, photodiode detectors; CROl, Tektronix 519 oscilloscope; CRO 2-3, Tektronix 555 oscilloscopes; HGl, KH_2PO_4 5321 Å generation cell; HG2, CsH_2AsO_4 temperature-tuned 5321 Å generation cell; F, green-pass filter; P, dispersing prism; C, curtain; L, lens; S, sample.

crystal is maintained in an oven at the proper temperature for noncritical or 90° phase-matching. Two characteristics of the green pulse, crucial for this experiment, accrue from 90° phase-matching.[41] First, no spatial distortion of the green pulse occurs by "walk-off," as occurs with angle-tuned phase-matching. The 5321 Å pulse is cylindrically symmetric, without spatial noise, and Gaussian in shape. Fig. 4 is a tracing of an oscillogram from a Reticon linear photodiode array (Reticon Corp., Sunnyvale, California) of a typical green pulse profile. The waveform was smoothed by no more than the width of the tracing pen. Such a distortion-free profile is required for accurate calculation of the electric field distribution of a laser pulse in the focal region of a lens. Second, this harmonic generator produces, for an unlimited length of time, green pulses with the same spatial profile. Such reproducible behavior, over a period of several hours and from day to day, is difficult, if not impossible, to obtain from angle phase-matched crystals. A serious attempt was made by us,[42] prior to the present experiment, to accurately measure breakdown thresholds with 5321 Å pulses generated in an angle-tuned KH_2PO_4 crystal. The effort was not satisfactory for the reasons outlined above. The same set of difficulties will thwart efforts to study breakdown at the third-harmonic frequency of the Nd:YAlG laser, unless materials are found to provide 90° phase-matching for 3547 Å generation.

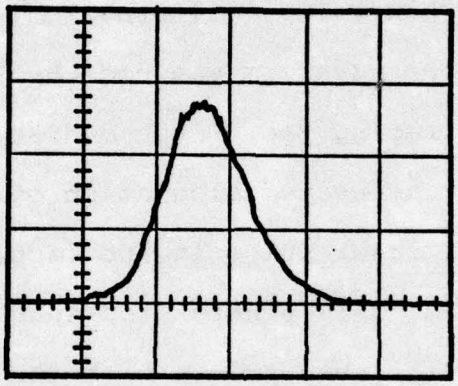

Fig. 4 Oscillogram tracing of the spatial intensity profile of the 5321 Å pulses produced by the CsH_2AsO_4 crystal. The oscillogram was recorded with a commercial linear array of 256 photodiodes with 0.05 mm resolution.

Fig. IV.4

The 5321 Å pulse is separated from the infrared pulse by a prism, oriented to maintain the circular cross section of the green pulse. Photodiode P4 monitors the absolute energy content of the green pulse just before the focusing lens L. Photodiode P4 was calibrated with two Eppley Laboratory (Newport, Rhode Island) thermopiles, themselves calibrated against National Bureau of Standards sources. By using the energy content signal from P4 and the individual pulse duration which we derive from P2 and P3 signals, we obtain the peak power in each individual pulse. The measured full angle of divergence of the harmonic pulses is less than 0.9 mrad. By measuring the cross-sectional area of the pulses at the lens position with the linear photodiode array, and using the design parameters of the lens, we may calculate the area in the focal plane of the lens.[1] The measurements which we report here were made with a 1.0 inch focal length corrected lens, with a calculated focal area (defined as πw^2, where w is the e^{-1} radius of intensity) of 14.8 μm^2. This figure includes contributions from spherical aberration of the lens and the planar sample surface,[1] both of which amounted to a calculated correction to the area of less than 2%. This calculated focal area was checked experimentally by a scanning aperture technique.[1] To within the limiting accuracy of the technique, ±20%, the experimental and calculated areas agreed.

We have employed an average full-width-at-half-intensity duration of 21 psec for our 5321 Å pulses. This duration is shorter than the 30 psec parent pulse duration by $1/\sqrt{2}$, as given by the theory for the ideal frequency doubling of Gaussian pulses in the low conversion efficiency regime. Final individual pulse durations were calculated using this average duration value, the τA technique,[40] and a computer program to account for the temporal stretching of the pulse due to saturation of the conversion efficiency. This last correction is discussed in Section D.1.

2. Procedure

The procedure for each measurement began with the alignment of a sample (dimensions typically 6 mm x 20 mm x 30 mm) in the x-y translating holder so that the pulse propagation direction was normal to the sample face. Then the lens itself was aligned with a reproducible procedure, discussed previously,[1] which was made easier by the visibility of the light in the present experiment. Next the sample was checked for unacceptable surface polishing roughness, a check which was not possible with invisible 1.064 μm light. Shots were fired through the sample, below the breakdown threshold, and the transmitted light was observed on a card. If the transmitted light pattern showed a contribution due to diffraction from polishing scratches, the sample was either repolished until no surface scratch diffraction was observed,

or the sample was deleted from the experiment if sufficient smoothness was unobtainable. The polishing was performed by an experienced technician using synthetic lap material and alumina abrasive particles down to 0.05 μm diameter. Several materials were unfortunately elimiated due to this problem - the relatively soft, small band-gap materials including NaBr, KBr, and KI. It now appears that such surface distortion may have been the cause of the heretofore unexplained rise in the breakdown thresholds, relative to NaCl, of KBr, KI at 1.064 [1] and 0.694 [11] over their values at DC and 10.6 μm. The absence of this problem in another study[10] at 1.06 μm is not understood. At 10.6 μm,[9] however, such submicron roughness would have almost no distorting effect.

After a proper sample and the lens were aligned, a series of 50-100 shots were fired into sites with recorded location in the sample, one shot per site. The pulse power was increased throughout the series, by altering the Pockels cell voltage which changes the position of switch-out from the oscillator train. In contrast to Nd:glass mode-locked lasers, Nd:YAG laser pulses do not vary in duration as a function of pulse position in the train. For each shot, signals from detectors P2, P3, and P4 were recorded and visual observation of microspark formation was used to indicate whether breakdown occured on each shot. Such visual sightings were not used to determine the breakdown threshold, however. If one wishes to meaningfully

compare thresholds measured at different light wavelengths, then the threshold observation mechanism cannot itself be wavelength-dependent. The ocular observation of spark production (with its attendant scattering of subsequently arriving laser light) would be particularly subjective and wavelength-dependent between 1.064 μm and 5321 Å. So the threshold here was defined by the same criterion as used in our previous 1.064 μm study, namely as the minimum electric field value, reached at the focal point and at the peak of the pulse, which produced microscopically observable, permanent damage in the material. The microscopic observation of the matrix of sites was performed after completion of the laser irradiation, using observation conditions identical to those in our 1.064 μm study[3]: Leitz Ortholux microscope, 340 power total magnification, 0.4 NA long working distance objective, blue light field illumination, ~7000 Å resolution.

Although the visual sightings of spark formation were not appropriate for identification of breakdown thresholds, the visual thresholds obtained with the 1.0 inch focal length lens, and also with 1.5 in. and 3.0 in. focal length lenses, were recorded for each material. The calculated focal areas of the two latter lenses were 32.9 μm^2 and 131.1 μm^2, respectively. These visual thresholds were used to investigate self-focusing behavior for pulses having powers between P_1 and P_2. Discussion of that behavior is found later in

Section D.2.

At least three different experimental runs were made on each tested material with each lens to ascertain the threshold reproducibility.

D. Results

1. Dielectric Breakdown Threshold Data

In this section we will present and discuss new results for dielectric breakdown thresholds at 5321 Å, induced by our nominally 21 psec pulses.

Several general characteristics of this damage study were observed to be the same as those encountered in Refs. 1-3. The thresholds were again noted to be sharply defined.[23] That is, our resolution of the thresholds was limited by our experimental uncertainty and reproducibility, which was observed to be ±15%. Again, only rare evidence of the presence or influence of inclusions was observed under the microscope (≲1% of the sites). Again, the results did not vary from site to site within a sample, or among different samples of the same material, by amounts larger than our experimental uncertainty. Fig. 5 exhibits the morphology in two of the sample materials, KH_2PO_4 and LiF. These breakdown sites were photographed with blue light on a Leitz microscope at 250 power magnification and ~0.8 μm resolution. The focal spot radius to the 1/e point of the electric field ($\sqrt{2}$ w) is

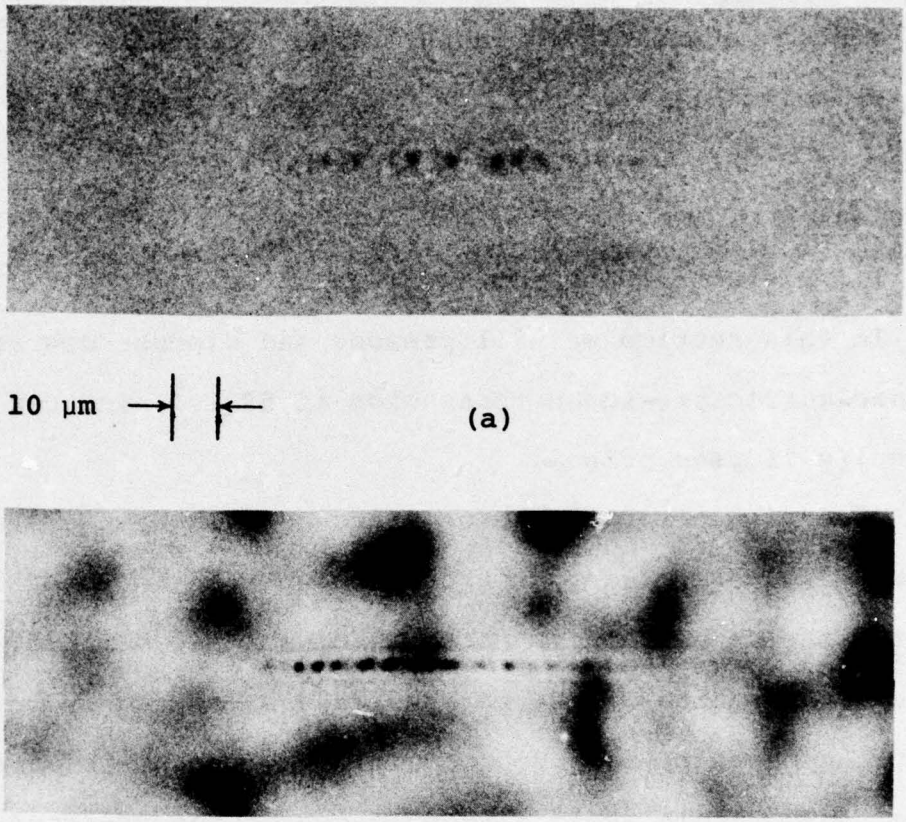

Fig. 5 Breakdown morphology in (a) KH_2PO_4 and (b) LiF, induced by 0.532 μm picosecond laser pulses focused to an e^{-1} rms electric field focal radius of 3.1 μm. The scale markers denote a distance of 10 μm, and the pulses were incident from the left. The maximum rms electric fields reached at the focal point for photographs (a) and (b) were 14% and 40% above the respective thresholds for the two materials. The mottled background appearance in (b) is immaterial.

Fig. IV.5

3.1 μm, and the Rayleigh distance for the electric field (given by $\pi n_o w^2 / \lambda$) is approximately 85 μm. The scale markers in the figure represent a 10 μm distance. The laser pulses which caused the damage of Fig. 5a and 5b had maximum focal point electric fields of approximately 14% and 40% above the respective thresholds for the two materials. The typical microscopically observed damage morphology of Fig. 5 is similar to that reported earlier[3] at 1.064 μm. Except for rare impurity sightings, damage always occurred within a needle shaped volume along the propagation axis at the focal point, the dimensions of which were only ~1 μm by ~10 μm at threshold. The perimeter of this damage was nonlinearly correlated with the incident electric field strength, again as encountered at 1.064 μm. Within the damage perimeter occurred nucleation sites of $\lesssim$1 μm diameter. at a density of 10^{10} cm^{-3} at threshold. No major differences were observed, between 1.064 μm and 0.532 μm morphology, which indicates that the final stages of the damage process are still due to avalanche ionization. A major difference in morphology would indicate massive or dominant influence from multiphoton ionization processes.

Table 1 lists several material parameters for the six tested dielectrics: KH_2PO_4, SiO_2 (fused), NaCl, CaF_2, NaF, and LiF. All the crystalline (monocrystalline) samples were cut so that the laser pulses propagated along the [001] axis,

TABLE IV.1

Test Material Parameters

Material	$\mathcal{E}_G$ (eV)	n_o	n_2 (10^{-13}esu)	P_1 (kW)	P_2 (kW)
KH_2PO_4	6.92	1.5316	1.00 ± 0.30[a]	267	988
SiO_2	7.8	1.4608	1.00 ± 0.08[b]	281	1040
NaCl	8.7	1.5491	4.20 ± 0.84[c]	64	238
CaF_2	10.0	1.4354	1.13 ± 0.34[d]	237	877
NaF	11.0	1.3269	0.94 ± 0.47[e]	283	1047
LiF	12.0	1.3937	0.92 ± 0.16[d]	290	1073

a. Ref. 39
b. Ref. 35
c. Ref. 34
d. Ref. 36
e. Chapter III, Part A of this thesis.

with the electric vector along the [100] axis. The KH_2PO_4 samples were purchased from Cleveland Crystal Co. (Cleveland, Ohio), while the other crystalline materials were purchased from Harshaw Chemical Co. (Solon, Ohio). The fused SiO_2 samples are Suprasil I, purchased from Amersil, Inc. (Hillside, N. J.). Column 2 of Table I lists band gap ($\mathcal{E}_G$) values, all of which (except that for KH_2PO_4) were obtained from standard reference books or manufacturer's data. For KH_2PO_4, we were unable to find either $\mathcal{E}_G$ or optical absorption data in the ultraviolet beyond 2100 Å,[43] which indicates a disturbing lack of knowledge of impurity absorption behavior of this important material in the UV. An ultraviolet spectrogram of our own samples indicates[44] strong absorption beginning at about 1800 Å, or 6.92 eV. For convenience, column 3 lists linear refractive index data, which is needed to convert nonlinear refractive index data (column 4) to third order nonlinear optical susceptibility ($\chi^{(3)}$) data, for comparison with data published elsewhere $\left[n_2 = 12\pi n_o^{-1} \cdot \chi^{(3)}_{xxxx}(-\omega,\omega,\omega,-\omega) \right]$. For KH_2PO_4 and CaF_2, ordinary ray n_o values are appropriate. In column 4, we list the most accurate n_2 values available from the literature for our materials, according to their quoted uncertainties which range between ±8% and ±50%. The last two columns tabulate the critical powers P_1 and P_2, which differ by a factor of 3.7 as discussed earlier.

In Table II we present the new breakdown threshold results at 5321 Å along with comparison data at 1.064 μm. The second column lists values of input power P at breakdown threshold. The ratio of these power thresholds to the respective P_l critical power values from Table I are listed in the third column. The aforementioned focal area of 14.8 μm^2 was corrected slightly ($\lesssim$9%) for each material to account for saturation[45] of the conversion efficiency of 1.064 μm light to the second harmonic. These power dependent correction factors were computed by numerical solution of the harmonic generation equations including pump beam depletion. The actual focal area values used are listed in column 4 of Table II. This spatial broadening (the profile remains Gaussian to a good approximation) due to conversion saturation also lengthens the pulse temporally. All power values in this paper have been corrected by the appropriate small factors ($\lesssim$5%), obtained from the same numerical computation.

The values of P, P_l, A, and n_o from the tables suffice to determine E_B using Eq. 5. The new values so obtained from our studies for the breakdown rms electric field strength, at 5321 Å with nominally 21 psec pulses, are denoted E_B^g(21 psec) and listed in column 5 of Table II. The superscript g denotes the green wavelength. The thresholds range from a low of 12.4 MV/cm for NaCl to a high of 26.5 MV/cm for LiF.

The discussion of the uncertainty in the E_B^g(21 psec)

TABLE IV.2

Dielectric Breakdown Threshold Results

Material	P (kW)	P/P_1	A (μm^2)	E_B^g(21 psec) (MV/cm)	E_B^{ir}(30 psec)† (MV/cm)	E_B^{ir}(21 psec) (MV/cm)	Δ‡
KH_2PO_4	151.2	0.57	16.0	23.4	22.3	33.6	0.70
SiO_2	129.0	0.46	15.9	19.0	11.7	17.6	1.08
NaCl	38.4	0.60	15.1	12.4	7.3	11.0	1.13
CaF_2	146.0	0.62	15.9	25.2	14.4	21.7	1.16
NaF	126.4	0.45	15.8	19.4	10.8	16.3	1.19
LiF	171.3	0.59	16.1	26.5	12.2	18.4	1.44

† Table 2, Chapter III of this thesis.

‡ The quantity Δ is defined as E_B^g(21 psec) / E_B^{ir}(21 psec).

values of Table II is complicated by the unavailability of $\phi(P)$ data. Our experimental conditions allow us to know the $\sqrt{P/A}$ factor in the expression for E_B (Eq. 6) to an estimated ±15%. The absence of $\phi(P)$ data has no effect on the reproducibility of our thresholds, of course, and our experimentally observed reproducibility limit of ~±15% reflects that fact. The absence of $\phi(P)$ data does, however, compound the uncertainty in the absolute numbers which are listed in Table II for E_B^g (21 psec). In column three of Table II, the P/P_1 values range from 0.45 to 0.62, and it is plausible that they are too large to permit the CS approximation to yield high accuracy for the breakdown threshold electric fields from Eq. 5. For that reason we will later consider the full range of possible modification of our results, which in the worst case would be obtained by using P_2 in the denominator of Eq. 5 in place of P_1. For the present, however, we will continue to discuss E_B values obtained with P_1 in Eq. 5 ($\phi(P) = 1$) in the CS approximation.

Our greatest interest lies in determining what effect the doubling of the light frequency has had on these thresholds, by comparing them with the results of our previous study at 1.064 μm.[1] Column 6 of Table II lists the thresholds from that infrared study [denoted E_B^{ir} (30 psec)]. As indicated by the notation, the ir data was taken with nominally 30 psec duration pulses, and it is desirable to separate out the pulse duration dependent changes in these two sets of data so that

we may observe changes due to light frequency, or photon energy, only. In order to convert the E_B^{ir} (30 psec) data to E_B^{ir} (21 psec) data, we require the pulse duration dependence in the picosecond range of the breakdown threshold for the six materials tested. Unfortunately such data is known only for NaCl [1] and, to a lesser degree, for five other alkali-halides. We are restricted, therefore, to an approximate treatment for removal of the pulse duration dependence, based on NaCl data only. From Fig. 6 of Ref. 1, one obtains that the ratio of E_B^{ir}(21 psec) to E_B^{ir}(30 psec) for NaCl is about 11.0 / 7.3 = 1.51. We have used this number to convert the entries of column 6, Table II, to those of column 7. It is, of course, unlikely that the threshold dependence on pulse duration would be exactly the same for the dissimilar collection of tested materials. However, over such a small range of pulse duration (30 psec to 21 psec), the use of a single renomalization factor is reasonable. In that case, the change in breakdown thresholds due to frequency alone, denoted Δ, is the ratio E_B^g (21 psec) / E_B^{ir} (21 psec), and is listed in the final column of Table II. As discussed in Sec. A, the systematic variation of Δ with optical band gap should indicate the presence, if any, of frequency-dependent or quantum effects. Such systematic variation has never before been seen in experiments on laser-induced breakdown. Fig. 6 illustrates this point. In that illustration we have ordered the alkali-halides

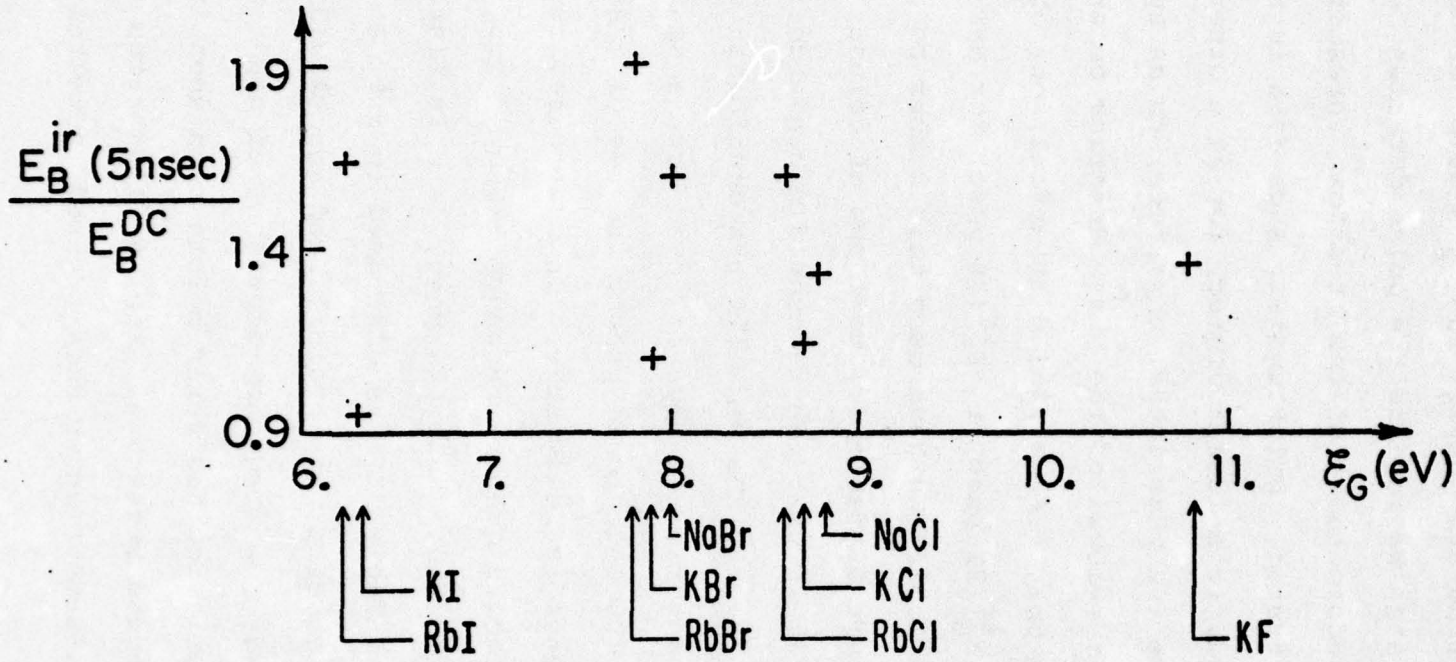

Fig. 6 Illustration of the absence of multiphoton effects in breakdown threshold data for wavelengths down to 1.064 μm. The ratio of thresholds at the Nd frequency[10] to that at zero frequency[6] is plotted versus alkali-halide band gap. No systematic pattern is evident, in contrast with the higher frequency data of Fig. 7.

Fig. IV.6

according to band gap. Plotted along the vertical axis is the ratio of breakdown thresholds from two previous experiments, one at 1.06 μm [10] with ~5.0 nsec laser pulses [E_B^{ir}(5 nsec)] and the other at DC [6] [E_B (DC)]. No systematic behavior of this ratio is observed, and the same is true for any other pair of laser-induced breakdown experiments reported thus far. The basis for this frequency-independent behavior up to 1.06 μm has been discussed previously [19] and is due largely to the two conditions mentioned in Sec. A concerning the brevity of the hot-electron collision time and the size of the band gap in these solids. Even the smallest band gap of 6.2 eV for the tested alkali-halides in the previous 1.06 μm experiments would require at least six photons for the occurrence of direct multi-photon transitions, and such transitions are vanishingly small even at breakdown intensity levels. At the ruby laser frequency (1.79 eV photon energy), four photons are needed to directly cross a 6.2 eV band gap and the probability is still small. At a 1.79 eV or 1.17 eV photon energy, it is probable that the only important role in the breakdown process in these insulators played by multiphoton transitions is the supply of avalanche initiating electrons by the two-photon ionization of defect centers.[21] As mentioned earlier, from our own work in the present and previous[1] studies, it appears now that the unexplained increases in the thresholds (relative to that of NaCl) encountered by Fradin[11] at 6943 Å

and by us at 1.064 μm [1] in soft, low band gap ($\lesssim$8 eV) alkali-halides may have been an artifact due to the undetected sample surface roughness mentioned earlier. Fradin also reported a large increase in the breakdown threshold of NaF over that of NaCl at 6943 Å, and it is likely that most of that increase is a true observation, indicating the condition $\omega\tau_c \gtrsim 1$ as discussed in Sec. A. This observation indeed indicated the departure of the breakdown process from the DC limit at 6943 Å. Up to the present 5321 Å experiment, the NaF observation of Fradin and Bass was the only experimental datum point available for checking the predictions of frequency dependence summarized in Fig. 1.

Now let us discuss the frequency-dependent threshold changes encountered in this study at 5321 Å (2.33 eV). We plot in Fig. 7 the values of Δ listed in Table II versus material band gap $\mathscr{E}_G$. Because of the specific uncertainty introduced by the lack of $\phi(P)$ data, we have plotted in addition the Δ values obtained by using in each case P_2 in Eq. 5, rather than P_1. Due to the closeness of the P/P_1 values for the six materials (see Table I), it is probable that the true data points, were $\phi(P)$ known, would all lie the same relative distance between the circle points and the solid points. That is, the adjustment of the circle points to their true location in Fig. 7 due to full knowledge of $\phi(P)$ would probably result in only a small, nearly constant

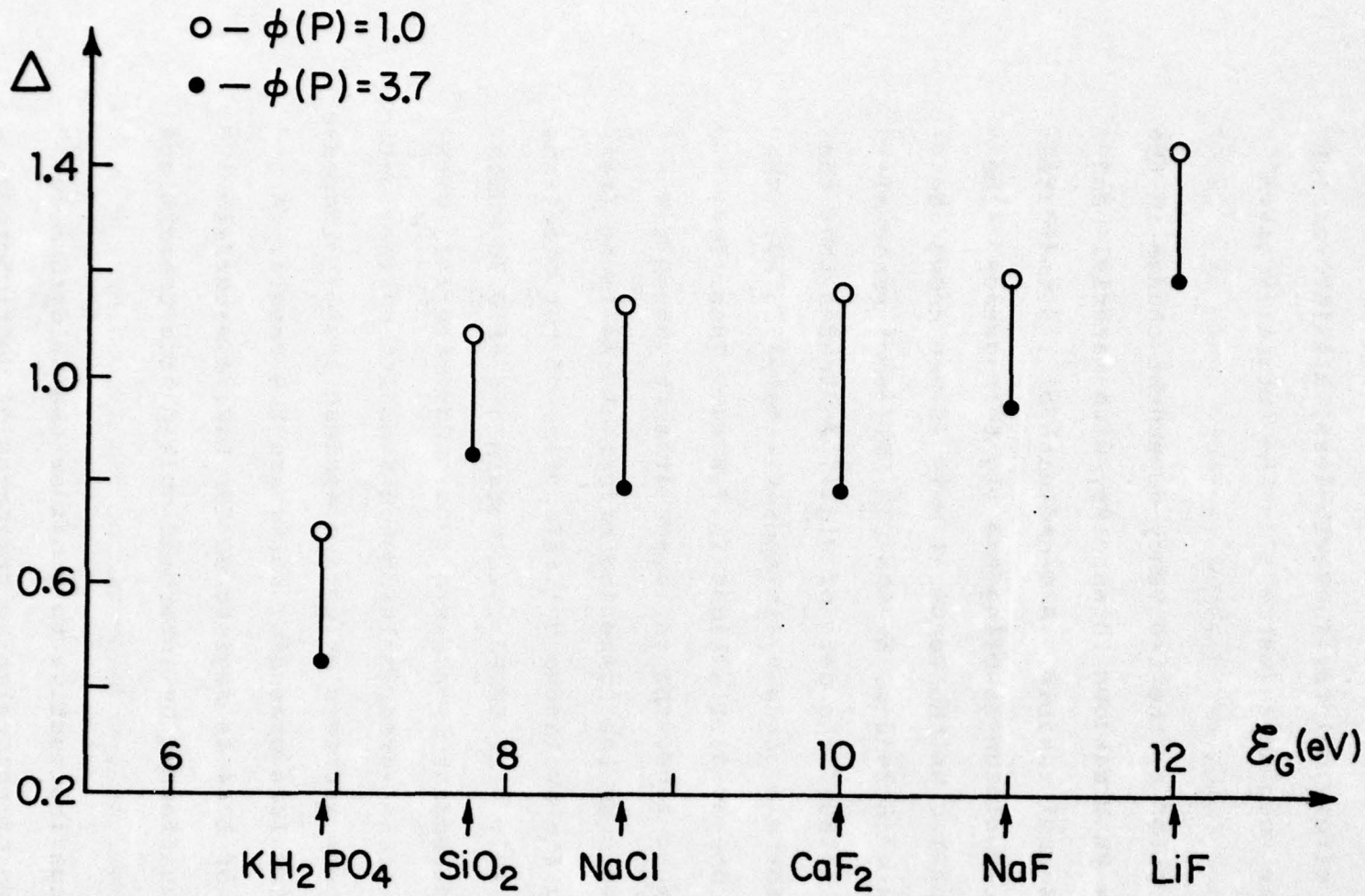

Fig. 7 Illustration of the band gap dependent behavior of the threshold change, Δ, observed in the present experiment. Here Δ is the ratio E_B^g(21 psec) / E_B^{ir}(21 psec) from Table II, plotted versus band gap ($\mathcal{E}_G$) for the six test materials. For each material, the open circle point and the dotted point result from the use of φ(P)=1 and φ(P)=3.7 in Eq. 6, resp., to determine E_B^g(21 psec). The discussion of the trend of this data is found in Sec. D.

Fig. IV.7

lowering of the circle points. (Nevertheless, all information necessary to make such an adjustment in the future is given in this paper.)

The variation of Δ, the frequency-dependent change in the 5321 Å and 1.064 μm breakdown thresholds, with material band gap in Fig. 7 is unmistakable. A Δ ordinate of 1.0 indicates no change in threshold on doubling the light frequency. The exact position of 1.0 on the vertical axis is not known due to the uncertainty introduced by the E_B^{ir} (21 psec) renormalization. Nevertheless, the data of Fig. 7 indicates that the band gap value for a Δ of unity is approximately 7.5 eV. The energy of 3 photons of 5321 Å light is 7.0 eV. Thus, for materials with $\mathscr{E}_G$ < 7 eV, the influence of multiphoton transitions dominates over the competing effect of the light frequency exceeding the avalanche collision time of hot electrons: the result is Δ < 1. For KH_2PO_4, we obtain a Δ of 0.70 which is a frequency-dependent decrease of 30%. For materials with $\mathscr{E}_G$ > 7 eV, 4 or higher-order multiphoton transitions (neglecting defect populations) are less effective against the $\omega\tau_c$ increase at 5321 Å, and Δ values exceeding unity are the result. A maximum Δ value of 1.44 is registered for LiF, a material ($\mathscr{E}_G \simeq 12.0$ eV) unaffected by interband multiphoton transitions at 5321 Å.

It is perhaps instructive to consider the Keldysh model[20] for an indication of the relative strengths of multiphoton

transition effects in our materials. The Keldysh model allows one to estimate for a particular field strength, the transition rate per unit of volume and time for the promotion of electrons from the valence band directly to the conduction band via the lowest-order, energetically sufficient, multi-photon transition process. We have used the free electron mass, in place of the unknown effective mass, the band gap values listed in Table I, and the breakdown threshold field strengths from Table II [E_B^g(21 psec)] to calculate the Keldysh rates. Here, because we wish only to consider the rough variation of this rate for our six materials, such a single field strength estimation will suffice in lieu of a detailed computation. The Keldysh rate for KH_2PO_4, at 23.4 MV/cm with $h\omega$ = 2.33 eV, is large ($\sim 7 \times 10^{28}$ / cm^3-sec) due to the fact that $3h\omega$ slightly exceeds the band gap. As we go to SiO_2 at a field strength of 19.0 MV/cm the rate drops by a factor of over 660 as the lowest-order transition then requires four photons. The further successive decreases in the rate as one proceeds through NaCl, CaF_2, NaF, and LiF are less pronounced: 46,2,21,20, respectively. The trend of these numbers is reflected in the Δ data of Fig. 7. The much greater strength of the three-photon transition for KH_2PO_4, compared to the higher-order transitions for the other materials, is consistent with the significantly lower Δ value for that material from our experiment. The gradual increase in the

Δ value for $\mathcal{E}_G$ > 7 eV is consistent not only with the gradual weakening of the higher-order transition probabilities, but also with the "low" frequency avalanche ionization, Joule heating model embodied in Eq. 1. Thus one sees that the data of Fig. 7 illustrates the continuous evolution of the character of the breakdown process as a function of material band gap from the "pure" avalanche ionization, Joule heating region of large $\mathcal{E}_G$ into the regime where the influence of multiphoton transitions is observable.

2. Self-focusing Behavior

The experiments reported here provide qualitative verification of two aspects of self-focusing behavior in the tightly focused geometry, which to our knowledge were not investigated before. For the self-focusing experiments, we used the same experimental arrangement as in Fig. 3. However, three different lenses (focal lengths 1.0, 1.5, 3.0 in.) were used rather than one as in the previous section. Pulses of increasing power were passed with each lens into the sample materials, one shot per site, and the threshold power for the production of a visible, light scattering plasma at the focal point was recorded. Note that this criterion for plasma scattering (PS) is not identical to the criterion for threshold breakdown as discussed in Sec. C.2. Great care was necessary to remove extraneous scattered light so that only the focal volume was observed. Considering

the sensitivity of the eye at 5321 Å to scattered photons, one would not be surprised that the PS criterion required less power to achieve than the breakdown criterion of permanent microscopic damage. For the 1.0 in. focal length lens which was used for both experiments, the ratio of the PS threshold power to the breakdown threshold power varied with material between about 1.0 and 0.5. Nevertheless, the experiments showed that the PS criterion was sufficient to indicate reproducibly the attainment of a well-defined electric field in the sample. Because it is less time consuming to implement, the PS criterion enabled several materials to be examined.

By plotting the PS power thresholds versus focal area for the three lenses, as discussed earlier and illustrated in Fig. 2, we investigated the trajectory of the breakdown curve in the dotted region of that figure. Referring to Fig. 2, consider the analysis of a data set containing points lying in the power range P_1^{-1} to P_2^{-1}. A straight line fit to those points will yield a vertical axis intercept below P_1^{-1} and, perhaps, even below P_2^{-1}, if the construction in the dotted region of Fig. 2 is correct. Our data for a typical material, SiO_2, is shown in Table III. The calculated focal areas, corrected for saturation as mentioned earlier, are listed in column 2, and PS power thresholds are listed in column 3. Columns 4 and 5 indicate that the power values almost span the P_1 to P_2 region. If one plots this data as in Fig. 2,

TABLE IV.3

Self-focusing Data for SiO_2

f (in.)	A (μm^2)	P (kW)	P/P_1	P/P_2
1.0	15.9	138.9	0.49	0.13
1.5	36.6	260.2	0.93	0.25
3.0	155.7	709.1	2.52	0.68

$$P_{int} = 1138 \text{ kW}$$

$$P_{int} / P_2 = 1.09$$

and fits a straight line to the three points, the intercept of the line with the P^{-1} axis yields a value P_{int} of 1138 kW. As stated in Table III, this quantity indeed exceeds P_2, verifying qualitatively the construction of the dashed breakdown curve as drawn in Fig. 2. A great need exists for accurate numerical computational results of $\phi(P)$ with which the data of Table III could be further tested.

The second aspect of self-focusing behavior which has been qualitatively verified in our experiments concerns the exact input power value, in the tightly focused geometry, which will result in a singularity in axial intensity. In numerical computations, such a singularity is recognized as a rapid increase in intensity of orders of magnitude with only a small incremental increase in input power.[28] In the experimental situation, the singularity is restricted to the breakdown intensity. As listed in Table III, in SiO_2 we were able to focus up to 0.68 of P_2 before initiating a sizable plasma density. Of the six materials we tested, P/P_2 for the 3 in. lens was highest for SiO_2. The other materials registered P/P_2 between 0.32 and 0.57 for the 3 in. lens. All these P/P_2 values correspond to P/P_1 values exceeding unity. Therefore, we have verified that in the tight externally focused geometry, as discussed by Marburger,[28] power of P_1 is insufficient to produce a self-focus singularity. We were not able with our lenses to verify that the full P_2 is so

required, but we did determine that at least ~0.7 of P_2 is required. This data could be extended further, of course, with longer focal length precision lenses.

E. Discussion

In Section D we interpreted the measured, frequency-dependent threshold changes (Fig. 7) in terms of the two-component picture of laser-induced breakdown which is schematized in Fig. 1. The interesting behavior there is provided by competition between the frequency trends of avalanche ionization and multiphoton absorption. One would like to be able to directly compare the experimental data of Fig. 7 with existing theoretical predictions. At present, however, none have been presented for our experimental conditions of wavelength and pulse duration. This situation is due to the unavailability of experimental multiphoton absorption coefficients at 1.064 μm and 5321 Å. This absence is unfortunate because the only available avalanche ionization rate data for laser-induced breakdown is for 1.064 μm wavelength in alkali-halides.[1,46,47]

Multiphoton ionization coefficients have been measured (by photoconductivity detection) at 6943 Å and 3472 Å in NaCl, KCl, and KI, however, by Catalano et al.[48] and Dneprovskii et al.[49] Braunlich et al.[21] have used that data, along with the 1.064 μm avalanche ionization rate data (neglecting its

frequency dispersion) to investigate numerically the influence of multiphoton absorption on breakdown in NaCl at 6943 Å and 3472 Å (30 nsec FWHM pulse duration). They calculated, as a function of light intensity, the conduction electron density generated by pure avalanche ionization, by avalanche ionization with five-photon interband absorption, and by avalanche with five-photon absorption plus an F-center population. Their results showed that multiphoton absorption, both interband and via F-center levels, is more efficient at producing initial electrons at low field strengths than is avalanche ionization. They also showed that the avalanche ionization efficiency dominates the plasma generation for electric field strengths over about 1 MV/cm, regardless of the presence of the other multiphoton mechanisms. Our morphological data, at 1.064 μm [3] and 5321 Å (Fig. 5), indicates that the last statement is indeed true. At both of those wavelengths we observed the same morphology, even in KH_2PO_4 at 5321 Å where three-photon transitions are possible. At both wavelengths the morphology consisted of spatially distinct plasma sites separated irregularly by short (~1 μm) undamaged spaces. If strong multiphoton absorption were dominant in the breakdown process, one would expect to see, not spatially distinct plasma vestiges, but spatially <u>continuous</u> evidence of damage along the focal axis even at breakdown threshold. As Fig. 5 demonstrates, that is not the case. At 5321 Å, in materials with $\mathcal{E}_G > 7$ eV,

the character of intrinsic picosecond laser-induced breakdown is dominated by the familiar avalanche ionization mechanism. This situation is not expected[21,19] to persist for wavelengths much shorter than 5321 Å in our sample materials of band gap 7 to 12 eV.

Another recent theoretical analysis has been made by Sparks.[4,25] He included electron-photon-phonon transitions as a new mechanism for sustaining an avalanche, and he also included multiphoton absorption for initial electron generation. His theoretical threshold values for 10.6 μm, 1.06 μm, and 6943 Å laser-induced breakdown fall within the uncertainty limits of the experimental values. His calculations predicted a decrease in the NaCl threshold to be observed for wavelengths shorter than about 1.0 μm (for nanosecond pulses). Our picosecond pulse data do not follow that prediction. They do not show the predicted ~50% decrease of the threshold between 1.064 μm and 5321 Å. If NaCl behaves in a way similar to KH_2PO_4, our data suggest that a threshold decrease may be expected for wavelengths shorter than about $3hc/\mathcal{E}_G \simeq 4300$ Å. Several other points raised in Refs. 4 and 25 merit discussion. It was stated in these papers that the difference between early DC thresholds and those measured by Yablonovitch[9] was attributed to avalanche ionization frequency dependence, as embodied in Eq. 1. That assertion is incorrect. Yablonovitch[9] warned against such assignment of the systematic difference that

he found, and indicated that the more probable origin of that factor concerns details of the DC experiments. Others[19] have restated that point. Concerning the avalanche ionization frequency dependence as given by Eq. 1, both the present work and an earlier experiment[11] indicate that τ_c is of the order 2×10^{-16} sec, whereas the calculations of Sparks[25] predict that τ_c should be larger roughly by the factor 10. A final point concerns the initial density of electrons that may serve to launch an avalanche. It is stated by Sparks that because of insulator electrical conductivity and photoconductivity values, initial electron densities should be less than $\sim 10^4$ cm^{-3} and that densities as large as 10^{10} cm^{-3} are unreasonable. Yet direct experimental evidence of such large densities has been found in *picosecond* laser-induced breakdown morphology.[3] The resolution of this point lies in the fact that the photoconductivity measurements, to which Sparks alludes, must involve light intensities too weak to permit the ionization of color center traps by multiphoton absorption, and photon energy too small to allow single-photon ionization. Color center densities as low as 10^{11} cm^{-3} are difficult to detect by linear absorption spectrophotometry. It is therefore possible to have a clear NaCl sample which satisfies the insulator criterion (dc conductivity $\sigma \lesssim 10^{-20}$ ohm^{-1} cm^{-1}), yet simultaneously possesses 10^{11} cm^{-3} F-centers which may be ionized by 1.064 μm two-photon

absorption to produce breakdown morphology as observed in Ref. 3.

F. Acknowledgements

We thank Prof. J. H. Marburger of the University of Southern California for a helpful discussion concerning self-focusing. Dedicated sample preparation by Mr. S. Maurici is once again greatly appreciated.

REFERENCES

* A preliminary report of this work was presented at the IX International Conference on Quantum Electronics, Amsterdam, The Netherlands, June, 1976, Paper Q2.

Research supported in part by the National Aeronautics and Space Administration, by the Joint Services Electronics Program, and by the Advanced Research Projects Agency.

† Present address: Lawrence Livermore Laboratory, University of California, Livermore, California 94550.

‡ Present address: General Motors Research Laboratory, Warren, Michigan 48090.

1. W. Lee Smith, J. H. Bechtel, and N. Bloembergen, Phys. Rev. B12, 706 (1975).

2. W. Lee Smith and J. H. Bechtel, Appl. Phys. Lett. 28, 606 (1976).

3. W. Lee Smith, J. H. Bechtel, and N. Bloembergen, "Picosecond Laser-Induced Damage Morphology: Spatially Resolved Microscopic Plasma Sites," to be published in Opt. Commun. (1976).

4. M. Sparks, "Current Status of Electron-Avalanche-Breakdown Theories," in Laser Induced Damage in Optical Materials: 1975, Natl. Bur. Stds. Spec. Publ. No. 435 (U.S. GPO, Washington, D. C., 1976), p. 331.

5. A. Van Marum, Ann. Phys. (Leipz.) 1, 68 (1799).

6. A. von Hippel, Z. Physik 67, 707 (1931); J. Appl. Phys. 8, 815 (1937); Phys. Rev. 54, 1096 (1938).

7. H. Fröhlich, Proc. Roy. Soc. (London) 160, 230 (1937); see also Proc. Roy. Soc. (London) 188, 521 and 532 (1947) and references therein.

8. F. Seitz, Phys. Rev. 76, 1376 (1949); see also H. Callen, Phys. Rev. 76, 1394 (1949).

9. E. Yablonovitch, Appl. Phys. Lett. 19, 495 (1971).

10. D. Fradin, E. Yablonovitch, and M. Bass, Appl. Opt. 12, 700 (1973).

11. D. Fradin and M. Bass, Appl. Phys. Lett. 22, 206 (1973).

12. M. Bass and H. H. Barrett, Appl. Opt. 12, 690 (1973).

13. G. M. Zverev, T. N. Mikhailova, V. A. Pashkov, and N. M. Solov'eva, Zh. Eksp. Teor. Fiz. 53, 1849 (1967) [Sov. Phys. - JETP 26, 1053 (1968)].

14. G. M. Zverev, E. A. Levchuk, and E. K. Maldutis, Zh. Eksp. Teor. Fiz. 57, 730 (1969) [Sov. Phys. - JETP 30, 400 (1970)].

15. R. Yu. Orlov, I. B. Skidan, and L. S. Telegin, Zh. Eksp. Teor. Fiz. 61, 784 (1971) [Sov. Phys. - JETP 34, 418 (1972)].

16. S. A. Belozerov, G. M. Zverev, V. S. Naumov, and V. A. Pashkov, Zh. Eksp. Teor. Fiz. 62, 294 (1972) [Sov. Phys. - JETP 35, 158 (1972)].

17. V. A. Gridin, A. N. Petrovskii, and S. L. Pestmal, Kvant. Electr. 1, 2278 (1974) [Sov. J. Quant. Electr. 4, 1270 (1975)].

18. V. A. Gridin, V. A. Krotov, and A. N. Petrovskii, Kvant. Electr. 3, 311 (1976) [Sov. J. Quant. Electr. 6, 163 (1976)].

19. N. Bloembergen, IEEE J. Quant. Electr. QE-10, 375 (1974).

20. L. V. Keldysh, Zh. Eksp. Teor. Fiz. 47, 1945 (1964) [Sov. Phys. - JETP 20, 1307 (1965)]; see also S. S. Mitra, L. M. Narducci, R. A. Shatas, Y. F. Tsay, and A. Vaidyanathan, Appl. Opt. 14, 3038 (1975). Our calculations follow those of Mitra et al.

21. P. Braünlich, A. Schmid, and P. Kelly, Appl. Phys. Lett. 26, 150 (1975).

22. P. Kelly, P. Braünlich, and A. Schmid, Appl. Phys. Lett. 26, 223 (1975).

23. N. L. Boling, P. Braünlich, A. Schmid, and P. Kelly, Appl. Phys. Lett. 27, 191 (1975).

24. L. H. Holway and D. Fradin, J. Appl. Phys. 46, 279 (1975).

25. M. Sparks and C. J. Duthler, "Theoretical Studies of High-Power Ultraviolet and Infrared Materials" (Fifth Technical Report on Contract DAHC 15-73-C-0127, Xonics Corp., Van Nuys, CA 91406, 1975).

26. See p. xxvii of Ref. 4 for a full listing of Natl. Bur. Stds. Special Publications of Proceedings of Conferences on Laser-Induced Damage in Optical Materials, 1969-1975.

27. J. J. O'Dwyer, The Theory of Electrical Conduction and Breakdown in Solids and Dielectrics (Clarendon, Oxford, 1973).

28. J. H. Marburger, "Theory of Self-Focusing," in Progress in Quantum Electronics, edited by J. H. Sanders and S. Stenholm (Pergamon, Oxford, 1975), Vol. 4, Part 1, and references therein.

29. V. I. Talanov, Zh. Eksp. Teor. Fiz. 2, 218 (1965) [Sov. Phys. - JETP Lett. 2, 138 (1965)].

30. P. L. Kelley, Phys. Rev. Lett. 15, 1005 (1965).

31. G. M. Zverev and V. A. Pashkov, Zh. Eksp. Teor. Fiz. 57, 1128 (1969) [Sov. Phys. - JETP 30, 616 (1970)].

32. D. Fradin, IEEE J. Quant. Electr. QE-9, 954 (1973). Note that Eq. 2 in this reference should read $I_d = I_o(1-P/P_{cr})^{-1}$.

33. A. Feldman, D. Horowitz, and R. M. Waxler, IEEE J. Quant. Electr. QE-9, 1054 (1973).

34. P. D. Maker and R. W. Terhune, Phys. Rev. 137, A801 (1965).

35. A. Owyoung, IEEE J. Quant. Electr. QE-9, 1064 (1973).

36. M. D. Levenson, IEEE J. Quant. Electr. QE-10, 110 (1974); M. D. Levenson and N. Bloembergen, Phys. Rev. B10, 4447 (1974).

37. E. S. Bliss, D. R. Speck, and W. W. Simmons, Appl. Phys. Lett. 25, 728 (1974).

38. M. J. Moran, C-Y She, and R. L. Carman, IEEE J. Quant. Electr. QE-11, 259 (1975).

39. D. Milam and M. J. Weber, J. Appl. Phys. 47, 2497 (1976).

40. W. Lee Smith and J. H. Bechtel, J. Appl. Phys. 47, 1065 (1976); J. H. Bechtel and W. Lee Smith, Phys. Lett. 55A, 203 (1975).

41. K. Kato, IEEE J. Quant. Electr. QE-10, 616 (1974); see also the discussion of 90^o phase-matching in F. Zernike and

J. E. Midwinter, Applied Nonlinear Optics (J. Wiley, New York, 1973), Chap. 3.

42. W. Lee Smith, J. H. Bechtel and N. Bloembergen, in Laser-Induced Damage in Optical Materials: 1975, Natl. Bur. Stds. Spec. Pub. No. 435 (U.S. GPO, Washington, D. C., 1976), p. 321.

43. W. J. Deshotels. J. Opt. Soc. Am. 50, 865 (1960).

44. W. Lee Smith, J. H. Bechtel, and N. Bloembergen (unpublished).

45. D. R. White, E. L. Dawes, and J. H. Marburger, IEEE J. Quant. Electr. QE-6, 793 (1970).

46. D. W. Fradin, N. Bloembergen, and J. P. Letellier, Appl. Phys. Lett. 22, 635 (1973).

47. E. Yablonovitch and N. Bloembergen, Phys. Rev. Lett. 29, 907 (1972).

48. I. M. Catalano, A. Cingolani, and A. W. Minafra, Phys. Rev. B 5, 1629 (1972).

49. V. S. Dneprovskii, D. N. Klyshko, and A. N. Perrin, Zh. Eksp. Teor. Fiz. 3, 385 (1966) [Sov. Phys.-JETP Lett. 3, 251 (1966)].

CHAPTER V.

STUDY OF PICOSECOND LASER-INDUCED BREAKDOWN AT 3547 Å

A. Introduction

This chapter relates our effort to accurately measure breakdown thresholds in a series of materials using 3547 Å picosecond laser pulses. In order to investigate the widest possible range of material band gap, the series of materials included as many as possible of the materials tested at 1.064 μm and 5321 Å (Chapters III and IV of this dissertation): LiF, NaF, CaF_2, SiO_2, and KH_2PO_4 (KDP). These materials cover a band gap range of about 12.0 to 6.9 eV and, with a 3547 Å photon energy of 3.50 eV, present the opportunity to study dielectric breakdown assisted by multiphoton transitions of various order, all the way down to two-photon absorption in KH_2PO_4. Results from this study have provided qualitative verification and extension of the documentation of frequency dependent breakdown behavior, as first described in Chapter IV.

Section B of this chapter describes the experimental equipment, procedure, and difficulties. The results are presented in Section C and discussed in Section D.

B. Experiment

1. Apparatus

The components of the experimental apparatus are

illustrated in Fig. V.1. The optical input to that series of components is the single, 1.064 μm, nominally 30 psec, laser pulse from the laser system described in Chapter II of this dissertation. The characterization and frequency conversion of this infrared pulse is begun with the components within the dashed line. The potassium dihydrogen phosphate (KDP) crystal HG1 and vacuum photodiode detectors D1 and D2 yield the two energy signals required for the pulse duration measurement by the τA technique, as described fully in Appendix II. The infrared pulse is next frequency-doubled in a second-harmonic generation cell HG2 containing a cesium dihydrogen arsenate (CDA) crystal. This crystal is electronically maintained at a temperature of 42 °C, which is the temperature that noncritically phase-matches the oriented CDA crystal. The benefits of noncritical phase-matching[1] are the absence of deleterious walk-off[2] effects due to double refraction, a relatively large acceptance angle of input beam divergence, and stability of Gaussian spatial profile for an unlimited period of time. These properties, not obtainable with the more familiar angle-tuned KDP doubling crystal, are essential for the production of precisely known, optical electric field distributions. The conversion efficiency for second-harmonic generation is monitored with the filtered detector D3. The limit to the amount of 3547 Å light that we may produce with this equipment is set by the damage threshold of the CDA

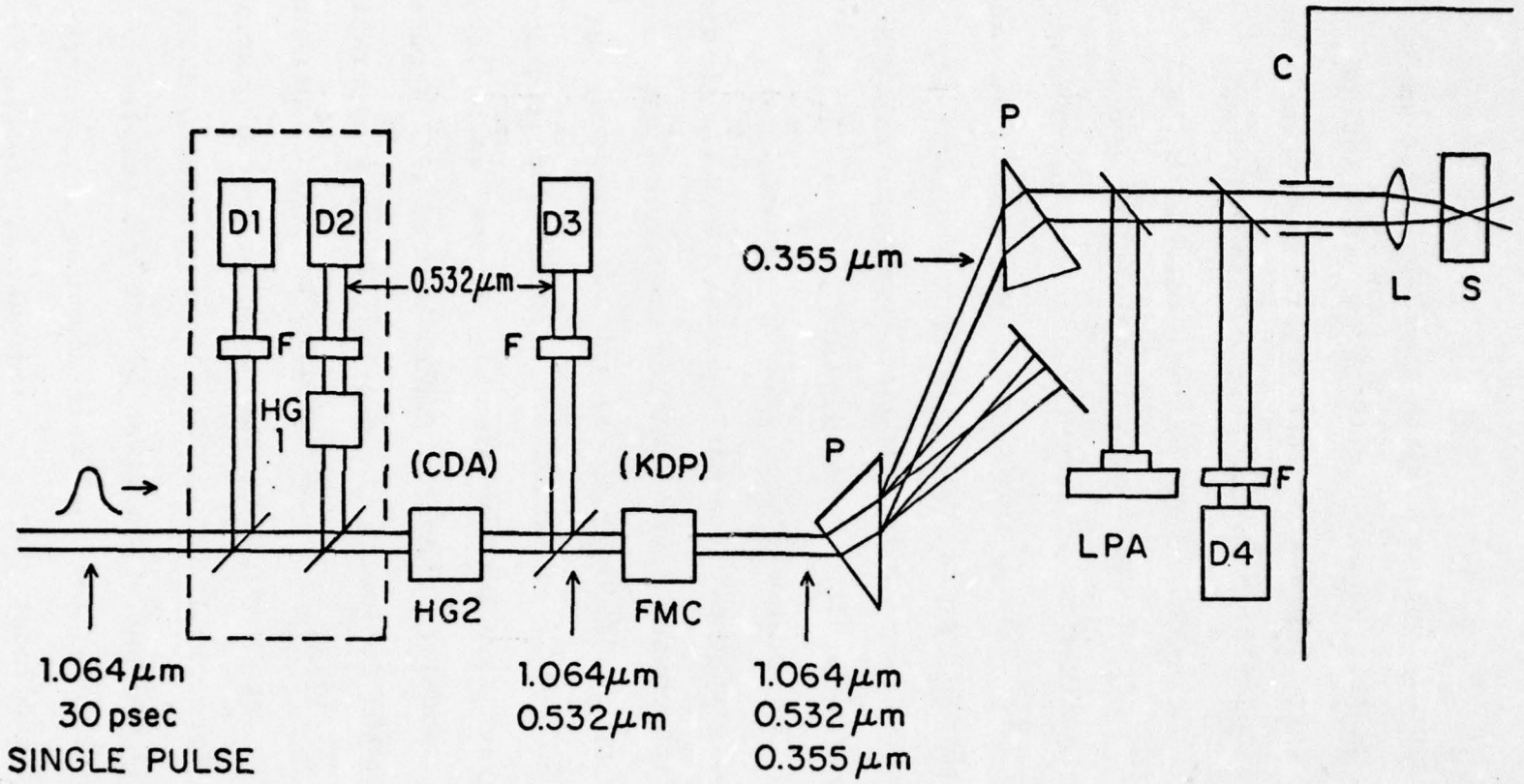

Fig. V.1 Diagram of the experimental apparatus. Notation: D1-D4, biplanar photodiode detectors; F, appropriate filters; HG1, KH_2PO_4 frequency doubling crystal; HG2, CsH_2AsO_4 frequency doubling crystal; FMC, KH_2PO_4 crystal for 3547 Å generation; P, prism; LPA, Reticon linear photodiode array; C, curtain; L, SiO_2 lens; S, dielectric sample.

material. At the conservative maximum incident 1.064 μm irradiance level we have used (~3 x 10^9 W/cm^2 with 100 MW single pulse power), the power conversion efficiency was ~50%.

The 1.064 μm and 5321 Å pulses exit collinearly from the CDA cell into the final frequency mixing crystal (FMC). In this crystal the orthogonally polarized infrared and second-harmonic pulses are mixed to produce light at the third-harmonic wavelength of 3547 Å. This frequency tripling crystal is made of KDP and is phase-matched by angle-tuning. Unfortunately, no material is available with the proper temperature behavior of refractive indices (ordinary and extraordinary) to allow temperature-tuned, 90° phase-matched frequency summing at these two input wavelengths. The maximum power we have obtained at 3547 Å, under the conservative limiting conditions mentioned above, is about 8 MW for a power conversion efficiency of ~8% from 1.064 μm to 3547 Å. Conversion efficiencies for frequency tripling of up to 30% have been obtained by others[3] using longer crystals. Further detailed characteristics of the 3547 Å pulse will be related in the following paragraphs. Spatial separation of the three output pulses from the tripling crystal is performed by quartz prism P. The UV pulse is then sampled by two quartz beam splitters, before passing through a light-shielding curtain and into the damage chamber. The first of the two samples is directed onto a commercial Reticon[4] self-scanning linear array of 256 miniature photodiodes (LPA). The diodes are spaced by

0.05 mm, and are incorporated onto an integrated circuit chip. This device, coupled to an oscilloscope, displays the spatial energy profile of the impinging light pulse. With it, we are able to measure the area of the 3547 Å pulse and check its spatial profile quality. Further mention of its use will be made below. The second sample of the main pulse enters a calibrated photodiode D4, in order to provide a measure of the UV pulse energy just before it enters the lens. The characterized UV pulse finally is tightly focused by a quartz lens (L) into the dielectric sample (S) under investigation. The sample is held in a three-dimensional translation holder so that the pulse may be directed through any volume element of the sample.

In Chapter II of this work, it was made clear that three pulse parameters must be carefully measured to allow the accurate determination of the electric field distribution of the optical pulse. The sufficiency of these three parameters - the spatial profile radius ρ, the temporal half-duration τ, and the total pulse energy $\mathcal{E}$ - is based on the assumption that the pulse spatial and temporal functional form is unchanging. We will now consider the degree to which the characteristics of our 3547 Å pulses allow us to determine the field distribution in this experiment.

The third-harmonic pulse energy ($\mathcal{E}_{TH}$) measurement is straightforward, as it was in the previous 1.064 μm and 5321 Å

experiments. The detector D4 in Fig. V.1 was calibrated again with two Eppley Laboratory[5] thermopiles, which were themselves calibrated with National Bureau of Standards spectral sources. Again, the detector area is large enough and the detector-oscilloscope response time is long enough that true spatial and temporal integration is performed over the pulse waveform by the detector. Our calibration method yields pulse energy measurements with an estimated accuracy of better than ±10%.

The temporal waveform of the 3547 Å pulse is closely Gaussian for small conversion efficiencies in both the doubling and mixing crystals. In that case, the average duration of the UV pulse will be $1/\sqrt{3}$ of the 30 psec 1.064 μm parent pulse duration (or 17 psec). This $1/\sqrt{3}$ degree of pulse shortening has been roughly confirmed experimentally with streak camera photography.[3] As the conversion efficiency increases, preferential saturation of the doubling and mixing processes at the temporal peak region of the pulse results in an effective lengthening of the duration. The saturation results simultaneously in an effective broadening[6] of the pulse area as the pulse becomes more square in profile. Fortunately, our experimental procedure - specifically the τA technique (Appendix II) - allows us to incorporate these broadening factors into our data analysis. In the low conversion regime, it is easily shown that the ratio $\sqrt{\mathcal{E}_f^3 / \mathcal{E}_{TH}}$ of the fundamental (f) and third-

harmonic (TH) pulse energies is directly proportional to the third-harmonic pulse area A and half-duration τ and is independent of the pulse intensity. For data in the low conversion regime, we may normalize the individual pulse $\sqrt{\mathcal{E}_f^3 / \mathcal{E}_{TH}}$ signals to a product of a half-duration τ of 17 psec and the actual pulse area as measured with the photodiode array. Then for the remaining data points in the higher power range, the signals will become progressively larger and will properly take into account the broadening of the duration and area.

We have discussed the energy and pulse duration measurements and the minor saturation broadening of the pulse area, $\pi\rho^2$. It remains to consider the distortions in the pulse spatial profile which are due to walk-off and self-focusing in the KDP mixing crystal. Fig. V.2 illustrates the typical spatial distribution of energy that we obtained in a 3547 Å pulse. Walk-off[7] is the term which describes the decrease in overlap, proportional to the distance traveled inside the nonlinear crystal, between the nonlinear polarization wave and the generated light wave. Walk-off is caused by crystal birefrigence, and it results in a cylindrically asymmetric, distorted spatial waveform for the 3547 Å pulse. The poor spatial profile exhibited in Fig. V.2a is the result in the plane most severely affected. Fig. V.2b shows the distortion which occurs in the plane normal to that of Fig. V.2a. One observes in these photographs the departure of our spatial profile from a

(a)

(b)

Fig. V.2 Oscillographs of the spatial energy distribution of the 3547 Å optical pulse. Figures (a) and (b) are taken in the orthogonal planes of most and least influence from walk-off, resp.

Gaussian form.

Nevertheless, the input area of the UV pulse of Fig. V.2 must be estimated by fitting to it a Gaussian curve, as shown in Fig. V.3. The input profile radius ρ (0.81 mm) obtained from the dotted Gaussian curves of Fig. V.3 yields (with Eq. 3 of Chapter III, Part A) a focal area A ($=\pi w^2$) of 5.6 μm^2. If the laser profiles of Fig. V.3 fit the dotted Gaussian curves perfectly, the uncertainty in A would be less than ±20%, as was the case in the experiments at 1.064 μm (see Fig. 2, Part A of Chapter III). The actual fit of the profile in Fig. V.2b is acceptable, but because of the modulation evident in Fig. V.2a, the fit there is poor and leads to additional uncertainty in the focal plane area. Since the lens essentially performs a Fourier transformation, the abrupt transverse intensity variations (high spatial-frequency modulation) of the input pulse result in a deconcentration of the energy distribution in the focal plane which is not taken into account by the Gaussian beam propagation equations used above to arrive at the area of 5.6 μm^2. Rough estimation indicates that the actual effective area might be as much as a factor two larger than the 5.6 μm^2 value obtained by Gaussian approximation.

If the laser spatial profile were constant from pulse to pulse over the period of time necessary for an experiment to be performed, the scanning aperture technique (Chapter III, Part A) could be used to measure the effective area in the

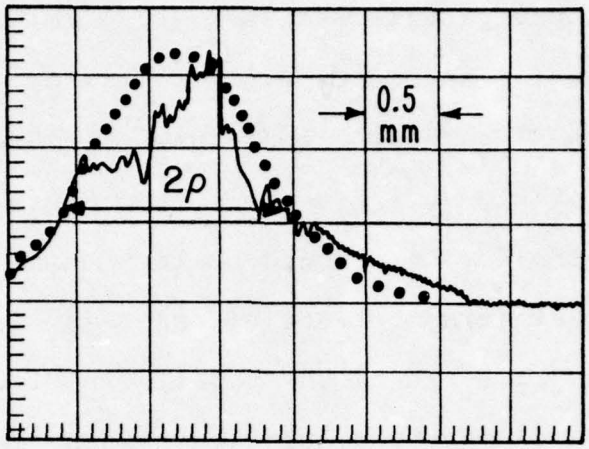

(a)

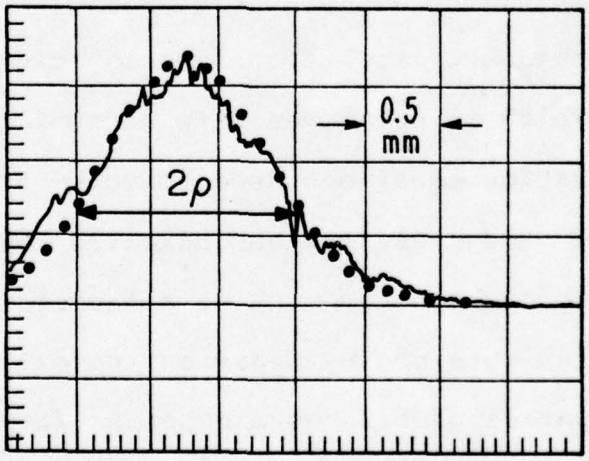

(b)

Fig. V.3 Illustration of the approximate fit of a Gaussian curve to the laser pulse spatial profile. The profile radius ρ is used to compute the area of the pulse in the focal plane of a lens.

focal plane. That avenue of relief was blocked in this experiment by the last distortions which must be mentioned and which are both time- and power-dependent. Over a period of a few (~3 to 5) minutes, minute movements in the optical table resulted in variations in the KDP phase-matching angle, and the large-scale fringe structure in Fig. V.2 wandered correspondingly.

At high power levels self-focusing of the 3547 Å pulse in the KDP crystal and in the subsequent quartz elements significantly enhances the noise structure produced by the phase-matching conditions. Such self-focusing, which grows from small-scale spatial hot spots on a pulse, is known as "small-scale self-focusing".[8] This latter spatial instability is to be distinguished from the "whole-beam" or "large-scale" self-focusing which was discussed in the breakdown experiments of Chapters III and IV. Enhancement of the hot spots on the pulse by self-focusing was easily observed by removing the sample (see Fig. V.1) and displaying the diverging 3547 Å light on a fluorescent card (or bleached paper). The strong power dependence of the enhancement was clearly observable. Hot spot enhancement by self-focusing was observed to occur for input power levels over roughly 150 kW, and was present in the breakdown tests of all materials except CaF_2. This effect results in different, uncalculable reductions in the effective focal area for materials which undergo breakdown

at different power levels. The influence of this effect is in opposite direction to the enlargement of the focal area, mentioned earlier, caused by the Fourier transform of high spatial-frequency components on the input pulse. Therefore the true effective focal area for CaF_2 is probably nearer the 11.2 μm^2 estimation than the 5.6 μm^2 value, but for materials with increasingly higher threshold power, the probable effective area is reduced to values closer to 5.6 μm^2 and perhaps less by hot spot enhancement. This material dependent effective area makes difficult the extraction and substantiation of even relative breakdown thresholds.

The conclusion of this section is that the best 3547 Å pulse that could be produced was decidedly less suitable for absolute electric field measurements than the 1.064 μm and 5321 Å pulses used in previous experiments. Aside from any consideration of whole-beam self-focusing, the spatial degradations mentioned above impose an uncertainty on the focal point power per unit area of roughly 100%. Repercussions of this uncertainty will be discussed in Section C of this chapter.

2. Procedure

The procedure for this experiment is identical to that of the 5321 Å experiment as related in Chapter IV (pages IV-20 to IV-23) and the reader is referred to those pages. One of the six materials studied at 5321 Å, NaCl, was eliminated from the 3547 Å experiment because of distortion by surface

polishing scratches. Due to the magnitude of the breakdown input power relative to the self-focusing critical power, data in this experiment was taken only with our shortest focal length (0.5 in.) lens.

C. Results

The data from this experiment are listed in Table V.1. The five tested materials are KH_2PO_4 (KDP), fused SiO_2, CaF_2, NaF, and LiF. These five materials were studied at the two previous frequencies of 1.064 μm and 5321 Å. The linear refractive indices n_o at 3547 Å are listed in column 2. Columns 3 and 4 tabulate the "paraxial" critical power P_1 and the "catastrophic" critical power P_2, calculated using the nonlinear refractive index (n_2) values listed in Table 1 of Chapter IV (page IV-26). These quantities were introduced and discussed at length in Chapter IV. The quantity P_1 equals $c\lambda^2 / 32\pi^2 n_2$, where c is the vacuum speed of light and λ is the light wavelength in air. P_2 is equal to 3.7 P_1. Because of the λ^2 dependence of P_1 and P_2, the 3547 Å critical power values in Table V.1 are smaller than the corresponding entries in Table 1 of Chapter IV by a factor of 9/4. In column 5 the measured values of the pulse input power at the breakdown threshold are listed, and columns 6 and 7 tabulate the fractional quantities P/P_1 and P/P_2.

As derived in Chapter IV (see Eq. 6) the breakdown

TABLE V.1

3547 Å Breakdown Data

Material	n_o	P_1 (kW)	P_2 (kW)	P (kW)	P/P_1	P/P_2	$\phi(P)$	E_B^{uv} (MV/cm)	E_B^{uv}/E_B^g
KH_2PO_4	1.4860	119	439	242	2.03	0.55	2.5-3.7	35-77	1.5-3.3
SiO_2	1.4762	125	462	170	1.36	0.37	2.0-3.0	25-49	1.3-2.6
CaF_2	1.4463	105	390	73	0.69	0.19	1.0-1.5	18-33	0.7-1.3
NaF	1.3359	126	465	271	2.15	0.58	2.5-3.7	40-99	2.1-5.1
LiF	1.4024	129	477	245	1.90	0.51	2.5-3.7	35-70	1.3-2.6

threshold electric field E_B may be obtained from the threshold power P with the relation

$$E_B = \left[\frac{1}{n_o \varepsilon_o c} \frac{P}{A} \frac{1}{1 - \frac{P}{\phi(P) P_1}} \right]^{1/2} . \qquad (1)$$

All the quantities in Eq. 1 have been defined in this chapter except ε_o, the permittivity of free space, and $\phi(P)$, the self-focusing function introduced in Chapter V. To recapitulate, the known limits of $\phi(P)$ are $\phi(P) \to 1$ for $P << P_1$ and $\phi(P) \to 3.7$ for $P \lesssim P_2$. Between these two limits $\phi(P)$ is presently unknown.

The obstacles to the interpretation and extraction of a breakdown threshold electric field from the data of Table 1 are two-fold. One of them has already been mentioned and it is the substantially non-Gaussian and unavoidably poor spatial character of the 3547 Å pulse due to the details of the final frequency mixing process and self-focusing. The specific result of the propagation of that distortion into the focal plane is that the intensity distribution there is irregular with an effective area A known only to within a factor 2. The probable effective area varies with input power, as well.

The other obstacle is the magnitude of the breakdown threshold power P relative to P_1 and P_2. As the entries in columns 6 and 7 show, the P values fit neither of the two limits mentioned above. The CaF_2 input power more closely fits the $P << P_1$ limit,

while the other input powers more closely approach the $P \lesssim P_2$ limit. It is therefore necessary to consider different ranges of the $\phi(P)$ function for the different materials, in order to deduce realistic upper and lower bounds for E_B from Eq. 1. Column 8 of Table V.1 lists the considered ranges of $\phi(P)$. In comparison to the large uncertainties introduced by the area A (5.6 to 11.2 μm^2) and by $\phi(P)$ in Eq. 1, the small (±10%) uncertainty in the input power P is immaterial and therefore neglected.

The next to the last column of Table V.1 lists the 3547 Å breakdown threshold (E_B^{uv}) results obtained in this experiment. The stated range in E_B^{uv} results from the uncertainties in A and $\phi(P)$. The lower and upper limits of E_B^{uv} for each material were obtained with the use of the upper and lower, respectively, limits of A and $\phi(P)$. The range of E_B^{uv} for a given material in column 9 constitutes an uncertainty of ~±35% about the average of the upper and lower limits. The reason the data were not displayed in that manner is that the power- (and thus material-) dependent hot spot behavior points to different probable location of the true threshold within that ±35% range for the different materials. For example, for CaF_2 the true threshold is closer to 18 MV/cm than 33 MV/cm, due to the small P/P_1 factor and the resulting absence of hot spot enhancement. But for LiF, the true E_B^{uv} may be nearer 70 MV/cm than 35 MV/cm.

In order to find whether interesting frequency dependent behavior is resolvable in this data, in Fig. V.4 we plot the

ratio E_B^{uv} / E_B^g (or rather the range thereof) versus material band gap. The 5321 Å thresholds (E_B^g) are taken from Table II of Chapter IV. Here we ignore the common effect of the small pulse duration difference (nominally 17 psec at 3547 Å versus 21 psec at 5321 Å) on the threshold ratio.

The relative and absolute positions of the data bars for CaF_2 and LiF seem reasonable, in view of the similar data of Chapter IV (Fig. 7). We also observe an absolute increase in the NaF threshold, as expected. Yet the reason for relative magnitudes of the NaF and LiF thresholds is not known, unless it is the simple manifestation of the large experimental uncertainties. The observation that the E_B^{uv} / E_B^g values for KH_2PO_4 and SiO_2 in Fig. V.4 are as large or larger than that for LiF can be explained, however. In Fig. 7 of Chapter IV, the interpretation was advanced that the marginal onset of three-photon absorption (3PA) lowered the KH_2PO_4 threshold at 5321 Å relative to that at 1.064 μm. If we apply that observation to the present 3547 Å experiment, we conclude that the 3PA might serve to lower the thresholds for materials with band gap less than 10.5 eV. CaF_2 has a band gap of 10 eV and indeed in Fig. V.4 one observes that the threshold ratio bar for CaF_2 allows the possibility that the 3547 Å threshold is less than the 5321 Å threshold. For SiO_2, 3PA would be considerably stronger due to its band gap value of about 8.0 eV. It is expected that strong 3PA caused beam depletion along the focal

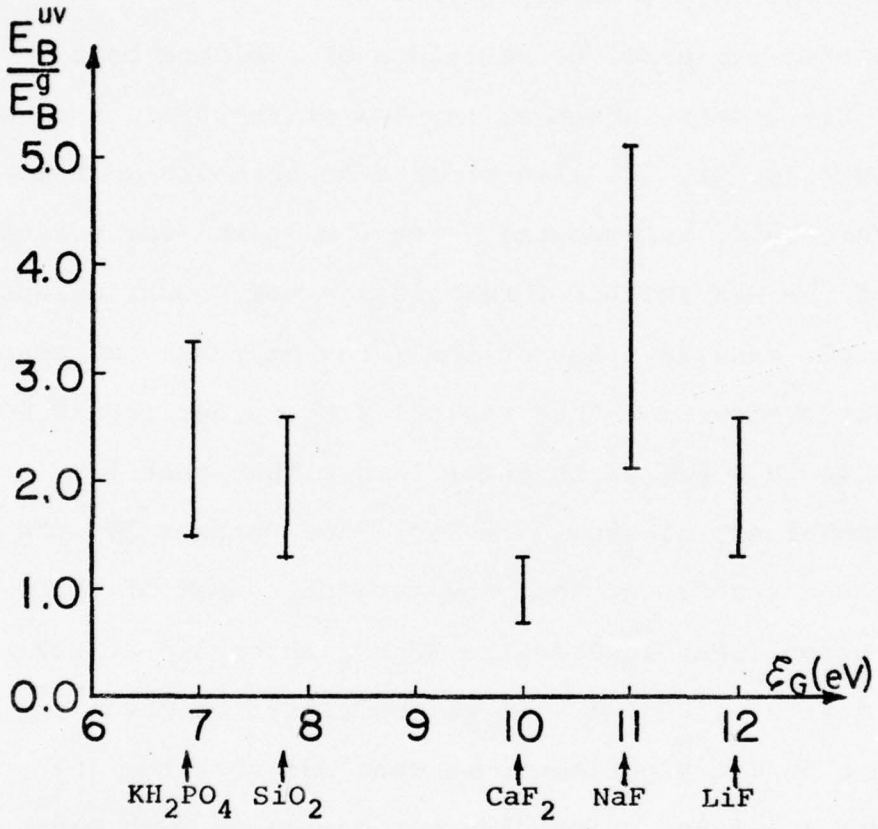

Fig. V.4 Illustration of the band gap ($\mathcal{E}_G$) dependent behavior of the threshold ratio E_B^{uv}/E_B^g observed in the present experiment. E_B^{uv} and E_B^g are the 3547 Å and 5321 Å thresholds, resp., as tabulated in Table V.1. The origins of the uncertainty in the data are discussed in the text.

axis in the SiO_2 sample and thus caused the E_B^{uv} / E_B^g value exceeding unity in Fig. V.4. A similar explanation may be advanced for the even larger E_B^{uv} / E_B^g values observed for KH_2PO_4. For that material, <u>two</u>-photon absorption is energetically allowed at 3547 Å, and beam depletion before the focal point would be more severe.

D. <u>Discussion</u>

We see that the data of Fig. V.4 is in large both explicable and reasonable in light of the earlier data obtained at the wavelengths of 1.064 μm and 5321 Å and displayed in Fig. 7 of Chapter IV. Although the uncertainties introduced by pulse distortion did not allow the determination of precise breakdown thresholds at 3547 Å, the frequency-dependent behavior observed first at 5321 Å was verified and extended qualitatively. Larger thresholds were found at 3547 Å, than at 5321 Å or 1.064 μm, for materials which do not permit two- or three-photon interband absorption to occur at 3547 Å. For one material, CaF_2, which supports weak three-photon absorption at 3547 Å, a decrease in the 3547 Å threshold, compared to its 5321 Å threshold, was found. This threshold behavior at 3547 Å in CaF_2 corresponds energetically to that found in KH_2PO_4 as the light frequency was doubled to 5321 Å in the prior investigation. At 3547 Å, for materials (KH_2PO_4 and SiO_2) with optical band gap smaller than that of CaF_2, an increase in the threshold input power

was also observed. However, those increases were interpretable as arising from depletion of the laser pulse, by strong two- or three-photon absorption, as it passed through the sample toward the focal region.

The indications of strong multiphoton absorption in KH_2PO_4 and SiO_2 suggest that if the breakdown experiment had been conducted on the sample surface rather than in the bulk, large decreases in the thresholds might have been observed at 3547 Å. The study of breakdown on surfaces would alleviate two difficulties which complicated the study described in this chapter - self-focusing in the sample and multiphoton absorption pulse depletion in the sample. Because of the wavelength dependence of these two factors, surface breakdown study will be increasingly attractive for wavelengths below 3547 Å. The use of 2661 Å fourth-harmonic light, generated entirely with 90° phase-matched materials (CDA and ADP), for such a study would remove walk-off distortion, as well. The benefits of surface breakdown study in the ultraviolet spectral region will be offset somewhat by other well-known problems associated with surface breakdown. Those problems originate with surface impurities and imperfections.[9] Because they generally introduce threshold electric field uncertainties of about a factor 2, the surface quality problems will require serious attention and solution if accurate and reproducible thresholds are to be obtained.

The main conclusion of this chapter is that the breakdown threshold does increase with light frequency, as predicted by the avalanche ionization model, up to the frequency where three-photon absorption may take place. Beyond that frequency, the assistance of the essentially instantaneous multiphoton absorption transitions dominates the avalanche ionization frequency trend, with the result that the breakdown threshold is reduced. It can now be said that the experimental study of laser-induced breakdown has been extended to the quantum regime, and that the predicted[10] behavior of the breakdown threshold has been observed.

REFERENCES

1. A discussion of the characteristics of angle- and temperature-tuned phase-matching is found in Applied Nonlinear Optics, F. Zernike and J. E. Midwinter (Wiley, New York, 1973), Chap. 3.

2. G. D. Boyd, A. Ashkin, J. M. Dziedzic, and D. A. Kleinman, Phys. Rev. 137, A1305 (1965).

3. D. T. Attwood, E. L. Pierce, and L. W. Coleman, Opt. Comm. 15, 10 (1975).

4. Reticon Corp., Sunnyvale, Calif.

5. The Eppley Laboratory, Newport, R. I.

6. D. R. White, E. L. Dawes, and J. H. Marburger, IEEE J. Quant. Electr. QE-6, 793 (1970).

7. The phenomenon of walk-off was originally termed the "aperture effect" by early authors: D. A. Kleinman, Phys. Rev. 128, 1761 (1962).

8. E. S. Bliss, D. R. Speck, J. F. Holzrichter, J. H. Erkkila, and A. J. Glass, Appl. Phys. Lett. 25, 448 (1974); also, laser frequency doubling in the presence of small-scale beam breakup has been investigated by D. T. Attwood, E. S. Bliss, E. L. Pierce, and L. W. Coleman, to be published in IEEE J. Quant. Electr.

9. N. Bloembergen, Appl. Opt. 12, 661 (1973).

10. N. Bloembergen, IEEE J. Quant. Electr. QE-10, 375 (1974).

Appendix I

Two-photon Fluorescence in Attenuating Media and Laser Pulse Duration Measurements

Two-photon fluorescence in attenuating media and laser pulse duration measurements*

J. H. Bechtel and W. L. Smith

Gordon McKay Laboratory, Harvard University, Cambridge, Massachusetts 02138
(Received 16 April 1975; in final form 1 August 1975)

Analytical and numerical results are obtained for two-photon fluorescence in an attenuating medium. Cases of one- and/or two-photon attenuation are considered. These results are interpreted with respect to the measurement of ultrashort laser pulses.

PACS numbers: 42.65.D, 42.60.N

The method of two-photon fluorescence (TPF) has been widely used to measure the duration of ultrashort light pulses produced by mode-locked lasers.[1] In general, if two oppositely directed pulses of equal duration overlap each other in a two-photon absorbing medium, then the spatial distribution of the fluorescence decay may be used to infer the duration of the pulse. A typical experimental arrangement for measuring the pulse length is exhibited in Fig. 1.

For simplicity we will assume that the laser pulse has a uniform spatial profile and that there is total spatial overlap of the two oppositely directed pulses when they intersect each other in the center of the cell. If the total time integrated fluorescence at a position z is denoted by $S(z)$, then

$$S(z) \propto \int_{-\infty}^{\infty} I_1^2(t - z/v)\,dt + \int_{-\infty}^{\infty} I_2^2(t + z/v)\,dt + 4\int_{-\infty}^{\infty} I_1(t - z/v) I_2(t + z/v)\,dt, \tag{1}$$

where I_1 and I_2 are the irradiances of the two pulses. The position $z = 0$ corresponds to the position of complete overlap of the two oppositely directed pulses, and v is the group velocity of the pulse in the fluorescent medium.

For the case of equal intensities and no attenuation of the pulses due to either scattering or one- or two-photon absorption, Eq. (1) reduces to

$$S(z) \propto 1 + 2G^{(2)}(2z/v)[G^{(2)}(0)]^{-1}, \tag{2}$$

where

$$G^{(2)}(x) = \int_{-\infty}^{\infty} I(t - x) I(t)\,dt.$$

This result has been obtained previously[2] and implies a contrast ratio $K = S(0)/S(\infty) = 3$. We wish to note, however, that contrast ratios less than 3 will be obtained if the pulses have unequal irradiances. Moreover, the spatial distribution of the TPF decay will also be different if there is pulse attenuation in the TPF cell.

For the case of TPF in a cell of length $2d$ and with significant beam attenuation via one-photon absorption or scattering, Eq. (1) becomes

$$S(z) \propto (\tfrac{1}{2}\pi)^{1/2}\tau I_{10}^2\{\exp[-2\alpha(d + z)] + \theta^2 \exp[-2\alpha(d - z)] + 4\theta \exp[-2\alpha d - 2z^2/(\tau^2 v^2)]\}. \tag{3}$$

Here I_{10} is the irradiance at $z = -d$ and I_{20} is the irradiance at $z = d$. The one-photon attenuation coefficient is α, τ is the $1/e$ pulse half-width of the assumed temporally Gaussian pulse, and θ is equal to I_{20}/I_{10}.

If $I_{10} = I_{20} = I_0$, the result becomes

$$S(z) \propto 2(\tfrac{1}{2}\pi)^{1/2}\tau I_0^2 \exp(-2\alpha d) \times\{\cosh(2\alpha z) + 2\exp[-2z^2/(\tau^2 v^2)]\}. \tag{4}$$

The results of Eq. (3) are presented in Fig. 2 for several values of θ and α.

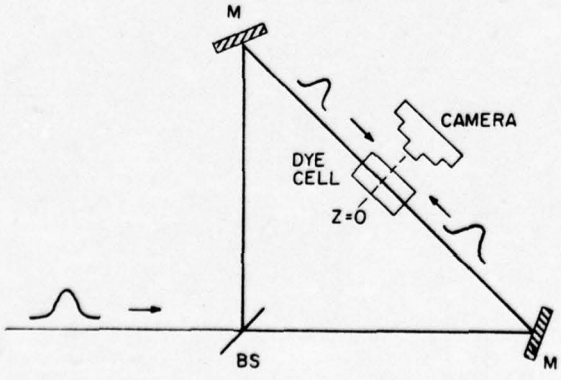

FIG. 1. Schematic diagram of the TPF experiment. M, mirror; BS, beam splitter.

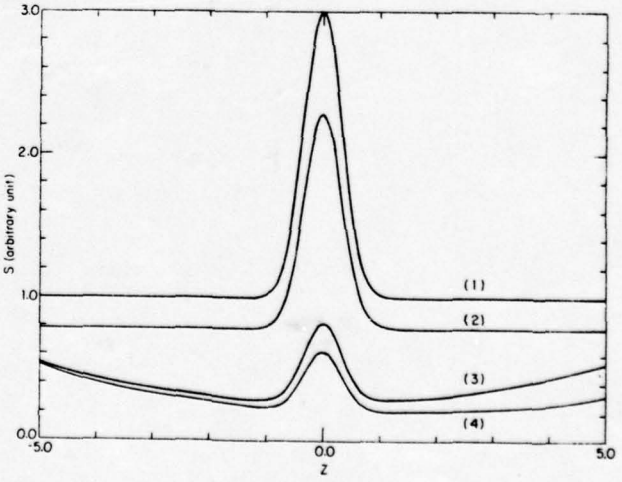

FIG. 2. Plot of two-photon fluorescence intensity S (in arbitrary units) versus z. The total TPF cell length is 10.0 cm. The pulse duration full width at half-maximum is 30 psec. Curve (1) $\alpha = 0$, $\theta = 1.0$; curve (2) $\alpha = 0$, $\theta = 0.75$; curve (3) $\alpha = 0.13$ cm^{-1}, $\theta = 1.0$; and curve (4) $\alpha = 0.13$ cm^{-1}, $\theta = 0.75$.

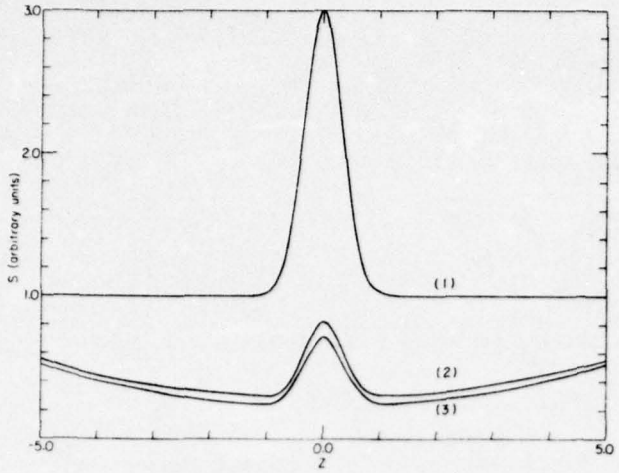

FIG. 3. Plot of two-photon fluorescence intensity S (in arbitrary units) versus z. The total TPF cell length is 10.0 cm, and the maximum irradiance is 3 GW/cm^2. The pulse duration full width at half-maximum is 30 psec. Curve (1) $\alpha = 0$, $\theta = 1.0$, $\beta = 0$; curve (2) $\alpha = 0.13$ cm^{-1}, $\theta = 1.0$, $\beta = 0$; and curve (3) $\alpha = 0.13$ cm^{-1}, $\theta = 1.0$, $\beta = 8.4 \times 10^{-12}$ cm/W.

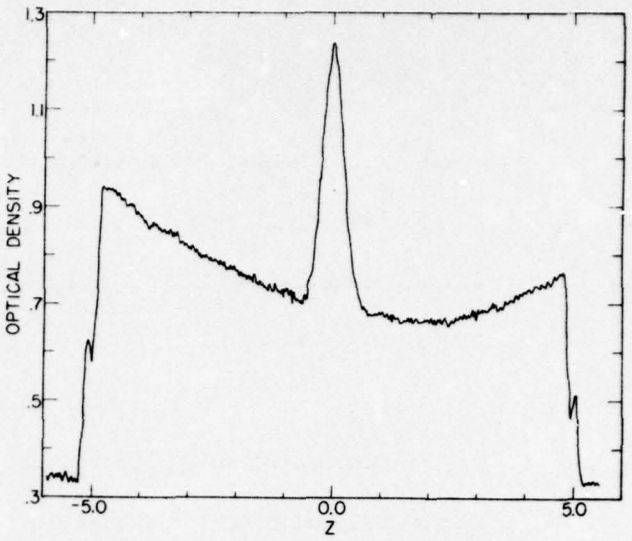

FIG. 4. Densitometer trace of two-photon fluorescence produced optical density versus z. This trace results from a single laser pulse extracted from a Nd:YAG mode-locked laser. The TPF medium is a 10^{-2} solution of Rhodamine 6G in ethanol placed in a 10-cm-long dye cell.

If both one-photon attenuation and two-photon attenuation are significant, the results become somewhat more complex. For the case of a spatially uniform but temporally Gaussian pulse the irradiances are given by the expressions

$$I_1(t - z/v) = I_{10} \exp\left(-\frac{(t - z/v)^2}{\tau^2}\right) \exp[-\alpha(d + z)] \times \left[1 + \left(\frac{\beta}{\alpha}\right) I_{10} \exp\left(-\frac{(t - z/v)^2}{\tau^2}\right) \times \{1 - \exp[-\alpha(d + z)]\}\right]^{-1},$$

and

$$I_2(t + z/v) = I_{20} \exp\left(-\frac{(t + z/v)^2}{\tau^2}\right) \exp[-\alpha(d - z)] \times \left[1 + \left(\frac{\beta}{\alpha}\right) I_{20} \exp\left(-\frac{(t + z/v)^2}{\tau^2}\right) \times \{1 - \exp[-\alpha(d - z)]\}\right]^{-1}.$$

Here β is the two-photon attenuation coefficient and is related to the two-photon absorption cross section $\sigma^{(2)}$, the number of two-photon absorbing molecules per unit volume n, and the photon energy $\hbar\omega$ by the expression

$$\beta = \sigma^{(2)} n / \hbar\omega.$$

If the two-photon absorption cross section has units cm^{-3}, and $\hbar\omega$ is expressed in Joules, then β is expressed in cm/W.

No simple analytic expression may be obtained from Eq. (1) in this case, but numerical results are presented in Fig. 3 for several examples. The numerical example for $\alpha \neq 0$ and $\beta \neq 0$ corresponds to a 10^{-2} M solution of Rhodamine 6G in ethanol for a laser wavelength of 1.06 μm. The incident laser pulse is assumed to be temporally Gaussian with a pulse duration of 30 psec full width at half-maximum; the maximum irradiance is 3 GW/cm^2. For this example $\alpha = 0.13$ cm^{-1} and $\beta = 8.4 \times 10^{-12}$ cm/W.[3]

From Figs. 2 and 3 we observe that if there is significant attenuation of the pulses in passing through the TPF cell by one-photon absorption and/or two-photon absorption, then the spatial dependence of the TPF profile may change significantly from the results predicted assuming no depletion of the oppositely directed laser pulses. It is evident from these figures that one must use care in interpreting contrast ratios derived from these figures.

Finally, we note that we have performed several experiments using single pulses produced by a mode-locked Nd:YAG laser to observe TPF. These experiments clearly show that there is significant attenuation of the laser pulse as it passes through the dye cell. A typical densitometer trace is exhibited in Fig. 4. The asymmetry of the trace is produced by the inequality of the intensities of the two oppositely directed pulses in this experiment. Our experimental results are in reasonable quantitative agreement with the theoretical description presented here.

*Supported in part by the National Aeronautics and Space Administration.

[1]D. J. Bradley and G. H. C. New, Proc. IEEE 62, 313 (1974).
[2]D. von der Linde, IEEE J. Quantum Electron. QE-8, 328 (1972).
[3]J. P. Hermann and J. Ducuing, Opt. Commun. 6, 101 (1972).

Appendix II

A Simple Technique for Individual Picosecond Laser Pulse Duration Measurements

A simple technique for individual picosecond laser pulse duration measurements*

W. L. Smith and J. H. Bechtel

Gordon McKay Laboratory, Harvard University, Cambridge, Massachusetts 02138
(Received 9 May 1975; in final form 20 August 1975)

We describe here a simple nonlinear optic technique for the measurement of the duration of individual picosecond pulses. The accuracy and relative simplicity of the technique increase with the number of pulses measured. An experimental test of the basis of the technique is described.

PACS numbers: 42.60.N, 42.65.

I. INTRODUCTION

Although a decade has passed since the generation of the first mode-locked laser pulses, the measurement of the duration of individual picosecond laser pulses is still accomplished only with difficulty. The only direct method of measurement is streak-camera photography.[1] The technology of streak photography has advanced to the point that subpicosecond resolution has been achieved,[2] and clearly streak photography is the optimal method of measurement when the experiment involves a limited number of pulses. However, the cost of a streak camera may be prohibitive. In addition, the associated photographic development and photodensitometric analysis of the data is time consuming. In that respect, a streak camera is not ideal as a simple and rapid monitor when many pulses are involved.

Single-pulse two-photon fluorescence[1] (TPF) is the most widely used method of measuring temporal duration. The advantages of this technique are experimental simplicity and economy. Several factors may hamper the straightforward interpretation of the data, however, as attested by the literature concerning the attainability of a contrast ratio of three.[3,4] Another such factor, that of nonlinear film response, will be mentioned here below. The actual temporal profile of the pulse cannot be reconstructed from the TPF trace. Indeed, one must assume a specific temporal shape in order to extract the pulse duration. The accuracy of that duration, therefore, depends on the degree to which the actual temporal profile conforms to the assumed profile. In this work with a Nd : YAG mode-locked laser we have assumed a Gaussian temporal profile. This assumption has been verified by others.[5] The TPF technique also involves photographic development and photodensitometric analysis for accurate measurements. Therefore, TPF measurement is also not ideal for use when many pulses are involved. It should be mentioned, however, that the use of a self-scanning photodiode array as the detector in a TPF arrangement[6] eliminates some of the above disadvantages of the TPF method.

We will describe in Sec. II a simple and economical technique which is a useful alternative to the above methods for many experiments, especially when large numbers of pulses are used. It is capable of measuring individual pulse durations relative to the average pulse duration of the laser output. The proper characteristic average pulse duration must be determined accurately by other means.[3] The technique presented should be useful for measuring single-pulse durations as short as 10^{-13} sec or less, provided the average pulse duration of such a short-pulse generator can be measured by other means. Section III describes an experimental test of the theory of the technique, the analysis and results of which are presented in Sec. IV.

II. THEORY OF THE τA TECHNIQUE

We begin the description of this technique by considering a laser pulse having Gaussian spatial and temporal distribution of intensity:

$$I(r,t) = I_0 \exp[-(r/\rho)^2] \exp[-(t/\tau)^2]. \tag{1}$$

The energy content in a sample of this pulse will be proportional to the quantity $\mathcal{E}_f$ given by

$$\mathcal{E}_f = \int_{-\infty}^{\infty} \int_0^{\infty} I(r,t)\, 2\pi r\, dr\, dt = \pi^{1/2} I_0 \tau A, \tag{2}$$

where $A = \pi\rho^2$ is the pulse area and τ is the $1/e$ half-width of the intensity distribution. Such an energy measurement is performed by the beam splitter BS-1, photodiode PD-1, and the oscilloscope in Fig. 1. If a second sample of such a pulse is converted to second-harmonic light, as by beam splitter BS-2 and the phase-matched second-harmonic generation crystal SHG-1 in Fig. 1, then for small conversion efficiencies the energy content of the pulse will be proportional to the quantity $\mathcal{E}_{sh}$ given by

$$\mathcal{E}_{sh} = \pi^{1/2} q I_0^2 \tau' A'. \tag{3}$$

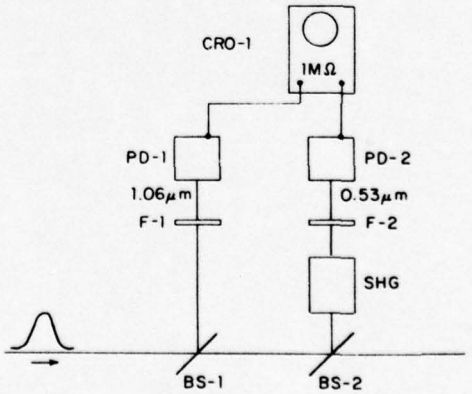

FIG. 1. Apparatus for pulse duration measurements with the τA technique. Notation: BS, wedged beam splitters; F, appropriate filter; SHG, phase-matched second-harmonic generation crystal; PD, biplanar photodiode; CRO, dual-beam oscilloscope.

The quantity q is a collection of constants, for a given experiment, involving the second-order nonlinear susceptibility, length of the harmonic-generation crystal, etc. In Eq. (3), the quantity $A' = \pi\rho'^2$ is the harmonic-pulse transverse area and τ' is the harmonic pulse $1/e$ half-width of the intensity. For small conversion efficiencies, we know that $\tau = 2^{1/2}\tau'$ and $\rho = 2^{1/2}\rho'$. Therefore, the ratio $\mathcal{E}_f^2/\mathcal{E}_{sh}$ can be written

$$\mathcal{E}_f^2/\mathcal{E}_{sh} = q'\tau A, \tag{4}$$

where q' is a second proportionality constant equal to $\pi^{1/2}2^{3/2}q^{-1}$. This ratio is observed to be linearly proportional to the product τA, a fact that was noted by Glenn and Brienza[7] in 1967 and employed by Shank and Ippen[8] in conjunction with a mode-locked cw dye laser. The ratio value is obtained simply from two oscilloscope signals or, alternatively, it could be obtained from digital equipment as a single numerical readout. In an experiment, therefore, if the value of the ratio $\mathcal{E}_f^2/\mathcal{E}_{sh}$ is recorded for each individual pulse, one needs only to normalize this set of numbers in order to obtain individual pulse values of τA. The normalization is easily achieved if two conditions are satisfied: (i) The average value of the pulse duration $\langle\tau\rangle$ and the pulse area $\langle A\rangle$ must be known. These are quantities that are routinely measured in the characterization of a laser source. (ii) Enough shots must be monitored such that the average of their recorded ratio numbers from Eq. (4) becomes meaningful and representative. During these shots, the conditions determining q' (the phase-matching angle of the harmonic generator, etc.) must not be allowed to change. If these two conditions are satisfied, then the average of the recorded ratio numbers, identified as $\langle\tau A\rangle$, may be set equal to the product of the known, previously measured average values, $\langle\tau\rangle\langle A\rangle$. The individual pulse ratio numbers are thereby calibrated absolutely in terms of this average. The quantity τA is just that needed to convert the easily measured individual pulse energy into individual pulse intensity. The latter quantity fluctuates from shot to shot in all mode-locked lasers, and heretofore has been difficult to measure. Usually, the average value $\langle\tau\rangle$ and $\langle A\rangle$ are used for all pulses, neglecting entirely their fluctuant behavior. If, to a reasonable approximation, the pulse-to-pulse fluctuations in A can be neglected, or if a self-scanning photodiode array is used to accurately determine A for each pulse, then individual pulse durations are easily obtained. It should be noted that the accuracy of the technique, in addition to its relative simplicity over the alternative methods, increases with the number of pulses utilized.

One other point should be noted. It concerns the effect of variation in the pulse temporal *profile*, and not just in the characteristic duration of that form, on the accuracy of the technique. It is not required that the laser pulses have Gaussian temporal and/or spatial functional form. A temporal and/or spatial form other than Gaussian will simply result in a different constant value of q' in Eq. (4). The values of $\mathcal{E}_f^2/\mathcal{E}_{sh}$ will still be proportional to the characteristic duration and area. So long as the proper characteristic average duration and area of the pulse have been determined by other means,[3] and are used in the normalization procedure, the technique presented here will function. However, if the functional form itself, and not just its characteristic area and/or duration, changes from shot to shot, then q' in Eq. (4) will no longer be constant and the strict proportionality there is lost. The accuracy of the technique will therefore be adversely affected. An example in which this limitation would be serious is that of a Nd:glass mode-locked laser without sufficient bandwidth reduction to remove noiselike substructure.

III. EXPERIMENT

We describe next an experiment that was conducted to test the validity of the linear correlation of $\mathcal{E}_f^2/\mathcal{E}_{sh}$ with τA as given by Eq. (4). The experimental arrangement is schematically illustrated in Fig. 2. The Nd:YAG oscillator is mode locked by a 0.5-mm-thick sheet of flowing Kodak 9860 dye. Transverse oscillation is constrained by an intracavity aperture to the TEM_{00} mode. The single-pulse switch-out mechanism is a standard Pockels cell pulsed by a laser-triggered spark gap. The components within the dashed line in Fig. 2 are those of Fig. 1 and they were used to record ratio values of Eq. (4) for each pulse. Photodiode PD-3 is a high-speed biplanar device used with Tektronix 519 oscilloscope CRO-2 to monitor each pulse and insure that only data from single pulses without satellite structure is employed. Beam splitter 4 directs a fraction of the pulse into a phase-matched second-harmonic-generation crystal SHG-2. The harmonic output strikes a MgO diffuser D and is photographed by camera C-1. This multilens camera[9] (MLC) is used to measure the harmonic pulse area A', from which the fundamental pulse area A is calculated. Kodak Royal-X pan film was found to be sensitive enough to yield good exposure from a single pulse. The remainder of the pulse is di-

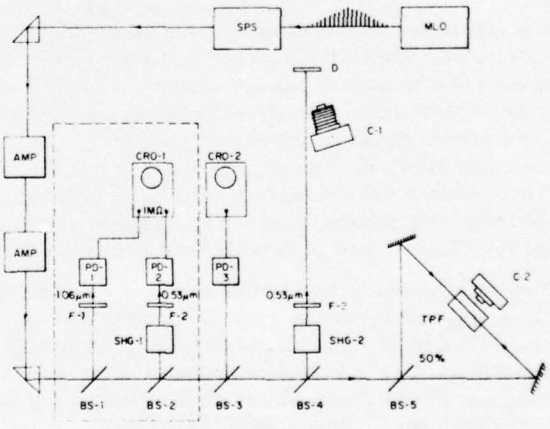

FIG. 2. Schematic diagram of the experimental arrangement. Notation: MLO, Nd:YAG mode-locked oscillator; SPS, single-pulse selector employing a laser-triggered spark gap and Pockels cell; AMP, Nd:YAG amplifier; BS, beam splitter; F, appropriate filter; SHG, phase-matched KDP second-harmonid generation crystal; PD, biplanar photodiode; CRO-1, Tektronix 555 dual-beam oscilloscope; CRO-2, Tektronix 519 oscilloscope; D, MgO diffuser block; C-1, multilens camera; C-2, camera; TPF, two-photon fluorescence cell containing rhodamine 6G in ethanol. The components within the dashed line are those of Fig. 1.

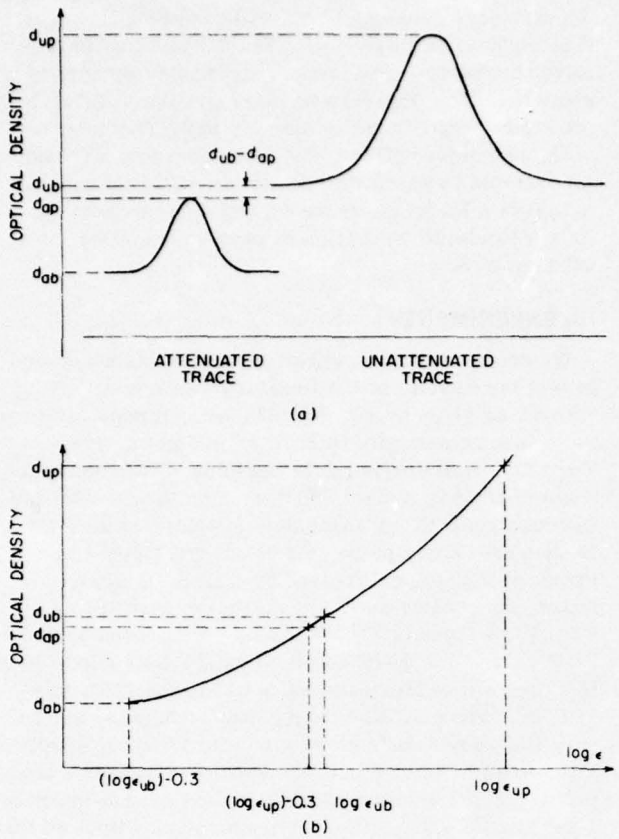

FIG. 3. (a) Schematic illustration of the TPF photodensitometer output from one shot; (b) Hurter-Driffield presentation of the data from (a). The letter d denotes optical density and log denotes the common logarithm. The subscripts u, a, p, and b denote the unattenuated trace, attenuated trace, peak level, and background level, respectively.

rected into a TPF arrangement. The TPF medium is rhodamine 6G, and Kodak Royal-X Pan Film was used in camera C-2 to record the TPF traces. The TPF cell housing employed two mirrors to direct two images of the TPF trace, one from either side of the cell, into the camera. However, one of these images was attenuated by a neutral density filter placed in its path inside the housing. The attenuated trace was used to check linearity of film response as will be described below.

The experiment was performed by firing a series of single pulses and recording various signals. The two traces from CRO-1 yield values of $\mathcal{E}_f^2/\mathcal{E}_{sh}$. The MLC data yields another independent measure of the pulse area A, and the TPF data yields an independent value of τ, for each pulse. Therefore, the product of A and τ, from the MLC and TPF data, should be linearly correlated with the value of $\mathcal{E}_f^2/\mathcal{E}_{sh}$ from CRO-1, according to Eq. (4).

IV. ANALYSIS AND RESULTS

In order to determine with what accuracy the ratio $\mathcal{E}_f^2/\mathcal{E}_{sh}$ detects variations in τ and A, the MLC and TPF data must be accurately analyzed. The problem of film response nonlinearity is absent in the MLC technique but not in the TPF technique. Indeed, high-speed films used to photograph single-pulse TPF traces offer correspondingly lower latitude.

The problem of film response linearity was taken into account in our experiment by recording two images of each TPF trace, one of which was attenuated with a neutral density filter of known optical density. An example of the photodensitometer trace output from one shot is shown schematically in Fig. 3(a). The exposure ϵ from the TPF has the spatial dependence

$$\epsilon(z) = \epsilon_0[1 + Q\exp\{-2(zn/c\tau)^2\}], \tag{5}$$

assuming the incident pulse shape of Eq. (1). Here the z axis is the axis of propagation in the TPF cell, having its origin at the point where the two pulses fully overlap. In Eq. (5), Q is equal to the contrast ratio minus 1.0, n is the refractive index of the TPF medium, and c is the vacuum speed of light. Figure 3(b) displays the Hurter-Driffield information obtained from Fig. 3(a). The exposure values of the two peaks of Fig. 3(a) are related by the known filter attenuation factor, in our case 50%. Thus, if $\log\epsilon_{up}$ is the common logarithm of the exposure of the point corresponding to the density d_{up}, then the abscissa of the point corresponding to d_{up} is $\log(\epsilon_{up}) - 0.3$. The abscissae $\log(\epsilon_{up})$ and $\log(\epsilon_{ub}) - 0.3$ result from the background densities of the unattenuated and attenuated traces, respectively, in identical fashion. Therefore, only a relation between $\log(\epsilon_{up})$ and $\log(\epsilon_{ub})$ is needed to plot all four points as shown in Fig. 3(b). In our analysis, use was made of the fact that $d_{ub} - d_{ap}$ was very small, i.e., $0.1(d_{ap} - d_{ab})$ or less, on all the traces from the experiment. This was due to fortuitous exposure conditions. Therefore, the film response was taken as linear over this small region, a very good approximation. An effective slope γ was computed as the average of the slope from the pair of background points and from the pair of points from the peaks of the curves. The points $\log(\epsilon_{ub})$ and $\log(\epsilon_{up}) - 0.3$ were then connected via the relation

$$d_{ub} = d_{ap} + \gamma[0.3 + \log(\epsilon_{ub}/\epsilon_{up})]. \tag{6}$$

This process established the positions of the four points as shown in Fig. 3(b). A quadratic curve was then least-squares fit to the four points, yielding the solid curve in Fig. 3(b). The proper optical density $d_{1/2}$ that correctly corresponds to the half-intensity point of the fluorescence above the background was then found from the relation $\log\epsilon_{1/2} = \log(\epsilon_{up} + \epsilon_{ub}) - 0.3$ and the curve of Fig. 3(b). The full width W of the TPF densitometer trace at the $d_{1/2}$ level then yields the temporal $1/e$ intensity duration via $\tau = Wn/c(2\ln 2)^{1/2}$, where c is speed of light and n is the refractive index of the TPF medium.

TABLE I. Test of the linear correlation of $\mathcal{E}_f^2/\mathcal{E}_{sh}$ with τA.

Pulse No.	τ_{TPF}[a] (psec)	V_1[b] $\propto \tau_{TPF} A_{MLC} \propto$	V_2[b] $\frac{\mathcal{E}_f^2}{\mathcal{E}_{sh}}$	$\frac{V_1}{V_2}$	$V_1/V_2 - \langle V_1/V_2\rangle$ (%)
1	15.4	1.00	1.00	1.00	+3.1
2	15.4	1.00	1.03	0.97	0.0
3	16.5	1.14	1.25	0.91	−6.2
4	18.1	1.36	1.51	0.90	−7.2
5	20.7	1.82	1.71	1.06	+9.3

[a] The full-width–at–half-intensity duration is equal to $2(\ln 2)^{1/2}\tau$.
[b] Normalized to 1.00.

In the above manner, τ_{TPF} was deduced from TPF for each of the five laser pulses and the values are listed in Table I. The area A_{MLC} was found from the technique of Ref. 9 for each pulse. In the third column of Table I, the normalized values of the product of τ_{TPF} and A_{MLC} are listed. The normalized values of the ratio $\mathcal{E}_f^2/\mathcal{E}_{sh}$ are listed in column 4. The ratio of the values of columns 3 and 4 is listed in column 5. The degree to which the fifth column ratio elements are mutually equal indicates the accuracy of the τA technique embodied by Eq. (4). The sixth column lists the variation of the entries in column 5 about their average. Therefore, the correlation of the quantity $\mathcal{E}_f^2/\mathcal{E}_{sh}$ with the product of the pulse duration τ and area A is demonstrated to be linear within about $\pm 10\%$.

The advantages of the τA technique outlined above are obvious: (i) minimal expenditure of pulse energy in the τA measurement itself (as opposed to 1.06-μm single-pulse TPF); (ii) freedom from error introduced by film nonlinearity, a problem often encountered when photographic film is used with picosecond pulses, e.g., in TPF photography; (iii) low cost and simplicity of apparatus; (iv) rapidity of data acquisition and analysis, and ease of incorporation of digital methods. These advantages suggest the attractiveness of the technique as a permanent on-line monitor. The simple scheme described above is useful in obtaining accurate data for processes which are highly nonlinear in the intensity, such as laser-induced breakdown[10] and electron emission,[11] multiphoton ionization, etc.

The authors appreciate helpful comments and support from Professor N. Bloembergen of Harvard University.

*Research supported in part by the National Aeronautics and Space Administration and by the Joint Services Electronics Program.

[1]D. J. Bradley and G. H. C. New, Proc. IEEE 62, 313 (1974).
[2]Laser Focus 11, 28 (1975).
[3]P. W. Smith, M. A. Duguay, and E. P. Ippen, in *Progress in Quantum Electronics*. edited by J. H. Sanders and S. Stenholm (Pergamon, Oxford, 1974), Vol. 3, Part 2.
[4]R. C. Greenhow and A. J. Schmidt, in *Advances in Quantum Electronics*. edited by D. W. Goodwin (Academic, New York, 1974), Vol. 2, p. 157.
[5]L. A. Lampre, G. Mainfray, and J. Thebault, Appl. Phys. Lett. 26, 501 (1975); A. W. Smith and A. J. Landon, Appl. Phys. Lett. 17, 340 (1970).
[6]W. Seka and J. Zimmerman, Rev. Sci. Instrum. 45, 1175 (1974).
[7]W. H. Glenn and M. J. Brienza, Appl. Phys. Lett. 10, 221 (1967).
[8]C. V. Shank and E. P. Ippen, Appl. Phys. Lett. 24, 373 (1974).
[9]I. M. Winer, Appl. Opt. 5, 1437 (1966).
[10]W. L. Smith, J. H. Bechtel, and N. Bloembergen, Phys. Rev. B 12, 706 (1975).
[11]J. H. Bechtel, W. L. Smith, and N. Bloembergen, Opt. Commun. 13, 56 (1975).

Appendix III

Pulse Width Fluctuations in Mode-locked Nd:YAG Lasers

Volume 55A, number 4 PHYSICS LETTERS 15 December 1975

PULSE WIDTH FLUCTUATIONS IN MODE-LOCKED Nd:YAG LASERS ☆

J.H. BECHTEL and W.L. SMITH
Gordon McKay Laboratory, Harvard University, Cambridge, Massachusetts 02138, USA

Received 18 August 1975

Using a nonlinear optical technique we have measured pulse width fluctuations in a passively mode-locked Nd:YAG laser.

An important aspect of mode-locked laser pulses is the pulse duration. We have measured the pulse with fluctuations by a technique that is based on observing both the total pulse energy and the pulse energy created by second harmonic generation in a nonlinear crystal [1–3].

Consider a laser pulse in the form of a spatially and temporally Gaussian pulse. In this case the irradiance is given by $I(r, t) = I_m \exp(-(r/d)^2)\exp(-(t/\tau)^2)$. The total pulse energy E_f is given by the expression

$$E_f = \pi^{1/2} I_m \tau A$$

where $A = \pi d^2$. For small second harmonic conversion efficiencies the total pulse energy E_{sh} created by phased matched second harmonic generation is given by

$$E_{sh} = q\pi^{1/2} I_m^2 \tau' A'$$

where q is a constant that depends on the nonlinear susceptibility the length of the harmonic generation crystal, and other parameters that do not change during the experiment. Here $\tau' = \tau/2^{1/2}$ and $A' = A/2$. Thus the ratio E_f^2/E_{sh} becomes

$$E_f^2/E_{sh} \propto \tau A.$$

If we assume that both the shape of the pulse and the pulse area do not change from shot-to-shot then our measurement of E_f^2/E_{sh} is simply proportional to the pulse duration.

A schematic diagram of the experiment is exhibited in fig. 1. The laser used for this experiment was a flashlamp pumped Nd:YAG laser rod in the Brewster-Brewster configuration. The laser was passively mode-locked by a 0.5 mm thick flowing dye (Kodak 9860) in contact with the high reflectivity rear mirror. The output was restricted to the fundamental transverse mode, TEM_{00}, by a 2 mm diameter aperture within the oscillator cavity. A single pulse was selected from the train of mode-locked pulses by a cylindrical-ring electrode Pockels cell. This pulse was subsequently amplified by two Nd:YAG amplifiers.

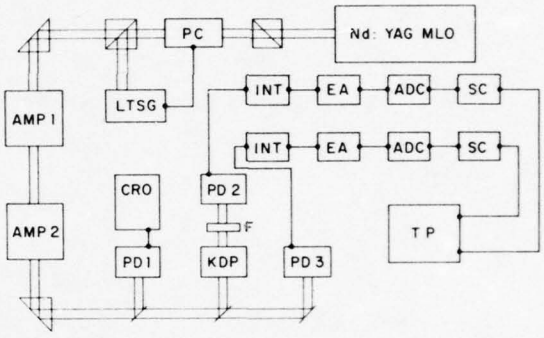

Fig. 1. Schematic diagram of the experiment. Nd:YAG MLO, neodymium doped yittrium aluminum garnet mode-locked oscillator; PC, Pockels cell; LTSG, laser triggered spark gap; AMP, neodymium doped yittrium aluminum garnet laser amplifiers; PD, photodiode; CRO, Tektronix 519 oscilloscope; F, filter; KDP, potassium dihydrogen phosphate second harmonic generation crystal; INT, integrator; EA, electronic amplifier; ADC, analogue to digital converter; SC, scaler; TP, teletype printer.

A photodiode, PD1, monitored the laser pulse with a Tektronix 519 oscilloscope to insure that only a single pulse was selected from the train of pulses. Calibrated photodiodes PD3 and PD2 measured respective-

☆ Supported in part by the Joint Services Electronics Program and the National Aeronautics and Space Administration.

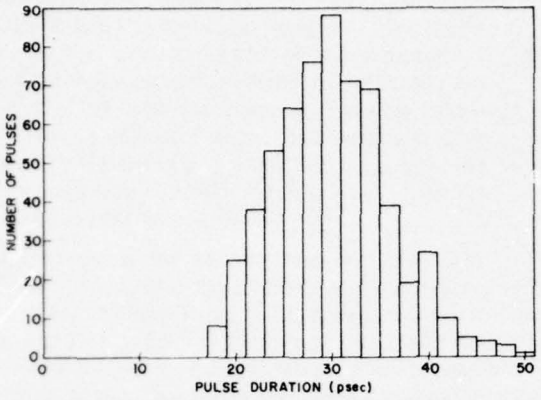

Fig. 2. Histogram showing pulse width variation for passively mode-locked Nd:YAG laser. The pulse duration is the full width at half maximum (FWHM).

ly the total pulse energy at the fundamental frequency and the total pulse energy at the second harmonic frequency. These photodiode signals were monitored by a digital data acquisition system and displayed on a teletype printer. The average pulse duration full width at half maximum (FWHM) corresponding to the measured average value of E_f^2/E_{sh} was set equal to 30 psec. This value was determined for our laser by a second harmonic autocorrelation technique employing a Michelson interferometer [4]. Fig. 2 exhibits a histogram of the total number of pulses observed with pulse duration (FWHM) between the endpoints of the horizontal axis, e.g., 88 observed pulses between 29 and 31 psec (FWHM).

The statistical nature of passive mode-locking is well known [5]. The variance of the fluctuations observed here is larger than that predicted by others on that basis. From ref. [5] one obtains $\delta\tau/\tau = m^{-1/2}$ where m is the number of locked longitudinal modes. For $m = 100$, $\delta\tau/\tau = 0.1$. A larger variation would be expected, however, if a more realistic model of the saturable absorber [6] were employed. In addition, natural nonuniformities in the flowing dye will increase the variation in the pulse width.

In conclusion we note that substantial pulse duration fluctuations can occur with passive mode-locking in Nd:YAG lasers. Similar pulse duration fluctuations have been observed in the initial pulses from the pulse train of passively mode-locked Nd:glass lasers [7]. These fluctuations were, however, observed with a streak camera.

We wish to acknowledge the support and encouragement of Professor N. Bloembergen.

References

[1] W.H. Glenn and M.J. Brienza, Appl. Phys. Lett. 10 (1967) 221.
[2] C.V. Shank and E.P. Ippen, Appl. Phys. Lett. 24 (1974) 373.
[3] W.L. Smith and J.H. Bechtel, unpublished.
[4] H.P. Weber and H.G. Danielmeyer, Phys. Rev. A2 (1970) 2074.
[5] P.G. Kryukov and V.S. Letokhov, IEEE J. Quant. Electron. QE-8 (1972) 766.
[6] M. Hercher, Appl. Opt. 6 (1967) 947;
G. Girard and M. Michon, IEEE J. Quant. Electron. QE-9 (1973) 979.
[7] D.J. Bradley and W. Sibbett, Opt. Commun. 9 (1973) 17.

Appendix IV.A

Four-photon Photoemission from Tungsten

Volume 13, number 1 OPTICS COMMUNICATIONS January 1975

FOUR-PHOTON PHOTOEMISSION FROM TUNGSTEN*

J.H. BECHTEL, W.L. SMITH and N. BLOEMBERGEN
Gordon McKay Laboratory, Harvard University, Cambridge, Massachusetts 02138, USA

Received 15 November 1974

Four-photon photoemission is observed from tungsten using carefully controlled and calibrated single pulses produced by a passively mode-locked Nd:YAG laser system. The results are shown to be in quantitative agreement with a four-photon generalization of the Fowler and DuBridge theories of photoemission.

Since the advent of the laser multiple-photon photoemission has been observed from several metals. Two-photon photoemission from sodium has been observed by Teich and Wolga by the use of gallium arsenide laser [1]. Both two-photon and three-photon photoemission have been observed from gold by the use of a ruby laser and the second harmonic radiation produced by a ruby device [2]. The observation of higher order multiple-photon photoemission has now been facilitated by the use of high power, ultrashort pulse, mode-locked lasers. These lasers can produce the very high irradiances necessary for the observation of multiple-photon photoemission, and yet because of the short pulse duration, catastrophic heating effects may not occur. Preliminary results of electron emission produced by a mode-locked Nd:glass laser have been presented in ref. [3]. Unfortunately, these results were inconclusive because the authors of ref. [3] used the entire pulse train of the laser, and they found an asymmetry in the electron emission depending upon whether it was produced by the leading or the trailing portions of the train of pulses. They attributed this asymmetry to the chirping of the pulses [4] or to satellite pulse formation. We report here the observation of four-photon photoemission from tungsten by the use of carefully controlled and calibrated single, amplified pulses produced by a passively mode-locked Nd:YAG laser followed by two Nd:YAG amplifiers.

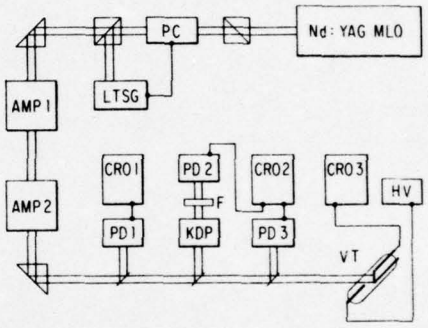

Fig. 1. Schematic diagram of the experimental arrangement. MLO, mode-locked oscillator; PC, Pockels cell; LTSG, laser-triggered spark gap; AMP, Nd:YAG amplifier; PD, photodiode; CRO, oscilloscope; KDP, potassium dihydrogen phosphate second harmonic generation crystal; F, filter; HV, high voltage power supply; VT, electron emission vacuum tube.

Fig. 1 exhibits a block diagram of the experimental apparatus. The laser oscillator used for this experiment is a 6 mm diameter by 3 inch long Nd:YAG rod. The laser is simultaneously Q-switched and mode-locked by a flowing saturable absorber, Kodak 9860, placed in contact with the high reflectivity mirror of the oscillator cavity. The laser oscillator output is restricted to the TEM_{00} mode by a 2 mm diameter aperture placed within the cavity. The output of the oscillator consists of a train of subnanosecond pulses separated by approximately 8 nsec. From this train a single

* Research supported in part by the National Aeronautics and Space Administration (under contract NGR-22-007-117) and by the Joint Services Electronics Program (under contract N00014-67-A-0298-0006).

pulse is selected for amplification by a spark-gap activated, cylindrical-ring electrode Pockels cell. After this amplification with two single pass Nd:YAG amplifiers we obtain a single, high power, subnanosecond pulse with a wavelength of 1.064 μm. The spatial profile of this pulse was measured by transverse scans of a 50 μm diameter pinhole. The spatial distribution of the laser irradiance at the site of the experiment was found to be gaussian with a radius at the 1/e point of the irradiance equal to 1.1 mm.

The determination of the pulse duration of a mode-locked Nd:YAG laser imposes some problems because the pulse width is less than the response time of the fastest available oscilloscopes. In order to determine the average pulse length we have used both a two-photon fluorescence technique [5] and a second harmonic nonlinear correlation method [6]. Both of these methods utilized many selected pulses, and the results of both measurements give an average pulse duration of 30 psec full width at half maximum (fwhm) for the laser used in this experiment.

To determine the incident peak irradiance of an individual pulse it is necessary to know the pulse energy, the pulse duration, the beam area, and the pulse shape. We shall assume that the functional form of the pulse shape does not change from shot to shot, and that it is both spatially and temporally gaussian. The energy of an individual pulse was determined by the response of photodiode 3 (see fig. 1) which is calibrated with an Eppley thermopile. The product of the pulse duration and the beam area may also be determined for an individual pulse by a second harmonic generation method. For a pulse irradiance of the form

$$I(r, t) = I_m \exp[-(r/d)^2] \exp[-(t/\tau)^2] ,$$

the pulse energy, E_f, is given by the expression $E_f = \pi^{3/2} d^2 I_m \tau$. For small conversion efficiencies the total energy at the second harmonic wavelength produced by this pulse is given by the expression

$$E_{sh} = \pi^{3/2} d^2 I_m^2 \tau \chi^{eff}/2^{3/2} .$$

Here χ^{eff} is the effective nonlinear susceptibility. From this we note that the ratio E_f^2/E_{sh} is proportional to the product of the beam area and the pulse duration. Therefore by equating the average value of E_f^2/E_{sh} for a series of laser pulses to the known product of the average beam area and the average pulse duration we can determine the product of the pulse width and the beam area for an individual pulse. Since we know the total pulse energy, we can calculate the maximum irradiance, I_m, for each pulse. Moreover, if it can be assumed that the beam area does not change from shot to shot, then this technique yields single pulse temporal widths in a simple manner. This detailed knowledge is essential for an accurate quantitative measurement of a highly nonlinear process.

During the taking of data for the laser-induced electron emission the incident laser pulse was monitored with a fast biplanar photodiode (ITT F4000) and a Tektronix 519 oscilloscope (oscilliscope 1). This was done to insure that the oscillator did not have more than one pulse in the cavity during the mode-locking and that the Pockels cell was selecting only one pulse for amplification. The energy of the 1.064 μm laser pulse was measured for each data point by the combination of oscilloscope 2 and photodiode 3. The second harmonic radiation was produced in a phase-matched KDP crystal, and the energy at 0.532 μm was measured for each data point by the combination of oscilloscope 2 and photodiode 2.

The electron emission was detected by measuring the total charge emitted from the tungsten ribbon target. This emission was recorded photographically with oscilloscope 3. The tungsten ribbon was 0.003 inches thick, 0.04 inches wide and approximately 1 inch long. The pressure in the vacuum tube containing the tungsten ribbon was measured as 1×10^{-7} torr. The ribbon could be outgassed by passing a current of approximately 10 A through it, and immediately before the taking of data very high irradiances produced by the laser were used to further clean the area from which the emission would occur. The voltage between the cathode and the anode was 6000 V.

In fig. 2 we plot the effective current density versus the maximum incident irradiance. By effective current density we mean the total emitted charge per pulse divided by the product of the laser area (πd^2) and the pulse duration (fwhm).

In order to explain the observed electron emission we shall use a theory that can be considered as a generalization of the photoemission theories of Fowler [7] and DuBridge [8,9]. The four-photon current density is given by the expression

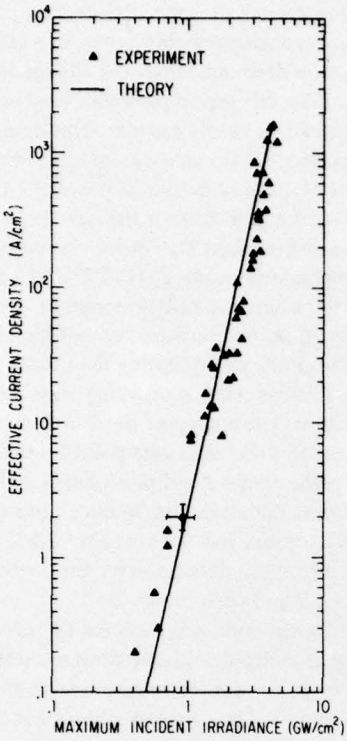

Fig. 2. Plot of the effective current density [total emitted charge divided by the product of πd^2 and the pulse duration (fwhm)] versus the peak incident irradiance. The theoretical curve is obtained from a four-photon generalization of the theories of Fowler and DuBridge.

$$J_4 = a_4\left(\frac{e}{h\nu}\right)^4 AI^4(1-R)^4T^2F\left(\frac{4h\nu-\phi}{kT}\right) .$$

Here e is the electron charge, R is the surface reflectivity, A is the theoretical Richardson constant, $h\nu$ is the energy of an incident photon, ϕ is the work function, k is Boltzmann's constant, I is the incident irradiance, T is the absolute temperature of the surface, and a_4 is an empirically determined constant. The function $F(x)$ is the Fowler function and is tabulated in ref. [8]. The total charge emitted per pulse is theoretically predicted by a numerical integration of J_4 over the spatial and temporal dimensions of the incident pulse. To perform this integration we assume that the incident irradiance is spatially and temporally gaussian. Using this form for the incident irradiance we can determine the spatial and the temporal dependence of the surface temperature by solving the heat conduction equation. The details of this temperature calculation will appear elsewhere. We note, however, that the result of this calculation gives a maximum surface temperature change of approximately 700 K for a 1 GW/cm^2 maximum irradiance, 30 psec (fwhm) pulse impinging on a tungsten target.

At the highest irradiances used in this experiment the maximum temperature is estimated to be near 3000 K. The question may therefore be raised, whether excited contributions to the emitted current become important. Quite generally the current density may be written as

$$J = \sum_{n=0}^{\infty} J_n ,$$

with

$$J_n = a_n\left(\frac{e}{h\nu}\right)^n AI^n(1-R)^nT^2F\left(\frac{nh\nu-\phi}{kT}\right) .$$

The term J_0 is independent of the incident light intensity and represents pure thermionic emission. At a maximum irradiance of 4 GW/cm^2 we calculate that the thermionic current density is less than 1 A/cm^2. This is more than three orders of magnitude less than the measured effective current density for a maximum irradiance of 4 GW/cm^2, and thus thermionic emission is negligible.

It is possible to have contributions from terms analogous to J_4 involving one, two, or three photons [10], given by J_1, J_2 and J_3. These terms represent photoelectric emission processes from the thermally excited high-energy tail of the Fermi–Dirac electron distribution. For these processes the argument of the Fowler function is negative, as it is for J_0. Their contribution is very small even for the highest temperatures achieved here. Moreover, if there were any contribution from these lower order processes, then the slope of the experimental curve would be at least a factor of two larger than the observed slope.

The result of the theoretical calculation of the effective four-photon current density is exhibited also in fig. 2. The constant a_4 is chosen to be 5×10^{-42} cm^8-sec^4/C^4, and the pulse duration is assumed to be 30 psec (fwhm). Moreover, we also assume that the reflectivity at 1.064 μm is 0.6, the work function is 4.52 eV, and the photon energy is 1.165 eV. When the

theoretical curve and the experimental data points are plotted on a log–log scale as in fig. 2, then the slope of each should be nearly four if the dominant electron emission process is four-photon photoemission. The thermally induced contributions would increase the slope to values higher than four, at the large irradiances.

In addition, since different pulse widths produce different temperature changes for a given peak irradiance, some fluctuations in the effective current density are expected for a given peak irradiance.

We conclude that careful control and careful calibration of individual picosecond pulses have permitted the unambiguous verification of a four-photon photoelectric process. For longer pulses, more heating occurs for a given level of irradiance. The contributions from thermally induced processes become usually significant, and for longer pulses it is difficult to identify unambiguously one high-order multiphoton process.

References

[1] M.C. Teich and G.J. Wolga, Phys. Rev. 171 (1968) 809.
[2] E.M. Logothetis and P.L. Hartman, Phys. Rev. 187 (1969) 460.
[3] Gy. Farkas, Z.Gy. Horath, I. Kertesz and G. Kiss, Nuovo Cimento Lett. 1 (1971) 314.
[4] O.S. Svelto, Appl. Phys. Lett. 17 (1970) 83.
[5] D. von der Linde, O. Bernecker and W. Kaiser, Opt. Commun. 2 (1970) 149.
[6] H.P. Weber and H.G. Danielmeyer, Phys. Rev. A2 (1970) 2074.
[7] R.H. Fowler, Phys. Rev. 38 (1931) 45.
[8] L.A. DuBridge, Phys. Rev. 39 (1932) 108.
[9] L.A. DuBridge, Phys. Rev. 43 (1933) 727.
[10] J.H. Bechtel, Ph.D. thesis, The University of Michigan, 1973 (unpublished).

Appendix IV.B

Two-photon Absorption in Semiconductors with Picosecond Laser Pulses

PHYSICAL REVIEW B VOLUME 13, NUMBER 8 15 APRIL 1976

Two-photon absorption in semiconductors with picosecond laser pulses*

J. H. Bechtel and W. L. Smith
Gordon McKay Laboratory, Harvard University, Cambridge, Massachusetts 02138
(Received 10 November 1975)

Single pulses from a well-calibrated mode-locked YAlG:Nd laser have been used to measure the two-photon absorption coefficient at 1.064 μm in several semiconductors. The materials studied are four direct-gap semiconductors, GaAs, CdTe, ZnTe, and CdSe, and one indirect-gap semiconductor, GaP. The results for the direct-gap semiconductors are interpreted with respect to the imaginary part of the third-order nonlinear susceptibility $\chi^{(3)}_{1111}(-\omega,\omega,\omega,-\omega)$. An anisotropy of the two-photon absorption coefficient is observed in GaAs.

I. INTRODUCTION

With the development of quantum mechanics in the late nineteen-twenties it became clear that when electromagnetic radiation interacts with matter, processes involving more than one photon can occur. One such interaction is two-photon absorption (TPA) and the basic theory for this process was formulated by Maria Goppert-Mayer in 1931.[1] The experimental observation of two-photon absorption had to await the development of the laser, however, and the first experimental observation was reported by Kaiser and Garrett in 1961.[2]

Several techniques are used to study two-photon absorption. One technique involves measuring the transmission of the two-photon absorbing material for different incident irradiances. Another involves measuring the luminescence from a material pumped by two-photon excitation, and a third involves measuring the change in the conductivity of a material under two-photon excitation.

There are several reasons for studying two-photon absorption in various materials. Not only can two-photon absorption measurements yield new information on the electronic states in a solid, but also TPA can provide a novel method of exciting large volumes in semiconducting and insulating materials. Such excitation has been used previously to pump semiconductor lasers.[3] Moreover, two-photon absorption can provide a damaging mechanism in materials that are nearly transparent to low-intensity radiation. This will constitute a very serious materials problem to the development of high-power ultraviolet lasers. Finally, two-photon absorption techniques in both liquids and solids have provided useful tools in ultrashort-pulse laser diagnostics.[4]

For comprehensive reviews involving many aspects of two-photon absorption and spectroscopy we refer the reader to Refs. 5 and 6.

There have been several previous studies of TPA in semiconductors, but there are very large differences in the measured values of the TPA coefficients. For example, in GaAs the measured values range from 0.02–5.6 cm/MW at a laser wavelength of 1.06 μm. Values of the TPA coefficient will be presented here for GaAs, CdTe, ZnTe, CdSe, and GaP.

Since two-photon absorption is a nonlinear optical phenomenon, the TPA coefficient can be expressed in terms of nonlinear optical susceptibilities. In Sec. II we outline a theory of TPA and relate this theory to nonlinear optics. In Sec. III the experimental apparatus and procedure are discussed. In Sec. IV the results of the TPA measurements are presented. Finally in Sec. V we discuss the results of our experiments and their relation to other experiments and theory.

II. THEORY

In semiconductors it is possible to have TPA from a single light pulse with angular frequency ω if twice the photon energy, $2\hbar\omega$, exceeds the semiconductor energy gap E_g. The number of two-photon transitions per unit volume per unit time $W^{(2)}$ is given by second-order perturbation theory as

$$W^{(2)} = \frac{(2\pi)^3}{n^2 c^2 \hbar^2}\left(\frac{I}{\hbar}\right)^2 \sum_f |M_{fg}|^2 \,\delta(\omega_{fg} - 2\omega)\,, \qquad (1)$$

where

$$M_{fg} = \frac{e^2}{m^2\omega^2}\sum_i \frac{\vec{p}_{fi}\cdot\hat{a}\,\vec{p}_{ig}\cdot\hat{a}}{\omega_{ig}-\omega}\,.$$

Here n is the index of refraction of the semiconductor, c is the vacuum speed of light, m is the electron mass, e is the electron charge, $\hbar$ is Planck's constant divided by 2π, and I is the power per unit area of the laser radiation. The sums are to be extended over all final states (or bands) denoted by the index f and all intermediate states denoted by the index i. The ground state is denoted by the subscript g, and the transition rate should be averaged over this index if there is more than one possible initial state.

The unit vector $\hat{a}$ is directed along the electric field of the laser, and $\vec{p}_{fi}$ and $\vec{p}_{ig}$ are matrix elements of the momentum operator between respectively the final state and the intermediate state,

and the intermediate state and the ground state. The angular frequencies ω_{fg} and ω_{ig} correspond to the angular frequency differences between the final and ground states and the intermediate and ground states, respectively. These differences, in general, depend on the wave vector $\vec{k}$. If we express the transition rate in terms of the peak electric field amplitude E instead of the irradiance I the transition rate per unit volume becomes

$$W^{(2)} = \frac{2\pi}{\hbar}\left(\frac{eE}{2m\omega}\right)^4 \times \sum_f \left| \sum_i \frac{\vec{p}_{fi}\cdot\hat{a}\,\vec{p}_{ig}\cdot\hat{a}}{\hbar\omega_{ig}-\hbar\omega} \right|^2 \delta(\hbar\omega_{fg}-2\hbar\omega) \ . \quad (2)$$

In addition to the perturbation-theory calculations of $W^{(2)}$ that involve matrix elements between the initial and final unperturbed states, it is also possible to calculate the transition rate by a method that includes the effect of the electromagnetic field on the Bloch wave functions at the beginning of the calculation. Such a theory has been described by Keldysh.[7] In this model the band distortion due to the electromagnetic field is included and the results are applicable to both the optical and the dc limits. Moreover, for higher-order multiple-photon processes the Keldysh model offers both a simple and convenient method of estimating transition rates.

One method of measuring TPA in semiconductors is to measure the attenuation of a beam or pulse propagating through a two-photon absorbing medium. If the pulse irradiance is I, then the pulse is attenuated according to the expression

$$\frac{dI}{dz} = -\alpha I - \beta I^2 \ . \quad (3)$$

Here α is the one-photon absorption coefficient and β is the two-photon absorption coefficient. If we neglect multiple reflections within the medium, the transmitted irradiance is given by the expression

$$I(r, l, t) = \frac{(1-R)^2 I(r, 0, t) e^{-\alpha l}}{1+\beta(1-R) I(r, 0, t)(1-e^{-\alpha l})/\alpha} \ . \quad (4)$$

Here l is the thickness and R is the reflectivity of the medium.

The TPA coefficient β is related to the two-photon transition rate per unit volume by the expression

$$\beta = 2\hbar\omega W^{(2)}/I^2 \ . \quad (5)$$

An alternative formulation of the TPA problem is to start with Maxwell's wave equation and treat TPA as a nonlinear source polarization. For a monochromatic beam the electric field amplitude $\vec{E}(\vec{r}, \omega)$ is determined by the solution to this wave equation given by

$$\nabla\times\nabla\times\vec{E}(\vec{r}, \omega) - (\omega^2/c^2)\,\vec{\epsilon}\cdot\vec{E}(\vec{r}, \omega) = (4\pi\omega^2/c^2)\,\vec{P}^{\rm nls}(\vec{r}, \omega) \ . \quad (6)$$

Here $\vec{\epsilon}$ is the linear dielectric tensor and $\vec{P}^{\rm nls}(\vec{r}, \omega)$ is the nonlinear source dipole moment per unit volume.

For TPA the relevant nonlinear source polarization term is cubic in the electric field and is purely imaginary in character. In centrosymmetric media the relation is

$$P_i^{\rm nls}(\vec{r}, \omega) = i\chi_{ijkl}^{(3)\prime\prime}(-\omega, \omega, \omega, -\omega) \times E_j(\vec{r}, \omega) E_k(\vec{r}, \omega) E_l^*(\vec{r}, \omega) \ . \quad (7)$$

Here $\chi_{ijkl}^{(3)\prime\prime}(-\omega, \omega, \omega-\omega)$ is the imaginary part of the complex third-order nonlinear susceptibility. In non-centro-symmetric media for electric field directions such that second-harmonic generation is not symmetry forbidden there are contributions to $P^{\rm nls}$ not only from the imaginary part of $\chi^{(3)}(-\omega, \omega, \omega, -\omega)$ but also from terms proportional to $\chi^{(2)}(-\omega, 2\omega, \omega)\,\chi^{(2)}(-2\omega, \omega, \omega)$. For a detailed discussion of these effects see Ref. 8.

We will be interested in determining the TPA coefficient β for laser electric field directions that preclude the generation of second-harmonic radiation. In this case the total nonlinear source polarization is given by Eq. (7). By using the slowly varying amplitude approximation to solve Eq. (6) we can express β in terms of $\chi_{ijkl}^{(3)\prime\prime}(-\omega, \omega, \omega, -\omega)$. The explicit relation between β and $\chi_{ijkl}^{(3)\prime\prime}(-\omega, \omega, \omega-\omega)$ depends both on the crystal class and the laser electric field direction. For example, in a crystal of $\bar{4}3m$ symmetry (e.g., GaAs, CdTe, or ZnTe) with the laser electric field polarized along the [001] direction we find

$$\beta = (32\pi^2\omega/n^2c^2)\,[3\chi_{1111}^{(3)\prime\prime}(-\omega, \omega, \omega, -\omega)] \ . \quad (8)$$

Here ω is the laser angular frequency, c is the vacuum speed of light, and n is the index of refraction at the laser frequency. Note that we are using the Maker and Terhune[9] convention for the third-order nonlinear susceptibility. In this convention the effective nonlinear susceptibility is $3\chi_{1111}^{(3)\prime\prime}(-\omega; \omega, \omega, -\omega)$ because there are three distinct permutations of the positive and negative frequency arguments. This is the same convention that has recently been used by Levenson and Bloembergen[10] in their study of the resonant behavior of third-order nonlinear susceptibilities by three-wave mixing.

The results that we have heretofore discussed are for pure two-photon transitions. These theoretical results are appropriate for the interpretation of data for which the direct energy gap of the semiconductor is less than the combined energy of two photons. It is also possible to have TPA in an indirect gap semiconductor by the simultaneous emission or absorption of a phonon. Although we

report here TPA from GaP, an indirect gap material, we shall not attempt to present here the theory associated with this third-order process. For a discussion of the theoretical aspects of TPA from indirect gap materials the reader is referred to Refs. 11 and 12.

There are, however, several theoretical aspects of TPA from indirect gap materials that are noteworthy. Firstly, the TPA coefficient β is expected to be a strong function of the temperature because of the phonon participation in the TPA process. Secondly, for the laser intensities and frequency used in this experiment the TPA in indirect gap materials is less than that in direct gap materials.

Until now we have tacitly assumed that absorption by two-photon created excess carriers is negligible. This assumption is not always valid. Usually the dominant absorption by excess carriers comes from free holes; therefore, we can write by analogy with Eq. (3)

$$\frac{dI(\vec{r}, t)}{dz} = -\alpha I(\vec{r}, t) - \beta I^2(\vec{r}, t) - n(\vec{r}, t)\,\sigma_h I(\vec{r}, t) \quad , \qquad (9)$$

where $n(\vec{r}, t)$ is the number of two-photon excited free holes per unit volume, and σ_h is the free hole absorption cross section. The excess hole density $n(\vec{r}, t)$ is determined by the relation

$$\frac{\partial n(\vec{r}, t)}{\partial t} = D_h \nabla^2 n(\vec{r}, t) - \frac{n(\vec{r}, t)}{t_h} + \frac{\beta I^2(\vec{r}, t)}{2\hbar\omega} \quad , \qquad (10)$$

where D_h is the hole diffusion coefficient and t_h is the hole recombination lifetime. In general, one must solve the coupled Eqs. (9) and (10). For picosecond pulses both diffusion and recombination may be neglected; therefore, the hole density is expressed by the relation

$$n(\vec{r}, t) = \int_{-\infty}^{t} (\beta/2\hbar\omega)\, I^2(\vec{r}, t')\, dt' \quad . \qquad (11)$$

Note also that we can solve Eq. (9) for the picosecond laser pulse if we assume that all absorption mechanisms are small. In this case the perturbation solution for the irradiance is given by the expression

$$I(r, z, t) = (1 - R)\Big(I_0(r, 0, t) - \alpha z I_0(r, 0, t) - \beta z I_0^2(r, 0, t) \times (1 - R) - \frac{\sigma_h \beta z I_0(r, 0, t)(1 - R)^2}{2\hbar\omega} \times \int_{-\infty}^{t} I_0^2(r, 0, t')\, dt'\Big). \qquad (12)$$

We have assumed that the incident irradiance is $I_0(r, 0, t)$ and that the irradiated medium occupies the half-space $z \geq 0$.

Finally we note that for picosecond pulses the attenuation due to the excited hole absorption is comparable to the direct two-photon absorption if the irradiance is equal to a critical irradiance I_{cr} given by the expression

$$I_{cr} = 2\hbar\omega/\sigma_h \tau(1 - R) \quad ,$$

where τ is the $1/e$ pulse intensity half duration. The corresponding expression for pulses longer than the hole lifetime is given by a similar expression in which the pulse duration is replaced by the hole lifetime. We conclude, therefore, that in order to obtain pulse attenuation due to pure two-photon absorption one should use the shortest possible pulse duration.

III. EXPERIMENTAL APPARATUS AND TECHNIQUES

A. Laser system

A passively mode-locked YAlG: Nd (neodymium-doped yttrium aluminum garnet) laser system produced the picosecond pulses used in these experiments. A schematic diagram of the experimental apparatus is exhibited in Fig. 1. The laser oscillator is a xenon flashlamp pumped 6-mm-diameter by 7.62-cm-long YAlG: Nd rod in the Brewster-Brewster configuration. The oscillator is simultaneously Q-switched and mode-locked by a flowing saturable absorber (Kodak 9860) in contact with the high reflectivity mirror of the oscillator cavity. The output of the oscillator is restricted to the TEM_{00} mode by a 2 mm diameter aperture. The output of the oscillator consists of a train of picosecond pulses separated by approximately 8 nsec. From this train of pulses a single pulse is selected by a cylindrical-ring electrode potassium-dideuterium-phosphate Pockels cell. This Pockels cell is positioned between crossed Glan prisms, and is activated by a laser-triggered spark gap. The selected laser pulse is subsequently amplified by two YAlG: Nd laser amplifiers.

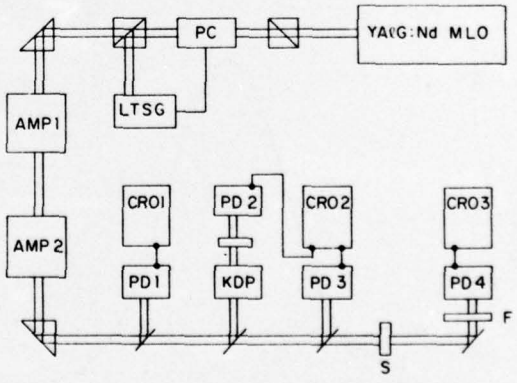

FIG. 1. Schematic diagram of the experimental apparatus. YAlG: Nd MLO, neodymium doped YAlG mode-locked laser; PC, Pockels cell; LTSG, laser triggered spark gap; AMP, neodymium doped YAlG laser amplifier; PD, photodiode; CRO, oscilloscope, F, filter; KDP, second-harmonic generation crystal; S, sample.

A high speed biplanar photodiode PD-1 (ITT F4000) is used in conjunction with CRO-1, a Tektronix 519 oscilloscope, to insure that only a single pulse is selected from the oscillator train of pulses. The calibrated photodiode PD-3 (S-1 response) measures the energy incident on the two-photon absorbing medium, and photodiode PD-4 (S-1 response) measures the energy transmission of this medium. A phase matched KDP (potassium dihydrogen phosphate) second-harmonic generation crystal and photodiode PD-2 (S-20 response) are used together with PD-3 to measure the individual pulse maximum irradiance. This technique is discussed below.

B. Pulse characteristics

For an accurate quantitative measurement of many nonlinear optical properties of materials it is necessary to know the spatial and the temporal form of the pulse incident on the material being studied. The spatial profile of the laser pulse at the site of the two-photon absorbing medium was determined by several independent techniques. In one experiment we employed transverse scans of a 50 μm diameter pinhole coupled to a photodiode. The results of one of these scans are shown in Fig. 2. In another experiment we directly monitored with an oscilloscope the output of a linear array of 256 silicon photodiodes that were irradiated by an attenuated laser pulse. The results of each of these experiments indicated that the spatial form of the incident irradiance was Gaussian, and that the $1/e$ intensity radius was 1.1 ± 0.1 mm.

In order to determine the temporal pulse width two techniques were utilized—a second-harmonic autocorrelation (SHAC) method and two-photon fluorescence (TPF) photography.[13] In the TPF technique the initial pulse is split into two pulses by a beamsplitter, and these pulses are redirected by mirrors to overlap within a two-photon absorbing material such as Rhodamine 6G. The dye fluorescence is photographed, and the pulse duration is determined by the spatial distribution of the exposure produced by the fluorescence track. In the second-harmonic autocorrelation method the pulse is split into two pulses by a Michelson interferometer. These two pulses are collinearly recombined after one pulse has been delayed by a variable amount. The recombined pulses are subsequently directed through a phase matched second-harmonic generation crystal. One plots the second-harmonic output as a function of the delay, and the result of such a plot is exhibited in Fig. 3. The curve is a four parameter least-squares fit to the function, $K_1 + K_2 \exp[-2(z - z_0/2)^2/c^2\tau^2]$. This curve gives a contrast ratio, $(K_1 + K_2)/K_1$, of 2.7 to 1. The results of both the TPF photography and the SHAC method give the average temporal duration full width at half maximum of 30 ± 6 psec, implying an average $1/e$ halfwidth $\langle\tau\rangle$ of 18 ± 3.6 psec.

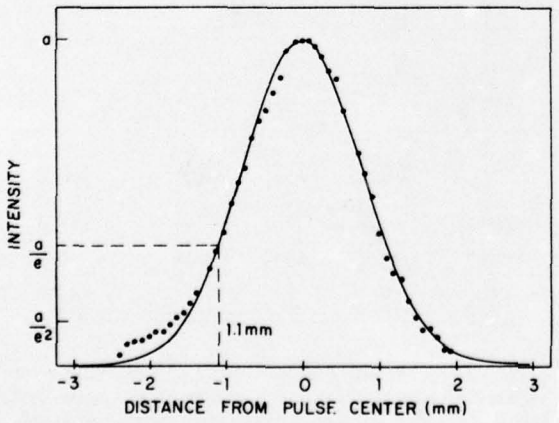

FIG. 2. Irradiance distribution at the sample. Solid line is a Gaussian fit to the data yielding a $1/e$ irradiance radius of 1.1 mm.

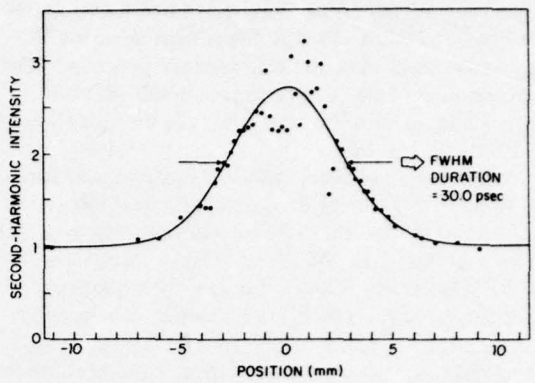

FIG. 3. Results of measurement of the average temporal duration of the laser pulse using a second-harmonic autocorrelation technique. Solid curve is a least-squares fit to the data yielding a FWHM duration of 30 psec and a contrast ratio of 2.7 to 1.

Although single-pulse TPF photographs are possible, the SHAC method is based on using many laser shots. We have found, however, that there are pulse-to-pulse fluctuations in the pulse duration.[14] A convenient way to measure the pulse duration, and thus the pulse irradiance for individual pulses, is to employ a nonlinear technique.[15] This method was first suggested by Glenn and Brienza[16] and involves measuring both the incident pulse energy $\mathcal{E}_f$ at the fundamental frequency and the total energy $\mathcal{E}_{sh}$ created at the second-harmonic frequency from a portion of the incident pulse. For small second-harmonic conversion efficiencies in the phase matched second-harmonic generation

crystal the relation $\mathcal{E}_t^2/\mathcal{E}_{sh}$ is proportional to the product of the incident pulse duration and the incident pulse area. If in an experiment a sufficiently large number of data points are taken so that the ratio $\mathcal{E}_t^2/\mathcal{E}_{sh}$ is meaningful, then this average value can be equated to the product of the known values of the average pulse duration and the average pulse area. Thus we can measure the individual pulse maximum irradiance on a shot-to-shot basis.

C. Procedure

The technique of obtaining the two-photon absorption coefficient β is to measure for each laser pulse the incident pulse energy, the transmitted pulse energy, and the pulse energy created at the second-harmonic frequency. The measurement of the pulse energy at the laser frequency in conjunction with the pulse energy at the second-harmonic frequency allows us to know the maximum pulse irradiance for each laser pulse as described in the previous section. The reciprocal of the energy transmission is then plotted versus the maximum incident irradiance. The incident irradiance was changed by either changing the gain of the amplifiers or by changing the position of the pulse selected from the oscillator train.

IV. EXPERIMENTAL RESULTS

In order to determine β, the two-photon absorption coefficient, we measured the energy transmission for different irradiances. The irradiance exiting a sample of thickness l for a spatially and temporally Gaussian laser pulse is given by the expression

$$I(r,l,t) = \frac{I_m e^{-(r/d)^2} e^{-(t/\tau)^2}(1-R)^2 e^{-\alpha l}}{1+\beta I_m(1-R)e^{-(r/d)^2}e^{-(t/\tau)^2}(1-e^{-\alpha l})/\alpha} \quad . \quad (13)$$

The energy transmission coefficient T is thus

$$T = \frac{\mathcal{E}^{\text{out}}}{\mathcal{E}^{\text{in}}} = \frac{2\pi \int_0^\infty r\,dr \int_{-\infty}^{\infty} I_m(r,l,t)\,dt}{I_m \pi d^2 \pi^{1/2}\tau}$$

$$= 2\frac{\alpha}{\beta}\frac{e^{-\alpha l}}{I_m \pi^{1/2}}\frac{1-R}{1-e^{-\alpha l}} \times \int_0^\infty \ln\left(1+\frac{\beta}{\alpha} I_m(1-R)(1-e^{-\alpha l})e^{-x^2}\right) dx \quad . \quad (14)$$

Expression (14) represents the basic equation used to derive β from the experimental measurement of T (or T^{-1}) vs I_m. Of course Eq. (14) is only appropriate when the absorption by two-photon excited free holes in negligible. The limitations thus required will be considered separately for each of the materials studied.

The TPA coefficient β was measured for three samples of single-crystal n-type GaAs with the laser electric field along the [001] direction of this zinc-blende material. In all experiments unless otherwise indicated the samples were irradiated at normal incidence along the [110] direction. Sample 1 was Te doped with a carrier concentration of 2×10^{18} cm^{-3}; the thickness was 0.09 cm. The experimental results indicate that $\beta = 0.030 \pm 0.005$ cm/MW with a one-photon absorption coefficient $\alpha = 8.0$ cm^{-1}. Samples 2 and 3 were both cut from the same boule and both had a carrier concentration of 5×10^{16} cm^{-3}. Sample 2 had a length of 0.22 cm, and β was measured to be 0.030 ± 0.005 cm/MW with $\alpha = 0.7$ cm^{-1}. The results for this sample are plotted in Fig. 4. From this figure we note that for incident irradiances above 300 MW/cm^2 there is a small but significant departure of the experimental data points from the theoretical curve. Similar effects were observed in other samples. This departure can be attributed to the free hole absorption, and thus there is an enhanced attenuation of the pulse at high intensities. Another possible explanation is beam distortion due to the real part of the third-order nonlinear susceptibility. This will be considered in Sec. V.

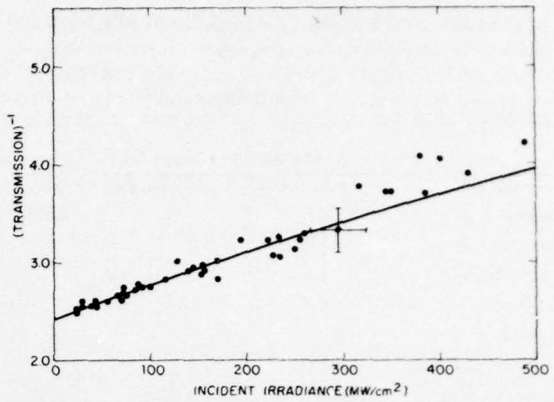

FIG. 4. Plot of reciprocal energy transmission coefficient vs maximum incident irradiance for GaAs. Sample thickness is 0.22 cm, and the laser electric field was polarized along the [001] direction. Theoretical curve is given by Eq. (14) with $\alpha = 0.7$ cm^{-1} and $\beta = 0.03$ cm/MW.

Sample 3 had a length of 1.29 cm; the one-photon absorption coefficient was the same as Sample 2, but the TPA coefficient was found to be 0.023 ± 0.005 cm/MW. The reason that the measured value of β is smaller for the longer sample probably results from the reflection at the exit surface. The reflected wave suffers a π phase change that enhances the total irradiance at and near the exit surface. Since the model that we are using doesn't include the effects of multiple reflections, we can expect the effective TPA coefficients to be slightly smaller for longer crystals.[17]

TABLE I. Various experimental values of the two-photon absorption coefficient β, the linear absorption coefficient α, and the optical electric field direction in GaAs at 1.06 μm and at room temperature.

	β (cm/MW)	α (cm^{-1})	Electric field
Present work	0.023–0.030	0.7–8.0	[001]
Bepko[a]	0.085	...	[001]
Lee and Fan[b]	0.23–0.36	4.0	...
Kleinman *et al.*[c]	0.019–0.045	0.05–4.0	...
Jayaraman and Lee[d]	5.6	3–4	...
Oksman *et al.*[e]	0.2	...	...
Ralston and Chang[f]	0.02	...	...
Arsen'ev *et al.*[g]	0.8	4.0	...
Basov *et al.*[h]	5.0	...	...

[a]Reference 18.
[b]Reference 20.
[c]Reference 21.
[d]Reference 22.
[e]Reference 23.
[f]Reference 24.
[g]Reference 25.
[h]Reference 26.

Finally we observed a small anisotropy of the TPA coefficient in Sample 3. For the laser field along the [110] direction we find that β is approximately 20% larger than when the laser field is along the [001] direction. A similar anisotropy was recently observed in Ref. 18.

A single crystal of high-resistivity ($\rho > 10^8$ Ω cm) n-type CdTe was examined for TPA. The crystal was 0.49 cm in length and was irradiated along the [110] direction with the electric field polarized along the [001] axis. The best fit to the experimental data gives $\alpha = 0.45$ cm^{-1} and $\beta = 0.025 \pm 0.005$ cm/MW.

A sample of 0.10-cm-thick p-type ZnTe was irradiated along the [110] direction with the laser electric field along the [001] direction. The best fit to the data gives $\alpha = 8$ cm^{-1} and $\beta = 0.008 \pm 0.004$ cm/MW.

In addition to the zinc-blende crystals described above we have also measured the TPA properties of CdSe, a wurtzite structure. The sample was 0.385 cm thick, and the incident laser irradiance was directed along the c axis of this hexagonal crystal. The data indicate that $\alpha = 0.2$ cm^{-1} and $\beta = 0.030 \pm 0.005$ cm/MW.

Of the materials considered in this experiment GaP is unique for two reasons. Firstly, at the laser energy of 1.165 eV per photon, GaP does not exhibit a direct-gap two-photon absorption. Instead the transition needs a phonon to participate in the absorption process. Secondly, the only crystal that we had available to us had an orientation such that the laser electric field could not be polarized along the [001] direction. We found that the two-photon absorption coefficient is much smaller in this material than in any of the other materials that we studied. The sample that we used was 4 mm thick with the [111] direction normal to the optically polished surfaces. For our experiment data were taken with the laser electric field along the [110] direction.

In order to measure any change in the transmission coefficient it was necessary to use incident irradiances in excess of 1 GW/cm^2. Since this irradiance is comparable to the critical irradiance I_{cr} for GaP then the effect of free hole absorption must be considered. This was considered in our interpretation of the data, and the TPA coefficient β was determined by comparing the experimental energy transmission coefficient to the theoretical coefficient obtained by integrating Eq. (12) over the spatial and temporal profile of the laser pulse. The free hole absorption cross section was assumed to be 2×10^{-17} cm^2.[19] From our data we find that $\alpha = 0.5$ cm^{-1} and $\beta = 0.0002 \pm 0.0001$ cm/MW.

V. DISCUSSION AND SUMMARY

There are very large discrepancies among the various measurements of the two-photon absorption coefficient β in GaAs as can be seen from Table I.[18,20–26] Our measurements seem to be in closest agreement with those of Ref. 21. It is noteworthy that any spatial or temporal fluctuations in the laser pulses used for the TPA measurements can lead to larger TPA. Thus if the lasers used in some of these other experiments did not produce smooth reproducible pulses, the inferred value of the two-photon absorption coefficient would be larger than the true value.

In Sec. II we discussed the importance of free hole absorption and noted that picosecond pulses are favored over nanosecond pulses for an accurate measurement of the TPA coefficient. The cross sections for free hole absorption were estimated from the one-photon absorption measurements in p-type materials. The results are as follows: 1×10^{-17} cm^2 (GaAs),[27] 4×10^{-17} cm^2 (CdTe),[28] 3×10^{-17} cm^2 (ZnTe),[29] and 2×10^{-17} cm^2 (GaP).[19] There is no known measurement for CdSe. From these values the critical irradiance, I_{cr}, was calculated and except for GaP, as noted above, only data points less than I_{cr} were used to infer the TPA coefficient. If we compare our experiments with others as in Tables I and II we find that our experimental results for the TPA coefficients are among the smallest reported values. Our results for the direct-gap semiconductors are typically within a factor of 2 of the theoretical results obtained using the Keldysh model to calculate the TPA coefficient.

Our experimental results as well as the results based on several theoretical calculations are presented in Table III. For the direct-gap semiconductors the TPA coefficient was measured with the laser electric field polarized along the [001] direction; thus, second-harmonic generation was pro-

TABLE II. Experimental values of the two-photon absorption coefficient β in CdTe, CdSe, ZnTe, and GaP at room temperature. The units are cm/MW.

	CdTe	CdSe	ZnTe	GaP
Present work	0.025	0.03	0.008	2×10^{-4}
Bepko[a]	0.17			
Ralston and Chang[b]	0.2	0.2		
Basov *et al.*[c]		0.95		
Lee and Fan[d]			0.04	
Yee and Chau[e]				1.7×10^{-3}
Bryukner *et al*[f]		0.14		

[a]Reference 18.
[b]Reference 24.
[c]Reference 26.
[d]Reference 20.
[e]Reference 30.
[f]F. Bryukner, V. S. Dneprovskii, and V. U. Khattatov, Kvant. Electron. 1, 1360 (1974); [Sov. J. Quantum Electron. 4, 749 (1974)].

hibited for these materials, and the imaginary part of the third-order optical nonlinear susceptibility $\chi^{(3)}_{1111}(-\omega, \omega, \omega, -\omega)$ at the laser frequency may be inferred from the TPA coefficient.

In GaP several different attenuation mechanisms are possible. In addition to indirect TPA and free hole absorption it is also possible to have second-harmonic generation followed by one-photon absorption for the laser electric field polarized along the [110] direction. Finally since the observed attenuation was very small three-photon absorption was also considered. To predict the amount of three-photon absorption a simple calculation using the Keldysh model shows that three-photon absorption is negligible compared to the other attenuation mechanisms at the irradiances used in this experiment. Moreover, we can calculate the effective TPA coefficient due entirely to second harmonic generation followed by one-photon absorption. We find for GaP at 1.064 μm that $\beta_{SHG}\approx10^{-6}$ cm/MW. This is approximately two orders of magnitude less than the experimental value that we obtain. We conclude, therefore, that the attenuation mechanism is a combination of two-photon absorption across the indirect gap plus linear absorption by the resulting free holes. If the value of the free hole absorption cross section is known, then we may infer the TPA coefficient β from the measured transmission change. This value is reported also in Table III. Our experimental value compares very favorably with the theoretical value given in Ref. 30, but is approximately an order of magnitude less than the experimental value reported in this same reference.

In Sec. IV we noted that at high irradiances there is a departure of the experimental data from the theoretical curve obtained from the lower irradiance data. We noted that one possible explanation for this departure would be beam deformation due to the self-focusing aspect of the real part of the third-order nonlinear susceptibility. In order to estimate this effect we have calculated the beam intensity radius $a(l)$ at the exit surface of the crystal for an input radius a_0. The relation between these radii is given by the following approximation[31]

$$\frac{a(l)^2}{a_0^2}\approx\left[1+\left(1-\frac{P}{P_{cr}}\right)\frac{l^2}{k_0^2a_0^4}\right]. \tag{15}$$

The length of the crystal is l, P is the maximum laser power, and k_0 is the laser wave vector in vacuum. The parameter P_{cr} is the critical power for self-focusing and is given by

$$P_{cr}=c^3/8\omega^2n_2\ . \tag{16}$$

Here c is the vacuum speed of light, ω is the laser

TABLE III. Summary of the experimental results obtained in this work, and the results of several theoretical models.

Material	Index of refraction	β (cm/MW)[a]	$\chi^{(3)}_{1111}(-\omega\,\omega, \omega, -\omega)$ (cm^3/erg)	β (cm/MW), Theory 1[b]	2[c]	3[d]	4[e]
GaAs	3.475	$(2.8\pm0.5)\times10^{-2}$	1.8×10^{-11}	1.7×10^{-2}	3.1×10^{-2}	6.2×10^{-2}	
CdTe	2.818	$(2.5\pm0.5)\times10^{-2}$	1.1×10^{-11}	2.1×10^{-2}			
CdSe	2.539	$(3.0\pm0.5)\times10^{-2}$	1.0×10^{-11}	1.9×10^{-2}			
ZnTe	2.777	$(8.0\pm4.0)\times10^{-3}$	3.3×10^{-12}	3.8×10^{-3}	2.5×10^{-3}	3.2×10^{-2}	
GaP	3.106	$(2\pm1)\times10^{-4}$					1.9×10^{-4}

[a]If more than one sample was measured, the average value is given.
[b]Calculated from Eq. (41) of Ref. 7.
[c]Reference 20, degenerate valance band, no exciton.
[d]Reference 20, degenerate valance band, with exciton.
[e]Reference 30.

angular frequency, and n_2 is the intensity dependent nonlinear index of refraction. For self-focusing produced by an electronic nonlinearity, the intensity-dependent nonlinear index of refraction may be estimated by Wang's rule.[32] This is the contribution due to the bound electrons, and as an example, for GaAs we estimate that $n_2 \approx 1.6 \times 10^{-10}$ esu and $P_{cr} \approx 670$ W. Additional contributions to n_2 may come from the nonparabolicity of the conduction band and the number of conduction-band electrons.[33,34] However, for the intensities at which these effects become important, there is a decrease in the *linear* index of refraction that is linear in the number of excited free electrons. The net result would be a defocusing of the beam. Using the maximum possible values of the effective n_2 and Eqs. (15) and (16) we find that the area of the laser pulse at the exit surface is less than 10% smaller than at the incident surface. This is true even for the longest sample at the highest power. Moreover, we have estimated the effects of thermal self-focusing due to the temperature dependence of the linear index of refraction. We find that these effects are also small. Finally, the beam size was observed using an infrared-absorbing-visible-emitting phosphor. At no time was there a discernible change in the beam size at either high or low powers. We conclude, therefore, that pulse deformation due to self-focusing effects was not a serious problem in the interpretation of any of the experiments reported here.

In conclusion, we have measured the TPA coefficient for four direct gap and one indirect gap semiconductors. Our experimentally measured values of the TPA coefficient are significantly less than most previous measurements, but in reasonable agreement with several theoretical models. For the direct gap semiconductors we have related our measurement of the TPA coefficient to the imaginary part of the third-order nonlinear susceptibility of the material.

ACKNOWLEDGMENTS

We would like to thank S. Maurici for his preparation of many of the materials used in this investigation. One of us (J.H.B.) would like to thank Dr. G. A.N. Connell, Dr. T. D. Moustakas, Dr. H. Lotem, and Dr. E. Yablonovitch for several useful discussions. Finally, we would like to thank Professor N. Bloembergen for his support and comments on the manuscript.

---

*Supported by the Joint Services Electronic Program and the NASA.

[1]M. Goppert-Mayer, Ann. Phys. (Leipz.) 9, 273 (1931).
[2]W. Kaiser and C. G. B. Garrett, Phys. Rev. Lett. 7, 229 (1961).
[3]N. G. Basov, A. Z. Grasyuk, I. G. Zubarev, V. A. Katulin, and O. N. Krokhin, Zh. Eksp. Teor. Fiz. 50, 551 (1966) [Sov. Phys.-JETP 23, 366 (1966)].
[4]D. J. Bradley and G. H. C. New, Proc. IEEE 62, 313 (1974).
[5]J. M. Worlock, in *Laser Handbook*, edited by T. Arecchi and F. Schulz-Dubois (North-Holland, Amsterdam, 1972), p. 1323.
[6]V. I. Bredikhin, M. D. Galanin, and V. N. Genkin, Ups. Fiz. Nauk 110, 3 (1973) [Sov. Phys. -Usp. 16. 299 (1973)].
[7]L. V. Keldysh, Zh. Eksp. Teor. Fiz. 47, 1945 (1964) [Sov. Phys.-JETP 20, 1307 (1965)].
[8]D. Bedeaux and N. Bloembergen, Physica (Utr.) 69, 57 (1973).
[9]P. D. Maker and R. W. Terhune, Phys. Rev. 137, A801 (1965).
[10]M. D. Levenson and N. Bloembergen, Phys. Rev. B 10, 4447 (1974).
[11]J. H. Yee, J. Phys. Chem. Solids 33, 643 (1972).
[12]F. Bassani and A. R. Hassan Nuovo Cimento B 7, 313 (1972).
[13]P. W. Smith, M. A. Duguay, and E. P. Ippen, in *Progress in Quantum Electronics*, edited by J. H. Sanders and S. Stenholm (Pergamon, Oxford, 1974), Vol. 3, Part 2, Chap. 4.
[14]J. H. Bechtel and W. L. Smith (unpublished).
[15]W. L. Smith and J. H. Bechtel (unpublished).
[16]W. H. Glenn and M. J. Brienza, Appl. Phys. Lett. 10, 221 (1967).
[17]R. A. Baltrameyunas, Yu. Yu. Vaitkus, Yu. K. Vishchaskas, and V. I. Gavryushin, Opt. Spektrosk. 36, 1225 (1974) [Opt. Spectrosc. 36, 714 (1974)].
[18]S. J. Bepko, Phys. Rev. B 12, 669 (1975).
[19]J. D. Wiley and M. DiDomenico, Jr., Phys. Rev. B 3, 375 (1975).
[20]C. C. Lee and H. Y. Fan, Phys. Rev. B 9, 3502 (1974).
[21]D. A. Kleinman, R. C. Miller, and W. A. Nordland, Appl. Phys. Lett. 23, 243 (1973).
[22]S. Jayaraman and C. H. Lee, Appl. Phys. Lett. 20, 392 (1972).
[23]Ya. A. Oksman, A. A. Semenov, V. N. Smirnov, and O. M. Smirnov. Fiz. Tekh. Poluprovodn. 6, 731 (1972) [Sov. Phys. -Semicond. 6, 629 (1972)].
[24]J. M. Ralston and R. K. Chang, Appl. Phys. Lett 15, 164 (1969).
[25]V. V. Arsen'ev, V. S. Dneprovskii, D. N. Klyshko, A. N. Penin, Zh. Eksp. Teor. Fiz. 56, 760 (1969) [Sov. Phys. -JETP 29, 413 (1966)].
[26]N. G. Basov, A. Z. Grasyuk, V. F. Efimkov, I. G. Zubarev, V. A. Katulin, and Ju. M. Popov, J. Phys. Soc. Jpn. Suppl. 21, 277 (1966).
[27]I. Kudman and T. Seidel, J. Appl. Phys. 33, 771 (1962).
[28]V. Capek, K. Zimmerman, C. Konak, M. Popova, and P. Polivka, Phys. Status Solidi B 56, 739 (1973).
[29]N. Watanabe, J. Phys. Soc. Jpn. 21, 713 (1966).
[30]J. H. Yee and H. H. M. Chau, Opt. Commun. 10, 56 (1974).
[31]W. G. Wagner, H. A. Haus, and J. H. Marburger, Phys. Rev. 175, 256 (1968).
[32]C. C. Wang, Phys. Rev. B 2, 2045 (1970).
[33]P. K. Dubey and V. V. Paranjape, Phys. Rev. 8, 1514 (1973).
[34]J. J. Wynne, Phys. Rev. 178, 1295 (1969).

JSEP REPORTS DISTRIBUTION LIST

N00014-75-C-0648

Defense ... ...ation Center
Attn: DDC-TCA (Mrs. V. Caponio)
Cameron Station
Alexandria, Virginia 22314

Asst. Director
Electronics and Computer Sciences
Office of Director of Defense Research and Engineering
The Pentagon
Washington, DC 20315

Office of the Director of Defense Research and Engineering
Information Office Library Branch
The Pentagon
Washington, DC 20301

ODDR and E Advisory Group on Electron Devices
201 Varick Street
New York, New York 10014

Chief, R and D Division (340)
Defense Communications Agency
Washington, DC 20301

Director, National Security Agency
Fort George G. Meade, Maryland 20755
Attn: Dr. T. J. Beahn

Institute for Defense Analysis
Science and Technology Division
400 Army-Navy Drive
Arlington, Virginia 22202

Dr. Stickley
Defense Advanced Research Projects Agency
Attn: Technical Library
1400 Wilson Boulevard
Arlington, Virginia 22209

Dr. R. Reynolds
Defense Advanced Research Projects Agency
Attn: Technical Library
1400 Wilson Boulevard
Arlington, Virginia 22209

AF/RDPS
The Pentagon
Washington, DC 20330

AFSC (LJ/Mr. Irving R. Mirman)
Andrews AFB
Washington, DC 20334

Directorate of Electronics and Weapons
HQ AFSC/DLC
Andrews AFB, Maryland 20334

Directorate of Science
HQ AFSC/DLS
Andrews AFB
Washington, DC 20334

LTC J. W. Gregory
AF Member, TAC
Air Force Office of Scientific Research
Bolling AFB
Washington, DC 20332

Mr. Carl Sletten
AFCRL/LZ
Hanscom AFB, MA 01731

Dr. Richard Picard
AFCRL/OPL
Hanscom AFB, MA 01731

Mr. Robert Barrett
AFCRL/LQ
Hanscom AFB, MA 01731

Dr. John N. Howard
AFCRL (CA)
Hanscom AFB, MA 01731

Dr. Richard B. Mack
AFCRL/LZR
Hanscom AFB, MA 01731

Documents Library (TILD)
Rome Air Development Center
Griffiss AFB, New York 13441

Mr. H. E. Webb, Jr. (ESCP)
Rome Air Development Center
Griffiss AFB, New York 13441

Mr. Murray Kesselman (ESCA)
Rome Air Development Center
Griffiss AFB, New York 13441

Mr. W. Edwards
AFAL/TE
Wright-Patterson AFB, Ohio 45433

Mr. R. D. Larson
AFAL/DHR
Wright-Patterson AFB, Ohio 45433

Chief Scientist
AFAL/CA
Wright-Patterson AFB, Ohio 45433

HQ ESD (DRI/Stop 22)
Hanscom AFB, MA 01731

Professor R. E. Fontana
Head Dept. of Electrical Eng.
AFIT/ENE
Wright-Patterson AFB, Ohio 45433

Mr. John Mottemith (MCIT)
HQ ESD (AFSC)
Hanscom AFB, MA 01731

LTC Richard J. Gowen
Professor
Dept. of Electrical Engineering
USAF Academy, Colorado 80840

AUL/LSE-9663
Maxwell AFB, Alabama 36112

AFETR Technical Library
P.O. Box 4608, MU 5650
Patrick AFB, Florida 32542

ADTC (DLOSL)
Eglin AFB, Florida 32542

HQ AMD (RDR/COL Godden)
Brooks AFB, Texas 78235

USAF European Office of Aerospace Research
Technical Information Office
Box 14, FPO, New York 09510

Dr. Carl E. Baum
AFWL (ES)
Kirtland AFB, New Mexico 87117

ASAFSAM/FAL
Brooks AFB, Texas

HQDA (DAMA-ARZ-A)
Washington, DC 20310

Commander
US Army Security Agency
Attn: IARD-T
Arlington Hall Station
Arlington, VA 22212

Commander
US Army Materiel Development and Readiness Command
Attn: Technical Library, Rm 7S 35
5001 Eisenhower Avenue
Alexandria, VA 22333

Commander
US Army Ballistics Research Laboratory
Attn: DRXRD-BAD
Aberdeen Proving Ground
Aberdeen, MD 21005

Commander
Picatinny Arsenal
Attn: SMUPA-TS-T-S
Dover, NJ 07801

US Army Research Office
Attn: Dr. Hermann Robl
P.O. Box 12211
Research Triangle Park, NC 27709

US Army Research Office
Attn: Mr. Richard O. Ulsh
P.O. Box 12211
Research Triangle Park, NC 27709

US Army Research Office
Attn: Dr. Jimmie R. Suttle
P.O. Box 12211
Research Triangle Park, NC 27709

US Army Research Office
Attn: Dr. Horst Wittmann
P.O. Box 12211
Research Triangle Park, NC 27709

Commander
Frankford Arsenal
Attn: Mr. George, C. White, Jr.
Deputy Director, Pitman-Dunn Lab.
Philadelphia, PA 19137

Commander
US Army Missile Command
Attn: Chief, Document Section
Redstone Arsenal, AL 35809

Commander
US Army Missile Command
Attn: DRSMI-RR
Redstone Arsenal, AL 35809

Commander
US Army Materials and Mechanics Research Center
Attn: Chief, Materials Sciences Division
Watertown, MA 02172

Commander
Harry Diamond Laboratories
Attn: Mr. John E. Rosenberg
2800 Powder Mill Road
Adelphi, MD 20783

Commandant
US Army Air Defense School
Attn: ATSAD-T-CEM
Fort Bliss, TX 79916

Commandant
US Army Command and General Staff College
Attn: Acquisitions, Lib. Div.
Fort Leavenworth, Kansas 66027

Dr. Hans K. Ziegler
Army Member, TAC/JSEP
US Army Electronics Command
(DRSEL-TL-D)
Fort Monmouth, NJ 07703

Mr. J. E. Teti
Executive Secretary, TAC/JSEP
US Army Electronics Command
(DRSEL-TL-DT)
Fort Monmouth, NJ 07703

Director
Night Vision Laboratory, ECOM
Attn: DRSEL-NV-D
Fort Belvoir, VA 22060

Commander/Director
Atmospheric Sciences Laboratory (ECOM)
Attn: DRSEL-BL-DD
White Sands Missile Range, NM 88002

Director
Electronic Warfare Laboratory (ECOM)
Attn: DRSEL-WL-MY
White Sands Missile Range, NM 88002

Commander
US Army Armament Command
Attn: DRSAR-RD
Rock Island, IL 61201

Director, Div. of Neuropsychiatry
Walter Reed Army Institute of Research
Washington, DC 20012

Commander
USASATCOM
Fort Monmouth, NJ 07703

Commander
US Army R and D Group (Far East)
APO San Francisco, CA 96343

Commander
US Army Communications Command
Attn: Director, Advanced Concepts Office
Fort Huachuca, AZ 85613

Project Manager
ARTADS
EAI Building
West Long Branch, NJ 07764

Commander
US Army White Sands Missile Range
Attn: STEWS-ID-R
White Sands Missile Range, NM 88002

Director, TRI-TAC
Attn: TT-AD (Mrs. Briller)
Fort Monmouth, NJ 07703

Commander
US Army Communication Command
Attn: CC-OPS-PD
Fort Huachuca, AZ 85613

COL Robert Noce
Senior Standardization Representative
US Army Standardization Group, Canada
Canadian Force Headquarters
Ottawa, Ontario, Canada K1A 0K2

Commander
US Army Electronics Command
Attn: DRSEL-RD-O (Dr. W. S. McAfee)
CT-L (Dr. R. Buser)
NL-O (Dr. H. S. Bennett)
NL-T (Mr. R. Kulinyi)
TL-B
VL-D
WL-D
TL-MM (Mr. N. Lipetz)
NL-H (Dr. F. Schwering)
TL-E (Dr. S. Kronenberg)
TL-K (Dr. J. Kohn)
TL-I (Dr. C. Thornton)
NL-B (Dr. S. Amoroso)
Fort Monmouth, NJ 07703

Project Manager
Ballistic Missile Defense Program Office
Attn: DACS-BMP (Mr. A. Gold)
1300 Wilson Blvd.
Washington, DC 22209

Dr. Sidney Ross
Technical Director
SARFA-TD
Frankford Arsenal
Philadelphia, PA 19137

Department of Naval Research
Electronic and Solid State Sciences Program (Code 427)
800 N. Quincy
Arlington, Virginia 22217

Office of Naval Research
Code 200
Assistant Chief for Technology
800 N. Quincy
Arlington, Virginia 22217

Office of Naval Research
Information Sciences Program (Code 437)
800 N. Quincy
Arlington, Virginia 22217

Naval Research Laboratory
4555 Overlook Avenue, S.W.
Washington, DC 20375
Attn: Codes 2627
4000
4105
5300
5200
5203
5210
5270
5300
5400
5460
5404
5500
5510
6400

Director
Office of Naval Research Branch Office
536 South Clark Street
Chicago, Illinois 60605

San Francisco Area Office
Office of Naval Research
760 Market Street, Room 447
San Francisco, CA 94102

Dr. A. Laufer
Chief Scientist
Office of Naval Research Branch Office
1030 East Green Street
Pasadena, CA 91101

Director
Office of Naval Research Branch Office
715 Broadway, 5th Floor
New York, New York 10003

Mr. L. W. Sumney
Naval Electronics Systems Command
NC No. 1
2511 Jefferson Davis Highway
Arlington, VA 20360

Mr. R. Fratila
Naval Electronics Systems Command
NC No. 1
2511 Jefferson Davis Highway
Arlington, VA 20360

Mr. N. Butler
Naval Electronics Systems Command
NC No. 1
2511 Jefferson Davis Highway
Arlington, VA 20360

Dr. H. J. Mesller
Naval Air Systems Command
JP No. 1
1411 Jefferson Davis Highway
Arlington, VA 20360

Capt. R. B. Meeks
Naval Sea Systems Command
NC No. 3
2531 Jefferson Davis Highway
Arlington, VA 20362

Commander
Naval Surface Weapons Center
Attn: Technical Library
Silver Spring, Maryland 29010

Officer-in-Charge
Naval Surface Weapons Center
Dahlgren Laboratory
Dahlgren, Virginia 22448

Naval Air Development Center
Attn: Technical Library
Johnsville
Warminster, Penn. 18974

Commander
Naval Avionics Facility
Indianapolis, Indiana 46241
Attn: D/035 Technical Library

Naval Missile Center
Technical Library
Code 5632.2
Point Mugu, CA 93042

Naval Weapons Center
Attn: Technical Library
Code 533
China Lake, CA 93555

Naval Weapons Center
Attn: Code 6010
China Lake, CA 93555

Naval Weapons Center
Mathematics Division
China Lake, CA 93555

Naval Training Equipment Center
Technical Library
Orlando, Florida 32813

Naval Research Laboratory
Underwater Sound Reference Div.
Technical Library
P.O. Box 8337
Orlando, Florida 32806

Naval Underwater Sound Center
Technical Library
New London, Conn. 06320

U.S. Naval Oceanographic Office
Library - Code 1600
Washington, DC 20373

Commandant, Marine Corps
Scientific Advisor (Code AX)
Washington, DC 20380

Dr. Gernot M. R. Winkler
Director, Time Service
US Naval Observatory
Mass. Ave. at 34th St. N.W.
Washington, DC 20390

Naval Postgraduate School
Technical Library
Monterey, California 93940

Naval Electronics Laboratory Center
Technical Library
San Diego, California 92152

Naval Electronics Laboratory Center
Attn: Code 2600
San Diego, CA 92152

Naval Electronics Laboratory Center
San Diego, California 92152
Attn: Codes 2000
2200
2300
3000
3200
3300
4800
5000
5200
5300

Naval Undersea Center
Technical Library
San Diego, California 92152

Naval Ship Research and Development Center
David W. Taylor
Code 522.1
Bethesda, Maryland 20084

Office of Chief of Naval Operations
NAICOM/MIS Planning Branch
NOP-916D, Pentagon
Washington, DC 20350

Mr. F. C. Schwenk, RD-T
National Aeronautics and Space Administration
Washington, DC 20546

Los Alamos Scientific Laboratory
Attn: Reports Library
P.O. Box 1663
Los Alamos, New Mexico 87544

M. Zane Thornton
Deputy Director Institute for Computer Sciences and Technology
National Bureau of Standards
Washington, DC 20234

Director, Office of Postal Technology (R and D)
US Postal Service
11711 Parklawn Drive
Rockville, Maryland 20852

NASA Lewis Research Center
Attn: Library
21000 Brookpark Road
Cleveland, Ohio 44135

Library - R51
Bureau of Standards
Acquisition
Boulder, Colorado 80302

MIT Lincoln Laboratory
Attn: Library A-082
P.O. Box 73
Lexington, Mass. 02173

Dr. Jay Harris
Program Director
Devices and Waves Program NSF
1800 G Street
Washington, DC 20550

Dr. Howard W. Etzel
Deputy Director
Div. of Materials Research NSF
1800 G Street
Washington, DC 20550

Dr. Dean Mitchell
Program Director
Solid-State Physics
Div. of Materials Research
National Science Foundation
1800 G Street
Washington, DC 20550

Director
Research Laboratory of Electronics
Massachusetts Institute of Technology
Cambridge, Massachusetts 02139

Director
Microwave Research Institute
Polytechnic Institute of New York
Long Island Graduate Center, Route 110
Farmingdale, New York 11735

Asst. Director
Microwave Research Institute
Polytechnic Institute of New York
333 Jay Street
Brooklyn, New York 11201

Director
Columbia Radiation Laboratory
Dept. of Physics
Columbia University
538 West 120th Street
New York, New York 10027

Director
Coordinated Science Laboratory
University of Illinois
Urbana, Illinois 61801

Director
Stanford Electronics Laboratory
Stanford University
Stanford, California 94305

Director
Microwave Laboratory
Stanford University
Stanford, California 94305

Director
Electronics Research Laboratory
University of California
Berkeley, California 94720

Director
Electronics Sciences Laboratory
University of Southern California
Los Angeles, California 90007

Director
Electronics Research Center
The University of Texas at Austin
Engineering-Sciences Bldg. 112
Austin, Texas 87812

Director of Laboratories
Div. of Engineering and Appl. Physics
Harvard University
Pierce Hall
Cambridge, Mass. 02138